NON-CONTACT NDT OF CONCRETE STRUCTURES USING AIR-COUPLED SENSORS

BY

JINYING ZHU

B.E., Zhejiang University , 1992
D. Eng., Zhejiang University, 1997

DISSERTATION

Submitted in partial fulfillment of the requirements
for the degree of Doctor of Philosophy in Civil and Environmental Engineering
in the Graduate College of the
University of Illinois at Urbana-Champaign, 2005

Urbana, Illinois

Abstract

Elastic wave-based non-destructive test (NDT) methods are effective for detecting flaws in concrete structures. With the recent developments in computing hardware and software, imaging techniques have become very popular in NDT applications. However the application of elastic wave-based imaging methods for concrete structures is severely limited by the physical coupling between sensors and concrete surface, which reduces testing efficiency. In this thesis, the air-coupled sensing technique is proposed as a solution to improve the efficiency of elastic wave-based test methods for concrete structures.

Theoretical analyses are first conducted to study the propagation of leaky Rayleigh waves in fluid-solid half spaces. Closed-form solutions of the Green's function are derived for pressure and displacement in both the fluid and solid. This analysis provides theoretical background necessary for practical air-coupled sensing of leaky Rayleigh waves in concrete. The theory is also extended to underwater NDT applications.

Two applications of air-coupled sensing are considered. One is air-coupled leaky surface wave sensing in concrete. A laboratory study and field tests demonstrate that air-coupled sensors are very effective for sensing leaky surface waves in concrete. The sensitivity and accuracy of air-coupled sensors are comparable to contact sensors. Air-coupled sensors are suitable replacement for contact sensors in SASW and MASW tests and moreover help improve test efficiency. In addition, the contact-less nature of air-coupled sensing enables the study of the effect of defects on wave attenuation. The experimental results show leaky Rayleigh waves are sensitive to the existence of cracks in concrete when waves propagate across cracks; the crack positions are clearly located in a 2-D scanning test image.

The second application is air-coupled impact-echo. Two reinforced concrete slabs containing different types of defects were inspected using an air-coupled impact test testing scheme. 2-D scanning impact-echo tests were conducted over the slab containing voids and delaminations. The 2-D scanning image clearly shows the location of embedded defects, and their depths are also determined. Air-coupled impact-echo is also applied to examine the grouting condition of embedded ducts. The poorly-grouted and ungrouted sections are identified within the metal duct.

To Daqing, my husband, for his enormous patience, and love during this phase of our lives.
To my parents, sister and brother, for their continuous support and encouragement.

Acknowledgments

The author gratefully acknowledges the advice, support, and guidance of Dr. John Popovics during the course of this research. His assistance and trustfulness were fundamental to the achievement of the project. His understanding attitude, encouragement, and the time spent in amiable conversations made this five years very enjoyable. He is an excellent teacher and mentor, also a good friend.

Special thanks are given to Gonzalo Cetrangolo for his assistance in the experimental phase. The author would also thank Gonzalo Gallo, Anja Glusic for their help in experiments, and Cristian Gaedicke for assistance in access to the ATREL facilities.

Sincere appreciation goes to Dr. Frank Schubert of Fraunhofer Institute, Germany, for a fruitful collaboration and as a co-author.

Dr. Nils Ryden of Lund University provided valuable assistance on the MASW analysis. The author is also grateful to Dr. Richard Weaver and Dr. Nelson Hsu for their valuable suggestions on the theoretical analysis of leaky Rayleigh waves.

This work was carried out in the course of research sponsored by the National Science Foundation under grant number 0223819.

Finally I wish to thank my husband, Daqing, for his love and extraordinary effort during our four years at the U. of Illinois. Last, but not least,I would like to thank my parents for their continuous support and encouragement through my life, and for taking care of our son Richard, during the final phase of this thesis.

Table of Contents

List of Tables

List of Figures

1 Introduction

1.1 Significance of Developing Rapid NDT Imaging Techniques

The concrete infrastructure is comprised of a wide range of structure types, including bridge decks, beams, columns, pavements, piers and pipes. Each of these structures may contain damage or embedded flaws. In fact, there is growing concern about the deterioration of America's concrete infrastructure. Much of the infrastructure is approaching or has passed its original design life. The American Society of Civil Engineers (ASCE) finds the existing infrastructure in America is in critically poor condition, and the overall grade of America's infrastructure is "D+", with an estimated cost of $1.6 trillion to improve the situation [5, 6]. Infrastructure management agencies are shifting their priorities away from building new structures towards inspection, assessment and maintenance of the existing infrastructure [53]. Before appropriate rehabilitation can be prescribed, the condition of a structure must assessed. On the other hand, increased use of performance-based specifications requires accurate in-place estimates of new structures' quality and strength, e.g. new pavement thickness control. Therefore, non-destructive test (NDT) techniques that can detect, localize and characterize damage and flaws in the infrastructure are of great interest to infrastructure management agencies.

Visual images that describe the location, size and shape of embedded damage or flaws provide a direct way to help engineers evaluate the condition of concrete structures. Many individual data are needed to construct a single image, however, and the inherent large size of concrete structures results in an enormous amount of data needed to construct an adequate image.

Most NDT techniques require good contact between the sensor and tested concrete surface to obtain reliable data. But the surface preparation is often very time- and labor- consuming due to the rough surface or limited access of concrete structures. One approach to speed up the data collection process is to eliminate the need for physical contact between the sensor and tested structure. Commonly used non-contact techniques include radiography with penetrating radiation, RADAR with electromagnetic pulsed waves and infrared thermography [2]. However, these techniques have significant, inherent drawbacks that limit the ultimate potential for detecting and imaging flaws within concrete structures. Radiographic techniques are limited by safety and cost issues and require access to opposite sides of the structure. Since electromagnetic waves are a function of the dielectric properties, as opposed to mechanical properties of the material, they are strongly reflected from embedded steel reinforcing bars, often masking the signals from underlying flaws. Also, electromagnetic waves are disturbed by varying moisture and salt contents within the concrete, thereby complicating the interpretation of RADAR images for flaw detection and identification. Thermography is very efficient for detecting delaminations in large structures, but it is sensitive to weather and surface conditions and does not provide information about the depth of defects [11]. In addition,

all these non-contact techniques require expensive equipment, and the test results are not directly related to the mechanical properties of materials. On the other hand elastic wave-based test methods, such as ultrasonic scanning, enable inspection well below the surface of the concrete structure, offer direct information concerning the effective elastic constants and are sensitive to the presence of damage and flaws. Elastic wave-based test techniques have been successfully applied to measure pavement slab thickness [42, 61], estimate the depth of surface-opening cracks in concrete [35, 65], and monitor setting and strength gain in early-age concrete [43, 47]. However, the use of elastic wave data to create visual images is severely limited by the required physical contact and coupling of the transducers. This contact introduces disturbing experimental variations, and significantly reduces efficiency of measurement [11].

Therefore, it is necessary to search for advanced NDT techniques that will provide efficient, low-cost and reliable condition assessment to the existing concrete infrastructure. Air-coupled sensing has undergone rapid development in recent decades, especially in guided wave detection for layered structures [71]. With the advantages of being non-contact and having elastic wave based characteristics, air-coupled sensing has the potential to be an excellent candidate for NDT application in concrete structures.

1.2 Objectives and Approach

The objective of this research is to develop non-contact NDT techniques that enable accurate imaging of important damage and flaws inside concrete structures. The following objectives, and corresponding approaches, are proposed:

1. *Theoretical study of the propagation of leaky Rayleigh waves in a fluid-solid half-space system.* A fluid-solid half-space model is used to simulate a concrete element in contact with air. The analytical solution to the Lamb's problem (response to an impact point loading) is determined with regard to the leaky Rayleigh wave response in air. This study provides necessary theoretical background for air-coupled sensing leaky Rayleigh waves in concrete. The theory is also extended to the underwater NDT applications.

2. *Feasibility study of air-coupled sensing technique for concrete.* With the guidance of the theoretical analysis, the excitability of leaky Rayleigh waves by impact point loads is investigated. The effects of direct acoustic waves and ambient noise is also studied. The specifications of air-coupled sensors is determined.

3. *Development of sensitive, non-contact elastic wave detection techniques.* The application of air-coupled sensors to both newly developed and existing tests for concrete will be investigated.

4. *Development of a practical testing system and construction of an effective data presentation format.* The test data obtained from the developed non-contact sensing test schemes will be presented in images, so that structural engineers can use them to locate, size and characterize damage or flaws in a concrete structure. The most sensitive and reliable parameters will be used to construct the images.

1.3 Outline of the Thesis

The thesis first gives background information about common defects in concrete structures and the corresponding NDT techniques (chapter 2). Chapter 3 presents the fundamentals of stress wave propagation in solids, and reviews the currently available NDT techniques for concrete structures.

Chapter 4 is devoted to the detailed theoretical analysis of wave propagation in a fluid/solid half space system. Closed-form solutions are obtained to the Lamb's problem in the fluid/solid system. Applications of the theory are extended to air-coupled sensing and underwater NDT methods.

Chapter 5 discusses the testing setup and equipment used for air-coupled sensing in concrete. Preliminary experimental results are presented to show the effectiveness of air-coupled surface wave sensing techniques. Air-coupled sensors are then applied to surface wave detection in concrete pavements with SASW and MASW approaches (chapter 6).

Chapter 7 describes air-coupled impact-echo tests, and shows the 2-D imaging technique for detecting delaminations and duct voids in concrete. Future research is proposed in chapter 8.

2 Common Defects in Concrete Structures

The deterioration of concrete structures can be described by a variety of physical and environmental damage modes. The common flaw types include delamination/spalling, cracks and voids/honeycombings, as illustrated in Fig. 2.1. Existence of the flaws in concrete severely affects durability, service life and, in some cases, structural integrity of concrete structures. Early detection of the flaws is the most effective way to reduce maintenance and rehabilitation costs and improve public safety.

2.1 Delamination

Delamination is the most serious problem affecting the service life of reinforced concrete bridge decks and parking garage slabs. Effective maintenance of these structures requires detection of delaminations at early ages so that repairs can be made before large-scale deterioration occurs.

For concrete bridge decks, the dominant deterioration mechanism is the chloride-ion-induced corrosion of reinforcing steel, which accounts for approximately 40% of the current highway bridge repair and rehabilitation costs [69]. Corrosion-induced delaminations are horizontal cracked planes in concrete bridge decks that form when reinforcing steel in the deck corrodes. Corrosion is greatly accelerated by the presence of chloride ions (from deicing salts) that have diffused through the cover layer of concrete and arrived in a moist location at the reinforcing steel surface. The corrosion products significantly increase the volume that the reinforcing steel occupies in the concrete. The reinforcing steel volume expansion applies disruptive stresses to the surrounding concrete, and leads to cracking. Delamination cracking generally propagates in the plane of the top reinforcing steel layer and parallel to the surface, which is typically 5 cm to 15 cm below the bridge deck surface [64]. The delamination will eventually propagate to the surface, causing large area spalling. The cost to repair or rehabilitate will be very high at this late stage.

NDT techniques for delamination detection include the chain drag test (sounding), thermography, GPR and Impact-Echo. Each method has advantages and limitations. The chain drag test involves dragging a heavy chain over small areas of a bare concrete surface, while a technician listens to the acoustic response of the surface. Chain drag testing is very easy to apply, but it does

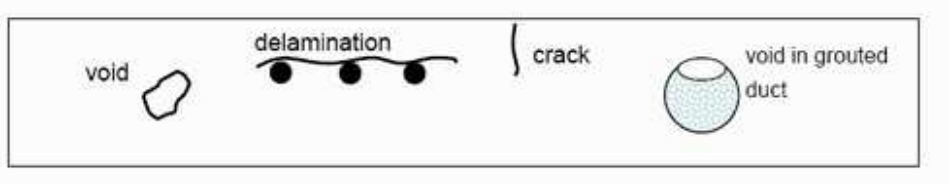

Figure 2.1: Flaws in a concrete slab

not work for deep delamination and on concrete bridge decks with asphalt overlays. The accuracy of test result largely relies on operator's experience. The limitation of thermography and GPR has been discussed in Chapter 1. Impact-Echo test is very effective in detecting and estimating depth of delaminations. More detail will be provided in Chapter 3.2

2.2 Cracks

Cracks can be caused by drying shrinkage, thermal expansion, freeze-thaw cycling, chemical reaction or mechanical actions, such as fatigue or overloading. The existence of cracks not only affects a structure's serviceability, but also reduces the durability. Cracks allow ingress of deleterious chemicals, such as water-borne deicing salts, leading to corrosion of steel reinforcement. Steel corrosion causes expansion, which further accelerates the rate of corrosion. A distinct single surface-breaking crack is a common and significant defect that can eventually lead to failure of concrete structures. Determining the size (width and depth) of cracks is essential to integrity assessment of concrete structures.

The width of surface-breaking cracks can be visually measured at the surface. However, crack depth determination is still a challenging topic. Several studies on the P-wave time-of-flight technique to predict surface-breaking crack depth in concrete have been reported, but this method is not effective when the crack tip is ill defined and the crack is tightly closed [65]. A self-compensating surface wave transmission coefficient measurements proposed by Popovics and Song et al. [49, 65] shows high sensitivity to realistic cracking in concrete. The relation between crack depth in concrete and surface wave transmission coefficient from the crack has also been established.

2.3 Voids and Honeycombing

Voids and honeycombing are usually caused by poor consolidation of concrete during construction. Voids due to incomplete grouting in post-tension ducts leave tendons vulnerable to corrosion, and can eventually lead to failure of the structure. This issue led to a ban on the construction of post-tensioned bridges by the UK's Department of Transport in 1992. Therefore, there is a critical need to develop reliable and effective methods for detecting grout voids in post-tensioned ducts.

The commonly used NDT techniques for void detection include Impact-Echo test [31], radiography and GPR. Guided waves were also investigated for inspection of grouted tendons [7], but dispersion and multiple modes of guided waves make signal analysis very complicated.

3 NDT Methods for Concrete Structures

3.1 Properties of Stress Waves

3.1.1 Waves in an Elastic Half Space

Several types of stress waves can propagate in a solid. In an elastic half space, body waves travel within the body, and surface waves (also called Rayeligh waves or R-waves) travel along the free surface of the half space. Body waves include P-waves (compression waves) and S-waves (shear waves). Ultrasonics methods based on body waves, especially P-waves, are the most commonly used NDT techniques in civil engineering.

The velocities of wave propagation depend on elastic constants and mass density of the solid. In solids, C_{P} and C_{S} are given by

$$C_{\mathrm{P}} = \sqrt{\frac{\lambda+2\mu}{\rho}} = \sqrt{\frac{E(1-\nu)}{\rho(1-2\nu)(1+\nu)}}, \tag{3.1}$$

$$C_{\mathrm{S}} = \sqrt{\frac{\mu}{\rho}} = \sqrt{\frac{E}{2\rho(1+\nu)}}, \tag{3.2}$$

where λ, μ are Lamé's constants, E and ρ are Young's modulus and density, and ν is Poisson's ratio. The Rayleigh wave velocity C_{R} can be solved from the bi-cubic equation with respect to C

$$(2-\frac{C^2}{{C_{\mathrm{S}}}^2}) - 4(1-\frac{C^2}{{C_{\mathrm{P}}}^2})(1-\frac{C^2}{{C_{\mathrm{S}}}^2}) = 0. \tag{3.3}$$

The Rayleigh wave velocity C_{R} is given by one of the roots of C. C_{R} is slightly slower than the shear wave velocity. The relations between them are expressed by equations

$$\frac{C_{\mathrm{S}}}{C_{\mathrm{P}}} = \sqrt{\frac{1-2\nu}{2(1-\nu)}}, \tag{3.4}$$

$$\frac{C_{\mathrm{R}}}{C_{\mathrm{S}}} \approx \frac{0.87+1.12\nu}{1+\nu}. \tag{3.5}$$

For concrete, ν typically varies from 0.15 to 0.25, and C_{R} ranges from 90% to 92% of C_{S} and from 58% to 53% of C_{P}. C_{P} typically ranges from 3800 m/s to 4500 m/s for sound concrete, and C_{R} from 2100 to 2600 m/s. The motion resulting from R-waves is restricted to a region near the surface, and decreases exponentially in amplitude away from the surface. The penetration depth of R-waves is about twice the thickness of wavelength, λ_R. Therefore the R wave penetration depth is inversely related to the frequency of the wave.

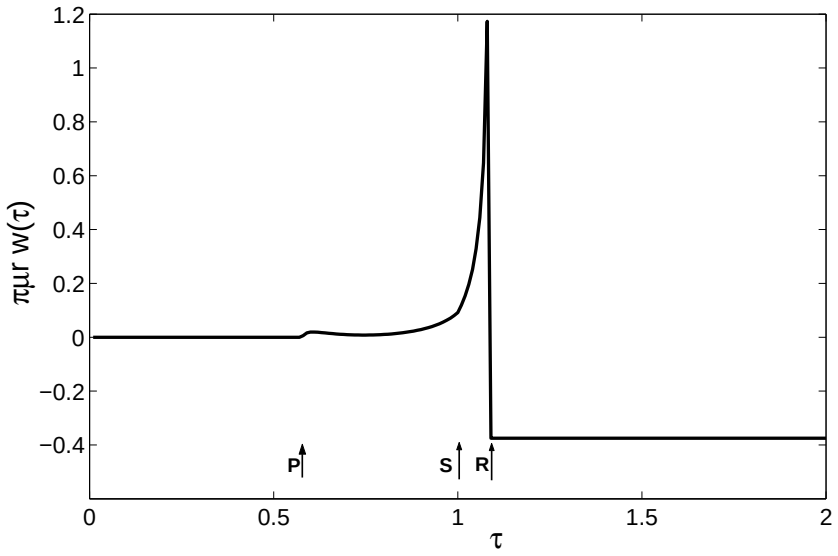

Figure 3.1: Vertical displacement at the free surface of an elastic half space resulting from a unit step load at a point. Arrival time of P-,S- and R-waves are denoted [46].

The response of an elastic half-space to a surface impact source was first studied by Lamb [34]. Since then this class of problems was called Lamb's problem. Pekeris [46] derived the closed-form expression for displacements at the free surface for an elastic half-space subject to a transient (step function) normal point load. The normalized vertical displacement $\pi\mu r w(\tau)$ is shown in Fig. 3.1 as a function of dimensionless time $\tau = tC_{\mathrm{S}}/r$, where r is horizontal distance from the source.

It can be seen that very large amplitude occurs near the R-wave arrival time. Therefore, R-waves are easily generated in a solid by a transient point source, and more readily sensed than P- and S-waves due to the large amplitude. The only limitation of R-waves is the limited penetration depth; the disturbances are confined to the near-surface region of thickness, approximately twice λ_R. However, the penetration depth may be increased by lowering the frequency. Assuming $C_{\mathrm{R}} = 2200$ m/s, a wave frequency of 30 kHz results in R-waves that penetrate 150 mm. Deeper penetration can be obtained by using lower frequency. A typical instrumented hammer can generate signals up to 10 kHz on a hard concrete surface, while a specially-designed impactor can generate signals up to 20 kHz. Thus, the penetration depth of R-waves can be controlled by choosing an appropriate impact source.

In addition to the large amplitude, R-waves have other advantages over P- and S-waves. For waves generated by a point source, R-waves attenuate with distance on the order of $r^{-\frac{1}{2}}$ along the free surface, while P- and S-waves attenuate on the order of r^{-2} [54]. Figure 3.2 illustrates the particle motion of Rayleigh waves in comparison to P- and S-waves. At the distance of 2.5 wavelength from the source, approximately 67% of the induced energy from an impulse point source on a homogenous half-space propagates as Rayleigh waves [54]. Thus, R-waves can be detected even at large distance. Unlike P-waves, which are dominated by in-plane motions, R-waves result in large amplitude out-of-plane motions, which is usually the quantity being measured at the free surface.

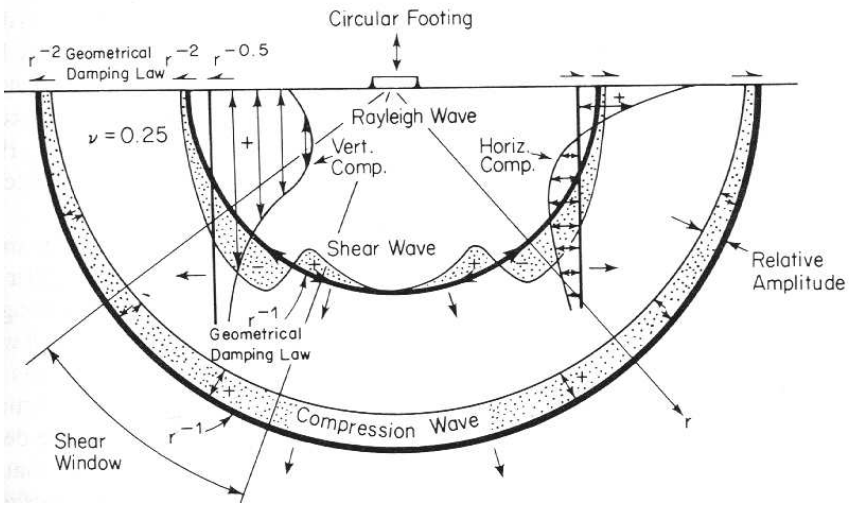

Figure 3.2: Distribution of seismic waves from a point source on a homogeneous, isotropic, elastic half-space. The particle motion is visualized at a distance of approximately 2.5 wavelengths from the source. The different wave types are drawn in proportion to the velocity of each wave, from Richard et al. (1970)[54].

3.1.2 Guided Waves in Layered Structures

Guided waves exist in layered media and are formed by the interaction of reflected P- and S-waves at the interface between layers. Guided waves are usually dispersive, meaning that the phase velocity is frequency dependent.

Rayleigh waves represent a special type of guided wave propagating along the surface of a homogenous half-space [52]. Rayleigh waves are non-dispersive in the homogenous medium, but Rayleigh-type surface waves propagating in layered medium are dispersive. Dispersion curves reflect properties of the layered structures (elastic constants and boundary conditions), and thus can be used for structure characterization. Dispersion of surface waves is the theoretical basis of the SASW (Spectral analysis of surface waves) and MASW (Multi-channel analysis of surface waves) techniques.

Lamb waves are guided waves in plates. Lamb wave analysis is often used to determine the top layer thickness and material properties of pavements. The inversion of deeper embedded layers is based on the full phase velocity spectrum of surface waves [56].

3.1.3 Waves in Fluid-Solid Half Spaces

The problem of wave propagation within two half spaces in contact was discussed by Ewing et al.[23]. Viktorov [68] gave a comprehensive study of so called “leaky” Rayleigh wave propagation along the interface of fluid-solid half spaces. In most air-solid contact cases, solutions drawn from a free surface solid half space model (solid-vacuum) can accurately simulate the propagation of elastic waves in the solid because the effect of air on the solid is very small. However, when the acoustic impedance ratio of the fluid to solid increases, or wave propagation in the fluid is concerned, the two half space model should be employed.

In a fluid/solid half space system, the wave field in the solid is similar to that in the free surface

solid half space. All body waves, head waves and Rayleigh waves exist in the solid. In the near interface region, there also exists an interface wave, called the Scholte wave, propagating along the interface in both the fluid and solid. The propagating P-, S- and Rayleigh waves in the solid cause a small disturbance at the interface, resulting in out-of-plane surface motion. The resulting surface motion at each point causes an acoustic wave to "leak" into the surrounding fluid, assuming the fluid has lower acoustic impedance than the solid. The superposed leaky waves that emanate from each point in motion form leaky P-, S- and Rayleigh wave wavefronts. In addition, a direct acoustic wave propagates in the fluid with a hemi-spherical wavefront.

Properties (velocity, amplitude and dispersion ect.) of leaky waves are affected by both the fluid and solid. The fluid is usually a homogeneous material that has uniform distribution in space, and the density and velocity are easy to determine. Therefore, material properties of the solid can be indirectly obtained by measuring leaky waves. Material variation of the solid influences leaky waves in the same way as it affects ordinary waves in the solid-vacuum cases. This provides the basis of air-coupled sensing techniques. In chapter 4, wave propagation in a fluid/solid half space system is analyzed in detail.

3.2 Stress Wave-Based NDT Methods

The stress wave based NDT techniques recommended by ACI228.2R-95 [2] for concrete structure inspection include Ultrasonic Pulse Velocity (UPV), Surface Wave Spectral Analysis (SASW), Impact-Echo and Impulse Response methods. Because the large difference of acoustic impedance between concrete and air causes strong wave reflection at interfaces, stress wave based NDT methods are most commonly used for air-filled crack and void detection in concrete.

3.2.1 UPV

The UPV test, one of the oldest NDT methods for concrete, is based on measuring the travel time of an ultrasonic P wave pulse over a known path length [2]. From Eq. (3.1), the P wave velocity in a solid depends on the mass density ρ and the elastic constants of the solid. Thus, by determining C_{P} at different locations in a structure, it is possible to measure the uniformity of the concrete [2]. It has been generally accepted that pulse velocity can be a good indicator of strength gain of concrete at early ages.

The instrument for UPV test is called the V-meter in the US or PUNDIT in the UK, and includes a pulser unit and a pair of transducers. The transducers are coupled to the test surfaces using grease or gel couplant to obtain a stable result. Transducers with 50kHz resonant frequency are the most commonly used. Lower (20kHz) or higher (100kHz) frequency transducers can be used for thicker or thinner concrete sections.

The UPV test is very easy to apply and successful for finding internal voids and transverse cracks. However, the need for access both sides of structure considerably limits wide application of the method. Moreover, P-wave transmission time is the only output of UPV test, which does not provide information about the depth of defects.

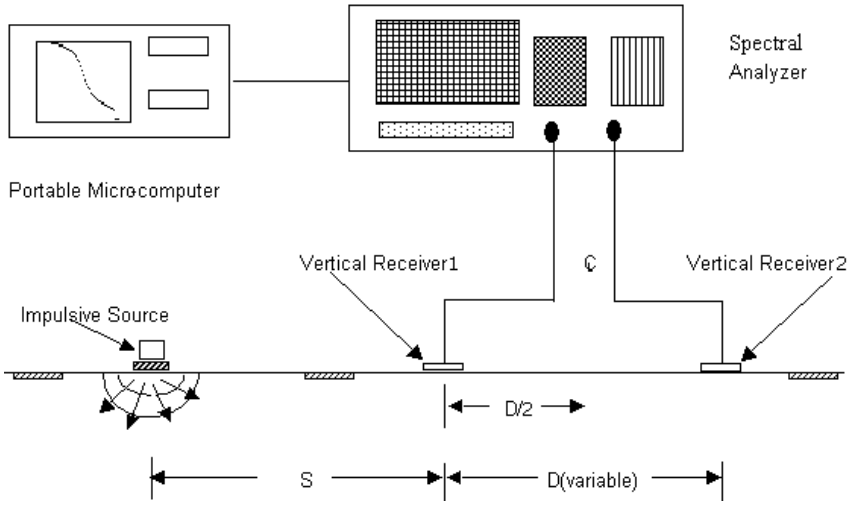

Figure 3.3: Schematic of SASW test. (After ACI228.2R-98[2])

3.2.2 SASW

The spectral analysis of surface waves technique (SASW) was developed initially for geotechnical applications at the University of Texas at Austin in 1980s. The technique utilizes the dispersive property of surface waves; the frequency-dependent phase velocity of the surface wave is a function of the material properties at different depths. Thus subsurface materials can be evaluated without direct access. The SASW method has been successfully applied to determine the stiffness profile of soil sites, asphalt and concrete pavement systems. In recent years, the method has been extended to measurement of concrete structures [33].

In SASW analysis, a surface wave is generated on the structure using an impact source, as illustrated in Fig. 3.3. The surface wave motion is then measured by two transducers a certain distance away from the source. The signals measured at each transducer are then analyzed, and phase velocity is calculated according to the phase difference between signals from the two transducers. The elastic profile for the structure can be estimated from this obtained dispersion curve, which plots Rayleigh wave phase velocity vs. frequency. However, since only two receivers are used in the SASW test, the SASW method cannot separate different modes of propagation over a layered system, and therefore measures a superposition of all propagating waves at the specific receiver locations.

The application of SASW method to concrete is still limited to estimate the stratification profile of pavement-like structures. The complicated signal processing and inversion procedure limit further application to concrete defect detection.

3.2.3 MASW

The Multichannel Analysis of Surface Waves (MASW) method was developed at the Kansas Geological Survey (KGS)[44] in late 1990s. The MASW method uses multiple sensors to record the complete wave field and resolve the different wave modes. With this technique, the fundamental and higher mode dispersion curves can be extracted [44, 56, 57, 59]. Because multi-channel recording

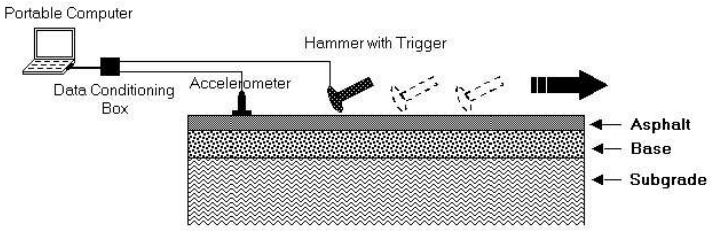

Figure 3.4: Schematic description of the MSOR measurement set-up.(after Ryden[56])

and processing schemes are employed, the MASW test gives reliable results even in the presence of higher modes of surface waves and various types of ambient noise.

However, satisfactory coupling between receivers and the test surface is difficult to achieve. It is time-consuming to couple many sensors in the MASW test. In addition, it is expensive to use multiple sensors and multi-channel data acquisition equipment. One alternative is to use the MSOR procedure (multi-channel simulation with one receiver) [59], where only one receiver is used. The receiver is fixed at one position, while the source moves consecutively at equal spacing. One disadvantage of MSOR is that it takes many steps to collect a whole set of data. Air-coupled sensors may provide a solution to the surface coupling problem.

The testing scheme of the MSOR method is shown in Fig. 3.4. Figure 3.5 shows multi-channel records and MASW analysis results from an asphalt pavement [58]. The Lamb-wave dispersion curves for a free plate are plotted on the frequency-phase velocity image.

3.2.4 Impact-Echo

The Impact-Echo method was first developed at the National Institute of Standards and Technology (NIST) in 1980s, and then further developed at Cornell University under the direction of Mary Sansalone. The principle of the Impact-Echo technique is illustrated in Fig. 3.6. A transient stress pulse is introduced into a test object by an impact force applied on the surface. The generated transient waves are reflected by internal interfaces or external boundaries. The surface displacement is measured by a receiving transducer and analyzed in the frequency domain. The distance to the reflecting interface D is related to the P wave velocity C_{P} and the peak frequency f by

$$D = \beta \frac{C_{\mathrm{P}}}{2f}, \tag{3.6}$$

where β is a factor related to section shape. According to the standard test method, for plates, $\beta = 0.96$. A recent study proposes that β is related to the zero group velocity frequency of S_1 mode Lamb waves in a plate structure [27], and depends on Poisson's ratio ν of concrete.

The impact-echo method is very successful in determining slab thickness, and detecting depth of flaws in plate-like structure members (e.g. pavements or bridge decks). Application to bar-like structural elements, such as beams or columns, is more difficult because signal analysis is complicated due to cross-sectional boundary effects. The impact-echo is a point measurement method, i.e., it only measures the concrete thickness at the test point, which limits its ability for imaging.

Commercial Impact-Echo systems are available which combine the hardware for generating

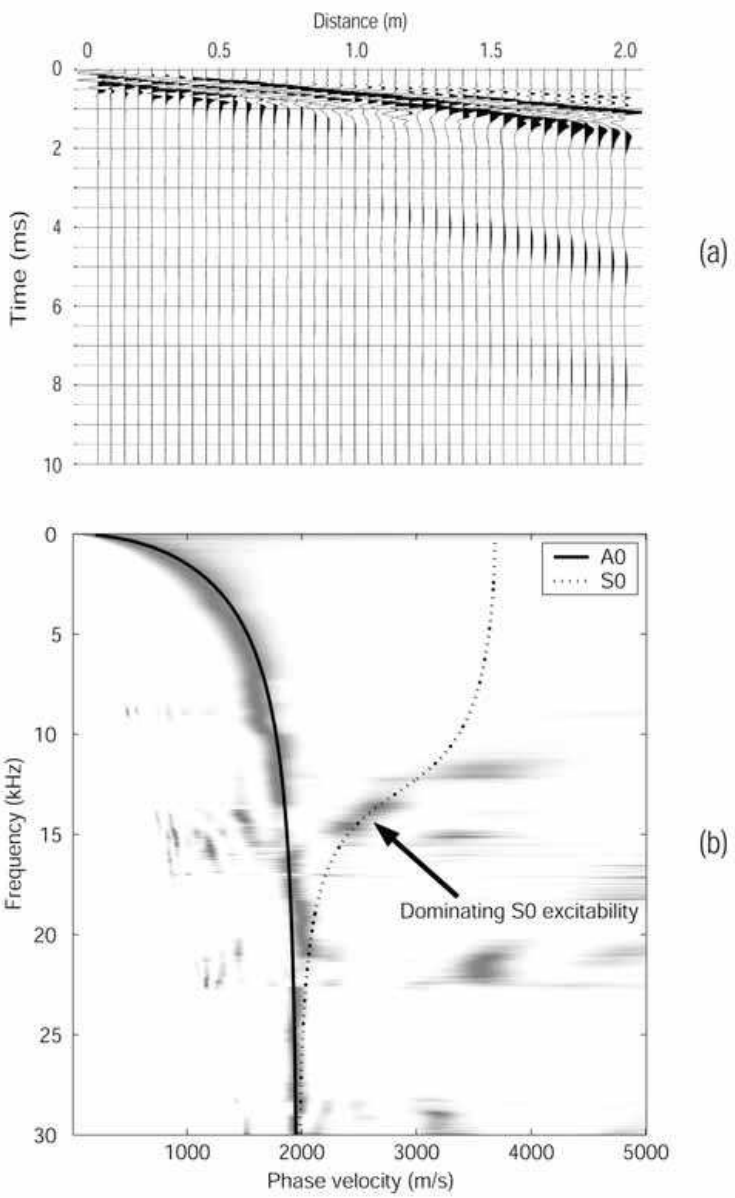

Figure 3.5: MASW test results from an asphalt pavement. (a) Collected time domain signals; (b) the frequency-phase velocity spectrum generated by MASW analysis.(after Ryden[58])

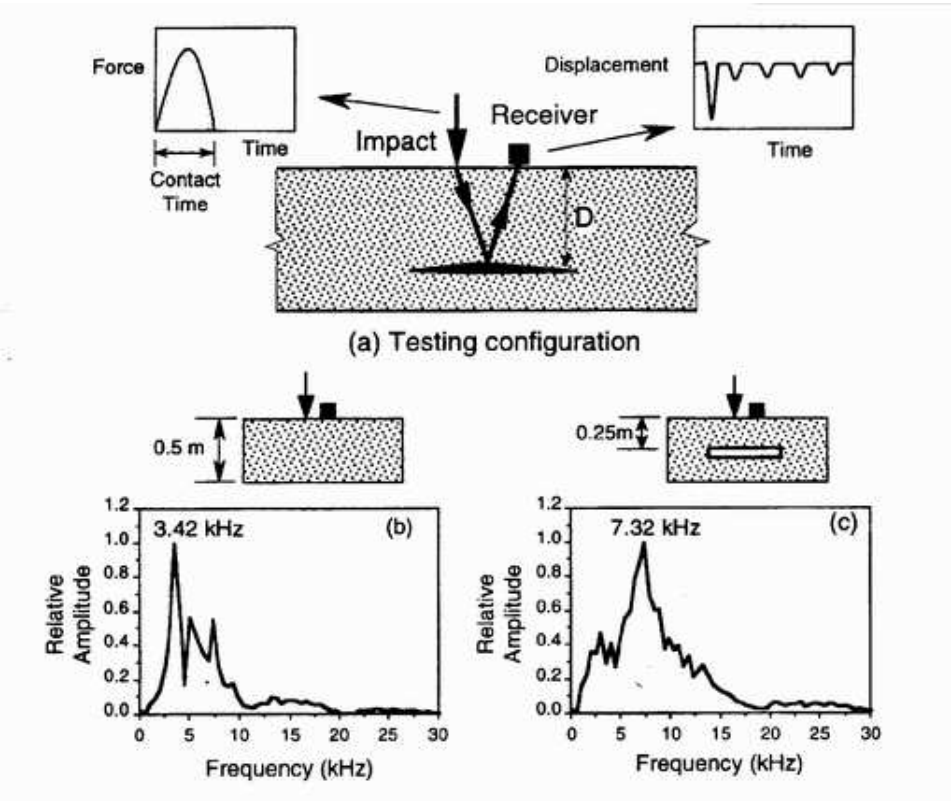

Figure 3.6: Principle of impact-echo test. (a) Schematic of impact-echo method; (b) amplitude spectrum for test of solid slab; and (c) amplitude spectrum for test over void in slab (after ACI228.2R-98[2])

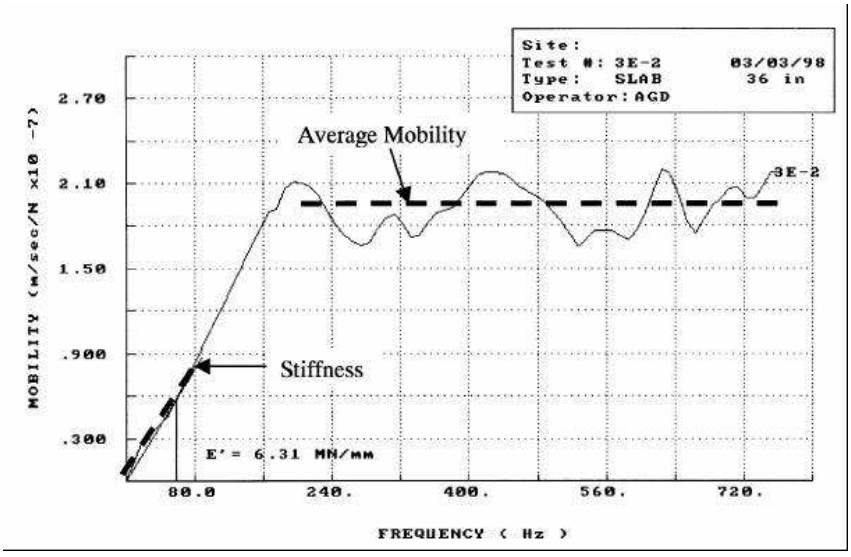

Figure 3.7: Typical mobility plot for sound concrete [18].

waves and measuring signals, as well as signal processing software to aid in data analysis.

3.2.5 Impulse Response

The impulse response (IR) method was originally developed from the vibration method for pile integrity testing [17] and known as the dynamic mobility or impedance method. In the last 30 years, the method has been extended to the inspection of concrete structures other than piles, particularly plate-like elements such as floor slabs, walls and large cylindrical structures [18, 19]. The detailed description of IR method can be found in literature [2, 18, 19].

The IR is a low-strain NDT method. It uses a force hammer to send stress waves through the tested element. The impact force can be measured by a built-in load cell in the hammerhead. Response to the impact force is normally measured using a velocity transducer (geophone). This receiver is preferred because of its stability at low frequencies and its robust performance in practice. Both the time records for the hammer force and the geophone velocity response are recorded and processed in a computer. The resulting transfer function between velocity and force $V(f)/F(f)$ is referred as the mobility of the element. The integrity of concrete can be obtained from the following measured parameters: dynamic stiffness, mobility and damping, peak/mean mobility ratio [18].

Figure 3.7 shows a typical mobility plot for sound concrete. The inverse of slope of the mobility plot below 50 Hz defines the dynamic stiffness of the test element, which is an important parameter to evaluate concrete quality, thickness and element support condition. Mobility and peak/mean mobility ratio are also sensitive indicators to presence of delaminations, cracks or voids.

Commercial impulse response equipment is available. There has been many successful applications to large concrete structure. The IR test is usually conducted on a 2-D test grid with grid spacing between 30 cm and 90 cm, depending on detail required for analysis of the tested structure. Contour plots of variations in dynamic stiffness or mobility enable quick condition evaluation of these large areas.

3.2.6 Stress Wave Based Imaging Techniques for Concrete Structures

Ultrasonic transmission tomography has been used as an imaging technique for concrete structures. The tomography method measures times-of-flight of ultrasonic waves along different paths through the material, as illustrated in Fig.3.8. Variation in internal material properties affects the travel time of ultrasonic waves along each path. Tomographic imaging software is used to reconstruct the section image by combining the data measured at different angles through the section. Sufficient data are needed in order to assure convergence to the correct solution. Greater numbers of measurements and intersecting ray paths result in more accurate tomograms [38]. Figure 3.9 shows the velocity map of a concrete beam containing two partially filled ducts. Voids and poor concrete regions are indicated by low velocity regions.

The synthetic aperture focusing technique (SAFT) superimposes numerically many pulse-echo signals measured at several positions to create a high resolution image. Signals are focused to every image point, and structural noise is suppressed by spatial superposition [62]. The SAFT result is a three-dimensional map of the backscatter intensity from inside the structure, which may then be interpreted in area (C-scan) or depth (B-scan) slices. Indications of significant backscatter indicate locations of interior air-filled voids and cracks.

Both tomographic and SAFT methods require collection of large amounts of data to reconstruct adequate images, which is computationally and labor intensive. SAFT also requires good coupling between transducers and the test surface, which is difficult to apply to practical inspection of concrete due to the inherent rough surface of concrete. In addition, only larger defects (> 20cm in size) can be detected reliably [48].

Recently, the scanning Impact-Echo (SIE) method has been reported for duct inspection in concrete slabs [67, 70]. An automated Impact-Echo scanning system was developed at Federal Institute for Materials Research and Testing of Germany (BAM) to perform Impact-Echo tests along a line or over an area. SIE helps to improve precision of point tests and provide correction for geometry effects.

3.3 Ground Penetrating RADAR

The Ground Penetrating RADAR (GPR) method sends electromagnetic waves pulses into pavement structures and measures the reflection of waves from interfaces between materials of dissimilar dielectric properties. A RADAR antenna, which is either dragged across the surface or attached to a survey vehicle, transmits short pulses of electromagnetic energy into the pavement structure. No direct contact or surface preparation is required, which allows for rapid scanning.

Reflections from interfaces below the surface are captured by the same antenna. The received signal contains information about wave velocity and attenuation. Electromagnetic waves are transmitted, reflected, and refracted through material in an analogous fashion to stress waves, but their behavior is governed by the dielectric constants, rather than the elastic properties, of the medium. Similar to the ultrasonic test described above, the depth of reflecting interfaces can be determined from the wave velocity C and the round trip travel time t. The velocity of an electromagnetic wave

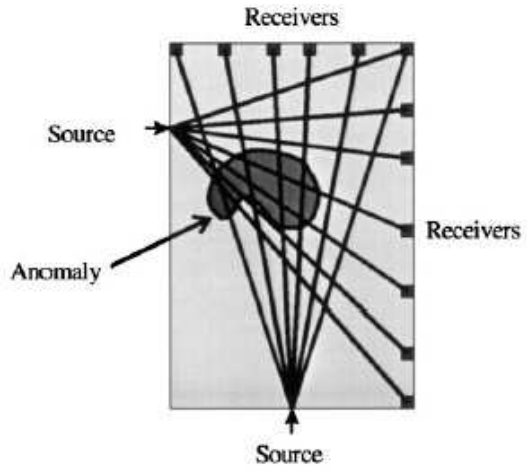

Figure 3.8: Ultrasonic tomographic ray path.(after Martin et al. [38])

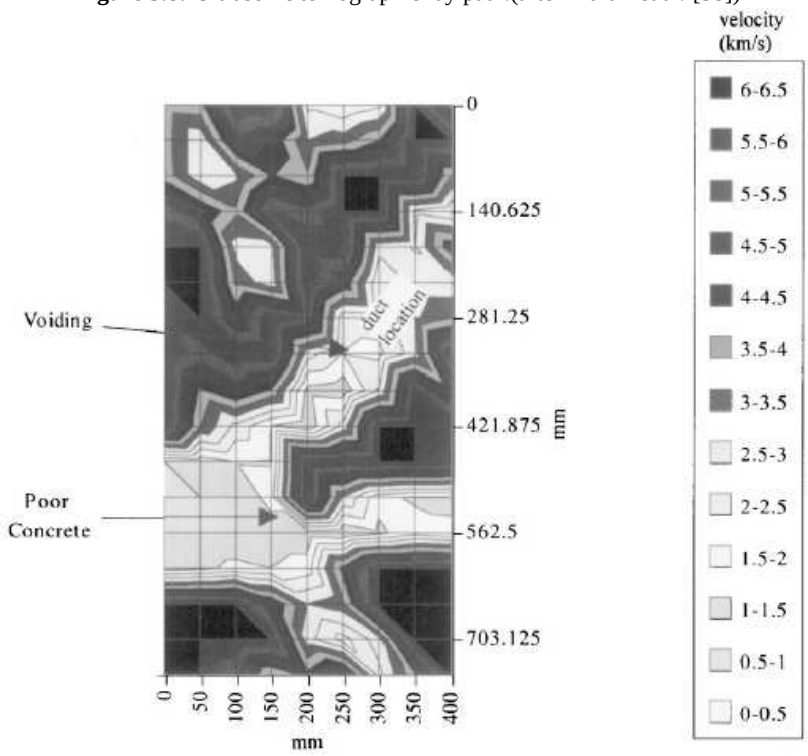

Figure 3.9: Velocity tomograph reconstructed from data collected from a reinforced concrete beam. Regions containing ducts, voids and poor concrete are identified as low velocity regions.(after Martin et al. [38])

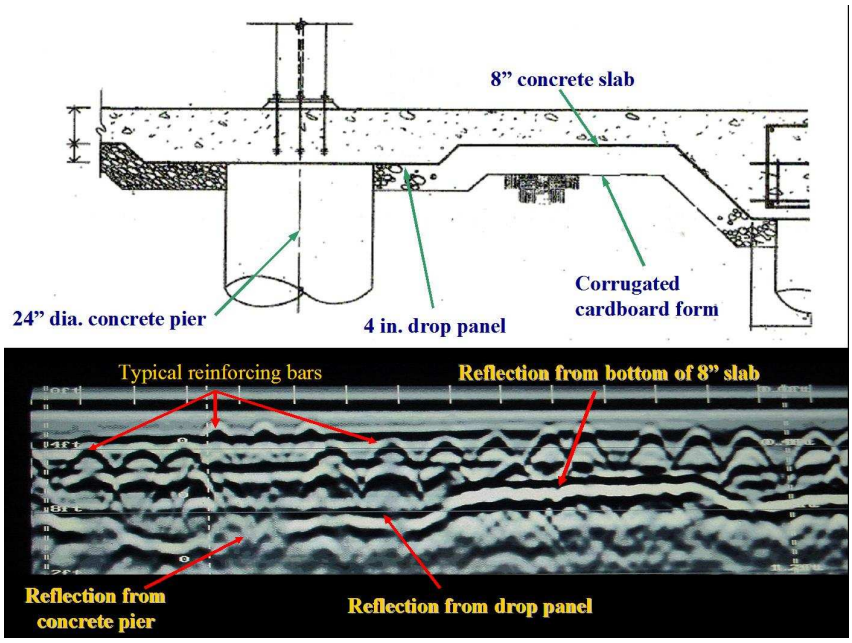

Figure 3.10: A GPR image of concrete structure [22].

C in a dielectric material is determined by the relative dielectric constant ε_r:

$$C = C_0/\sqrt{\varepsilon_r}, \tag{3.7}$$

where C_0 is the speed of light in air ($\approx 3 \times 10^8$ m/s) and ε_r is the relative dielectric constant of a material.

The contrast in dielectric constant determines the amount of reflected energy at the interface between two dissimilar materials. The reflection coefficient is given by the following equation [10, 16]

$$\rho_{12} = \frac{\sqrt{\varepsilon_{r1}} - \sqrt{\varepsilon_{r2}}}{\sqrt{\varepsilon_{r1}} + \sqrt{\varepsilon_{r2}}}, \tag{3.8}$$

where ρ_{12} = reflection coefficient, $\varepsilon_{r1,2}$ = relative dielectric constant of Material 1 and Material 2 respectively.

An important difference between GPR and stress-wave methods is the amplitude of the reflections at a concrete-air interface. Almost 100 percent of stress waves energy is reflected at the concrete-air interface because the acoustic impedance of air is negligible compared with concrete. On the other hand, the mismatch in dielectric constants at a concrete- air interface is not so large, and only about 50 percent of the incident energy is reflected at a concrete-air interface. This condition results in two significant differences between GPR and stress-wave methods. GPR is not as sensitive to the detection of concrete-air interfaces as are stress-wave methods. However, because the energy is not totally reflected at a concrete-air interface, GPR is able to penetrate beyond such an interface and detect materials below the interface [2].

GPR is especially effective for locating steel members within the concrete as there is complete reflection of electromagnetic waves at the metal/concrete interface. On the other hand, strong reflections from embedded metals can obscure weaker reflections from other reflecting interfaces that

may be present, and reflections from reinforcing bars may mask reflections from greater depths.

GPR results are usually presented as B-scan or C-scan images, which are more readily understood by NDT Engineers. Figure 3.10 shows a GPR B-scan image of a concrete bridge. Reflections from rebars and bottom surfaces are clearly identified. Powerful digital processing developments have allowed these data to be presented in real time, allowing field interpretations of results [9]. The background and new development of GPR testing for concrete is reviewed by Bungey[9].

3.4 Non-contact Sensing Techniques

Two approaches can be used for non-contact stress wave sensing in concrete: optical detection with a laser and acoustic detection with air-coupled sensors.

Optical techniques use a laser to detect propagating waves in a solid by providing sensitive measurement of motion at a point on the surface. The broad bandwidth and high sensitivity of laser vibrometers enable researchers to perform precise measurement without contacting the surface. However, practical application of laser sensing to concrete is hindered by the naturally rough surface of concrete that causes poor light reflection and lowers laser detection sensitivity. In the case of one-sided measurements, since the surface motion associated with Rayleigh waves is usually much larger than that of body waves, it is more practical to detect surface waves than body waves in concrete with a laser. Popovics et al. [50] demonstrated practical laser detection of propagating surface waves in concrete with a normal unprepared surface. Although it is a non-contact method, the signal amplitude measured by a laser vibrometer is considerably affected by the surface condition. Thus for untreated concrete surfaces, it is impossible to compare signals detected at different locations. Furthermore, due to the complicated and expensive equipment, laser detection is so far still limited to laboratory research purposes.

Air-coupled ultrasonic sensing has gained popularity since its first use in 1970s for propagating waves in solids [14]. There have been many successful applications of air-coupled sensors to detect waves in metals and composite materials. The air-coupled sensors used to detect body and guided ultrasonic waves are in the range of 50kHz-1MHz, above which air attenuation and scattering effects are unacceptable. For concrete testing, a flat frequency response below 100kHz is preferred. Microphones are sensitive acoustic sensors in this frequency range (usually up to 25kHz) and can serve as excellent air-coupled sensors that detect low frequency leaky waves in concrete. Compared with laser detection, air-coupled sensing is relatively insensitive to the surface condition of concrete. Thus, it is possible to study the attenuation of leaky waves in concrete. There are several concerns regarding the use of air-coupled sensors to detect leaky waves in concrete:

1. *What sensitivity is required for air-coupled sensors or microphones to detect leaky waves in concrete?* Because of the huge difference of acoustic impedance between air ($0.4kg/m^2s$) and concrete ($7 \sim 10 \times 10^6 kg/m^2s$), only a very little amount of wave energy leaks into air. Theoretical analysis is needed to determine the air pressure of leaky waves generated by a typical impact event applied to the surface, and then choose appropriate air-coupled sensors that meet the sensitivity requirement. Because leaky Rayleigh waves have large out-of-plane responses and attenuate slower with distance than leaky body waves, it is expected that leaky Rayleigh waves are more readily detected by air-coupled sensors.

2. *What is the effect of ambient noise?* If microphones are used for leaky wave detection, the ambient noise may reduce the signal-to-noise ratio. Theoretical and experimental studies should be performed to investigate the effect of ambient noise.

3. *How do leaky waves propagate in air and concrete?* In distinction to laser measurement, which gives direct measurements of surface motion, air-coupled sensing methods measure the surface motion of solids indirectly from the leaky waves. Theoretical analysis of leaky wave propagation in a fluid-solid system is needed to provide necessary background for air-coupled sensing.

4 Elastic Waves in Fluid-Solid Halfspace System

The propagating leaky Rayleigh wave that emanates from a fluid-solid interface has been used as an effective means for surface and subsurface defect detection. With recent improvements in instrumentation, air-coupled transducers have been used for detection of leaky surface [74] and leaky guided waves [14]. With the advantage of non-contact sensing, air-coupled transducers provide an opportunity for efficient scanning and imaging of large civil engineering structures by detecting the leaky waves. Therefore, detailed study of leaky surface waves for this case is needed. Parts of research results in this chapter have been published in [73, 76]

4.1 Modelling Wave Propagation in Fluid-Solid Half Spaces

Extensive studies and applications of leaky surface waves have been reported during the past 40 years. A comprehensive study of Rayleigh waves and leaky Rayleigh waves has been given by Viktorov [68], where leaky Rayleigh waves at the interfaces of a solid half space with both a fluid layer and a fluid half space were investigated in great detail. Leaky Rayleigh waves propagate with a velocity slightly higher than the ordinary Rayleigh wave, and attenuate more intensively with distance due to continuous energy radiation into the fluid. It was initially believed that the leaky Rayleigh wave exists when the fluid wave velocity C_F is smaller than the leaky Rayleigh wave velocity C_{LR}. However, Mozhaev and Weihnacht [41] showed the actual threshold phase velocity for leaky Rayleigh wave existence was 1.45% lower than the acoustic wave velocity of the fluid. The character and existence conditions of leaky Rayleigh and Scholte waves were also investigated experimentally by Glorieux et al. [28]. The propagation of leaky Rayleigh waves under the influences of viscous damping and heat conduction at the fluid-solid interface was studied by Qi [51], who concluded that the effect of viscosity can be neglected for fluids with Reynolds number larger than 2500. For common fluids such as water and air at normal driving frequencies ($<$10MHz), the viscous effect of the fluid can be neglected because the Reynolds numbers are far above the critical value of 2500.

The response of leaky waves owing to a transient point loading is of great practical interest to non-destructive evaluation (NDE) researchers, especially in civil engineering, where an impulse hammer or a point impactor applied to the surface of the solid is often used as a transient wave source. 2-D and 3-D analytical solutions for a fluid-solid configuration subjected to implosive line and point sources in the fluid have been given by de Hoop et al. [20, 21]. However, for the case of the Lamb's problem in fluid-solid configuration, where a normal transient point load is applied at the fluid-solid interface, no closed-form exact solution has been reported so far.

In this study, Laplace and Hankel integral transforms are employed to derive the full analytical solution to the Lamb's problem in a fluid-solid half space system, where a point load, varying with

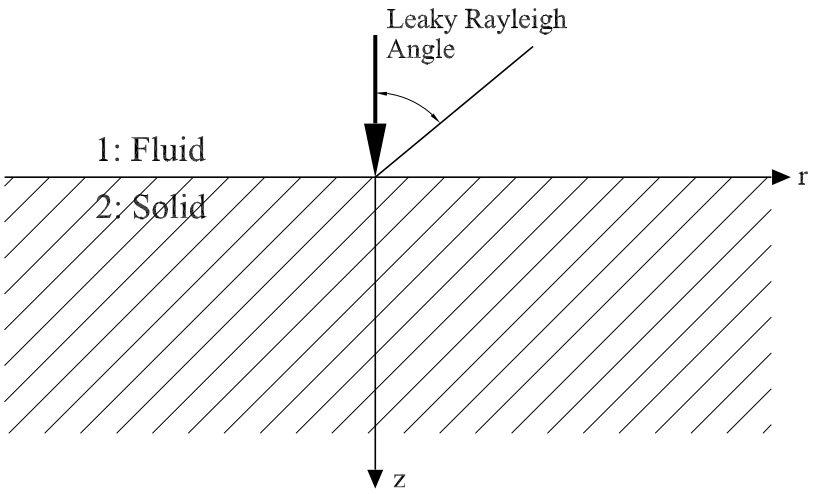

Figure 4.1: Illustration of a transient point load applied at the interface of a fluid-solid half-space system. $z > 0$ in the solid.

time as a step function, is applied at the interface. Impulse responses are then obtained by differentiating the step responses. Therefore for any transient impact loading that has arbitrary temporal variation and spatial distribution, the responses can be obtained by convolving the impulse response in time and space domains. The obtained analytical solutions are verified by EFIT (Elastodynamic Finite Integration Technique) numerical simulation, which is a powerful tool for elastodynamic wave field analysis. Then a simplified analytical formulation for the pressure field in the fluid is derived and illustrated.

4.2 Complete Solution to the Lamb's Problem in Fluid-Solid Halfspace System

Consider a fluid-solid half space system as shown in Fig. 4.1. The solid half space is given by $z > 0$, and the fluid by $z < 0$. The properties of the fluid are given by the Lamé's constant λ_1 and mass density ρ_1, and those of the solid by the Lamé's constants λ_2, μ and density ρ_2. The interface between the fluid and solid half space is subjected to a normal point load of magnitude $QH(t)$, where $H(t)$ is the Heaviside step function. Because the wave motion in the fluid and solid generated by the point load is axially symmetric about the z-axis, cylindrical coordinates are employed, where the origin is located at the load point on the interface.

4.2.1 Wave Equations

Basic Wave Equations

Introducing displacement potential functions φ_1 in the fluid and φ_2 and ψ in the solid, the governing equations for the fluid and the solid half spaces are

$$\begin{aligned} \frac{\partial^2\varphi_1}{\partial r^2}+\frac{1}{r}\frac{\partial\varphi_1}{\partial r}+\frac{\partial^2\varphi_1}{\partial z^2} &= \frac{1}{C_{\mathrm{F}}^2}\ddot{\varphi}_1, \\ \frac{\partial^2\varphi_2}{\partial r^2}+\frac{1}{r}\frac{\partial\varphi_2}{\partial r}+\frac{\partial^2\varphi_2}{\partial z^2} &= \frac{1}{C_{\mathrm{P}}^2}\ddot{\varphi}_2, \\ \frac{\partial^2\psi}{\partial r^2}+\frac{1}{r}\frac{\partial\psi}{\partial r}+\frac{\partial^2\psi}{\partial z^2}-\frac{\psi}{r^2} &= \frac{1}{C_{\mathrm{S}}^2}\ddot{\psi}, \end{aligned} \tag{4.1}$$

where $C_{\mathrm{F}}^2=\lambda_1/\rho_1$ is the acoustic wave velocity in the fluid, and $C_{\mathrm{P}}^2=(\lambda_2+2\mu)/\rho_2$, $C_{\mathrm{S}}^2=\mu/\rho_2$ are the P- and S-wave velocities in the solid. The double dots represent a double derivative with respect to time. The displacements are related to potential functions by

$$\begin{aligned} u_1 &= \frac{\partial\varphi_1}{\partial r}, \\ u_2 &= \frac{\partial\varphi_2}{\partial r}-\frac{\partial\psi}{\partial z}, \\ w_1 &= \frac{\partial\varphi_1}{\partial z}, \\ w_2 &= \frac{\partial\varphi_2}{\partial z}+\frac{1}{r}\frac{\partial(r\psi)}{\partial r}, \end{aligned} \tag{4.2}$$

where the subscript 1 and 2 represent quantities related to the fluid and solid respectively.

Continuity and Initial Condition

A point load is applied at the origin as a Dirac Delta function in space and varies as a Heaviside step function in time, which can be expressed as $QH(t)\dfrac{\delta(r)}{2\pi r}$. Because ideal fluid and shear-free interface conditions are assumed, only the normal stress and vertical component of the displacement are continuous at the interface. The continuity conditions at $z=0$ are

$$\begin{aligned} w_1 &= w_2\ , \\ \tau_{zz2} &= \tau_{zz1}+(-Q)H(t)\frac{\delta(r)}{2\pi r}=-P-QH(t)\frac{\delta(r)}{2\pi r}\ , \\ \tau_{zr2} &= \tau_{zr1}=0, \end{aligned} \tag{4.3}$$

where τ_{zz} and τ_{zr} are the normal and shear components of stress. Assuming the system is at rest prior to , we have

$$\varphi_1(r,z,0)=\ddot{\varphi}_1(r,z,0)=\varphi_2(r,z,0)=\ddot{\varphi}_2(r,z,0)=\psi(r,z,0)=\ddot{\psi}(r,z,0). \tag{4.4}$$

Integral Transform

One-sided Laplace and Hankel transforms are used to obtain solutions to the equations. The Laplace and nth order Hankel transforms are defined respectively as

$$\begin{aligned} \bar{f}(p) &= \int_0^\infty f(t)e^{-pt}dt \ , \\ f^{H_n}(\xi) &= \int_0^\infty f(r)J_n(\xi r)rdr, \end{aligned} \tag{4.5}$$

where p and ξ are variables of the Laplace and Hankel transforms respectively. The corresponding inverse transforms are

$$\begin{aligned} f(t) &= \frac{1}{2\pi i}\int_{\epsilon-i\infty}^{\epsilon+i\infty} \bar{f}(p)e^{pt}dp \ , \\ f(r) &= \int_0^\infty f^{H_n}(\xi)J_n(\xi r)\xi d\xi. \end{aligned} \tag{4.6}$$

Applying the Laplace transform to Eq.(4.1) with respect to time t and the zeroth- and first- order Hankel transform with respect to the radial distance r, the wave equations are transformed to frequency and wavenumber domain. That yields

$$\begin{aligned} &\frac{d^2\overline{\varphi}_1^{H_0}}{dz^2} - \alpha_1^2\bar{\varphi}_1^{H_0} = 0, \\ &\frac{d^2\overline{\varphi}_2^{H_0}}{dz^2} - \alpha_2^2\bar{\varphi}_2^{H_0} = 0, \\ &\frac{d^2\overline{\psi}^{H_1}}{dz^2} - \beta^2\bar{\psi}^{H_1} = 0, \end{aligned} \tag{4.7}$$

where

$$\alpha_1^2 = \xi^2 + s_{\mathrm{F}}^2p^2, \quad \alpha_2^2 = \xi^2 + s_{\mathrm{P}}^2p^2 \ , \quad \beta^2 = \xi^2 + s_{\mathrm{S}}^2p^2, \tag{4.8}$$

and s_{F}, s_{P}, s_{S} are P- and S-wave slowness in the fluid and the solid. Choosing only the terms which lead to finite responses for large values of $|z|$, we obtain the solutions to Eq. (4.7)

$$\begin{aligned} \bar{\varphi}_1^{H_0} &= \Phi_1\left(\xi,p\right)e^{\alpha_1 z}, \\ \bar{\varphi}_2^{H_0} &= \Phi_2\left(\xi,p\right)e^{-\alpha_2 z}, \\ \bar{\psi}^{H_1} &= \Psi\left(\xi,p\right)e^{-\beta z}, \end{aligned} \tag{4.9}$$

where $\Phi_1(\xi,p)$, $\Phi_2(\xi,p)$, $\Psi(\xi,p)$ are functions of p and ξ that need to be determined. From Eq. (4.2) and the displacement-stress relationships, the transformed displacements and stresses (pressure for the fluid) in the fluid are

$$\begin{aligned} \bar{w}_1^{H_0} &= \frac{d\overline{\varphi}_1^{H_0}}{dz}, \\ \bar{u}_1^{H_1} &= -\xi\bar{\varphi}_1^{H_0}, \\ \bar{P}^{H_0} &= -\rho_1 p^2\bar{\varphi}_1^{H_0}, \end{aligned} \tag{4.10}$$

and in the solid are

$$\begin{aligned}
\bar{w}_2^{H_0} &= \frac{d\bar{\varphi}_2^{H_0}}{dz} + \xi\bar{\psi}^{H_1}, \\
\bar{u}_2^{H_1} &= -\frac{d\bar{\psi}^{H_1}}{dz} - \xi\bar{\varphi}_2^{H_0}, \\
\bar{\tau}_{zz2}^{H_0} &= \mu\left[\left(s_{\mathrm{S}}^2 p^2 + 2\xi^2\right)\bar{\varphi}_2^{H_0} + 2\xi\frac{d\bar{\psi}^{H_1}}{dz}\right], \\
\bar{\tau}_{zr2}^{H_1} &= -\mu\left[2\xi\frac{d\bar{\varphi}_2^{H_0}}{dz} + \left(s_{\mathrm{S}}^2 p^2 + 2\xi^2\right)\bar{\psi}^{H_1}\right]
\end{aligned} \tag{4.11}$$

4.2.2 Solutions in Transformed Domain

Applying the same integral transforms to the continuity conditions Eq.(4.3), then substituting Eqs.(4.10) and (4.11) into it generates a group of linear equations in terms of $\Phi_1(\xi,p)$, $\Phi_2(\xi,p)$ and $\Psi(\xi,p)$. Solving the equations yields

$$\begin{aligned}
\Phi_1 &= \frac{Q}{2\pi\mu p}\frac{\alpha_2}{\alpha_1}\frac{s_{\mathrm{S}}^2 p^2}{D_H(\xi,p)}, \\
\Phi_2 &= -\frac{Q}{2\pi\mu p}\frac{s_{\mathrm{S}}^2 p^2 + 2\xi^2}{D_H(\xi,p)}, \\
\Psi &= -\frac{Q}{2\pi\mu p}\frac{2\alpha_2\xi}{D_H(\xi,p)},
\end{aligned} \tag{4.12}$$

where

$$D_H(\xi,p) = (s_{\mathrm{S}}^2 p^2 + 2\xi^2)^2 - 4\xi^2\alpha_2\beta + \frac{\rho_1}{\rho_2}p^4 s_{\mathrm{S}}^4\frac{\alpha_2}{\alpha_1}. \tag{4.13}$$

Substituting Eq.(4.12) into Eqs. (4.10) and (4.11), we obtain the displacements and pressure in the fluid

$$\begin{aligned}
\bar{w}_1^{H_0} &= \frac{Q}{2\pi}\frac{1}{\mu}\frac{\alpha_2 s_{\mathrm{S}}^2 p}{D_H(\xi,p)}e^{\alpha_1 z}, \\
\bar{u}_1^{H_1} &= -\frac{Q}{2\pi}\frac{1}{\mu}\frac{\alpha_2}{\alpha_1}\frac{s_{\mathrm{S}}^2 p\xi}{D_H(\xi,p)}e^{\alpha_1 z}, \\
\bar{P}^{H_0} &= -\frac{Q}{2\pi}\frac{\rho_1}{\rho_2}\frac{\alpha_2}{\alpha_1}\frac{s_{\mathrm{S}}^4 p^3}{D_H(\xi,p)}e^{\alpha_1 z},
\end{aligned} \tag{4.14}$$

and the displacements and stresses in the solid

$$\begin{aligned}
\bar{u}_2^{H_1} &= \frac{Q}{2\pi}\frac{1}{\mu p}\left[\left(s_{\mathrm{S}}^2 p^2 + 2\xi^2\right)e^{-\alpha_2 z} - 2\alpha_2\beta e^{-\beta z}\right]\frac{\xi}{D_H(\xi,p)}, \\
\bar{w}_2^{H_0} &= \frac{Q}{2\pi}\frac{1}{\mu p}\left[\left(s_{\mathrm{S}}^2 p^2 + 2\xi^2\right)e^{-\alpha_2 z} - 2\xi^2 e^{-\beta z}\right]\frac{\alpha_2}{D_H(\xi,p)}, \\
\bar{\tau}_{zz2}^{H_0} &= -\frac{Q}{2\pi}\frac{1}{p}\left[\left(s_{\mathrm{S}}^2 p^2 + 2\xi^2\right)^2 e^{-\alpha_2 z} - 4\alpha_2\beta\xi^2 e^{-\beta z}\right]\frac{1}{D_H(\xi,p)}, \\
\bar{\tau}_{zr2}^{H_1} &= \frac{Q}{2\pi}\frac{1}{p}\left[-e^{-\alpha_2 z} + e^{-\beta z}\right]\frac{2\alpha_2\xi\left(s_{\mathrm{S}}^2 p^2 + 2\xi^2\right)}{D_H(\xi,p)}.
\end{aligned} \tag{4.15}$$

4.2.3 Characteristic Equation for Leaky Rayleigh and Scholte Waves

$D_H(\xi, p) = 0$ is the characteristic equation for leaky Rayleigh waves at the interface of fluid-solid half spaces. Introducing the substitution $\gamma = i\xi/ps_{\mathrm{S}}$ and notations $q = s_{\mathrm{P}}/s_{\mathrm{S}}$ and $u = s_{\mathrm{F}}/s_{\mathrm{S}}$, the equation $D_H = 0$ can be changed to the following in terms of γ

$$(1-2\gamma^2)^2 - 4\gamma^2\sqrt{\gamma^2-1}\sqrt{\gamma^2-q^2} + \frac{\rho_1}{\rho_2}\frac{\sqrt{\gamma^2-q^2}}{\sqrt{\gamma^2-u^2}} = 0. \tag{4.16}$$

Eq.(4.16) is the same as that given by Viktorov [68], which differs from the regular Rayleigh equation in the third term due to the pressure of the fluid. Equation (4.16) produces eight Riemann sheets owing to the square roots. The roots have the physical meaning of normalized slowness with respect to s_{S}. When leaky Rayleigh waves exist, we can obtain 6 roots, which include 2 pairs of complex conjugate pairs corresponding to the leaky Rayleigh wave $[\mathrm{Re}(\gamma_R^2) < u^2]$, and 2 opposite real roots corresponding to the Scholte wave $(\gamma_{\mathrm{sch}}^2 > u^2)$.

The two pairs of complex conjugate roots corresponding to the leaky Rayleigh wave take the form of $\pm[\mathrm{Re}(\gamma) \pm i\,\mathrm{Im}(\gamma)]$, in which only two roots are acceptable. Because p is the Laplace transform variable, $\mathrm{Re}(p)$ must be negative to have a finite time domain response. Therefore, only the roots which lead to $\mathrm{Re}(p) < 0$ are acceptable, where $p = i\xi/\gamma s_{\mathrm{S}}$. A quick analysis shows that the two acceptable roots take the form of $\gamma_{\mathrm{R1,R2}} = \pm\mathrm{Re}(\gamma) - i\mathrm{Im}(\gamma)$. Here, we denote them as γ_{R1}, γ_{R2}, and note $\gamma_{\mathrm{R2}} = -\bar{\gamma}_{\mathrm{R1}}$, where the top bar indicates complex conjugate.

Analysis also shows that $|\mathrm{Re}(\gamma_{R1,R2})| < s_{\mathrm{R}}/s_{\mathrm{S}}$, where s_{R} is the slowness of Rayleigh wave in free surface solid half space. This result confirms that the slowness of the leaky Rayleigh wave is smaller than s_{R}, i.e., in a fluid-solid half space system, the leaky Rayleigh wave will travel faster than the regular Rayleigh wave in the same free surface solid. This conclusion is reasonable considering the influence of fluid pressure applied on solid surface. The imaginary part of γ_R accounts for the energy leaked into fluid. The larger the value of $|\,\mathrm{Im}(\gamma_R)|$, the more energy leaks into the fluid.

The Scholte wave velocity can be obtained from the real roots $\pm\gamma_{sch}$, where $\gamma_{sch} > u$ and $s_{sch} = \gamma_{sch}s_{\mathrm{S}}$. Scholte waves always exist for any fluid solid combination case. For lighter fluids lying on stiffer solids case, s_{sch} is only slightly smaller than the acoustic wave velocity of the fluid, and the Scholte wave contribution is relatively small. The property of Scholte waves will be discussed in more detail in section 4.4.4 .

4.2.4 Time-space Domain Solutions in the Fluid

The solution of fluid pressure in space-time domain is derived because pressure in the fluid is the most often measured quantity in practical application. By taking the inverse zeroth order Hankel transform to Eq. (4.14) and introducing the substitution$\xi = p\eta$, we have

$$\bar{P} = -\frac{Qs_{\mathrm{S}}^4}{2\pi}\frac{\rho_1}{\rho_2}\int_0^\infty \frac{\sqrt{\eta^2+s_{\mathrm{P}}^2}}{\sqrt{\eta^2+s_{\mathrm{F}}^2}}\frac{p}{D(\eta)}e^{pz\sqrt{\eta^2+s_{\mathrm{F}}^2}}J_0(p\eta r)\eta d\eta, \tag{4.17}$$

where $D(\eta)$ is defined as

$$D(\eta) = (2\eta^2+s_{\mathrm{S}}^2)^2 - 4\eta^2\sqrt{\eta^2+s_{\mathrm{P}}^2}\sqrt{\eta^2+s_{_S}^2} + \frac{\rho_1}{\rho_2}\frac{\sqrt{\eta^2+s_{\mathrm{P}}^2}}{\sqrt{\eta^2+s_{_F}^2}}s_{\mathrm{S}}^4. \tag{4.18}$$

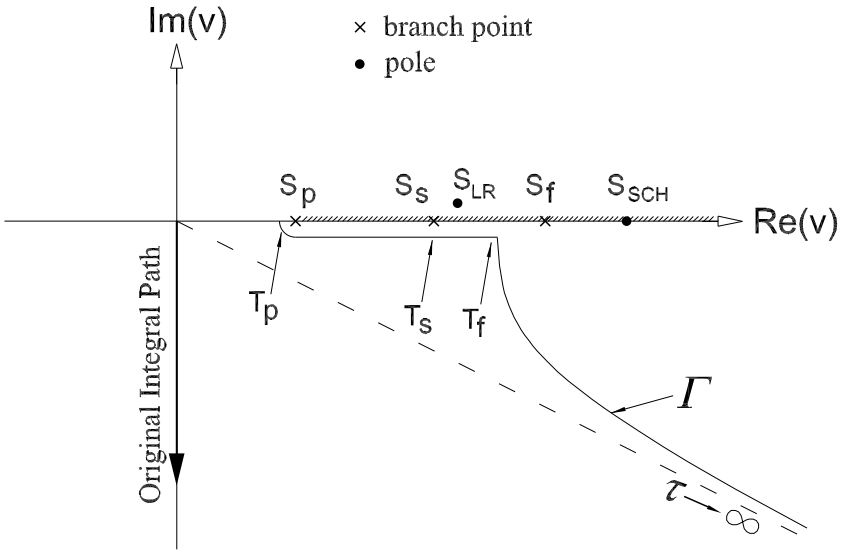

Figure 4.2: Complex v plane and the modified integral path. The indices denote: P $\rightarrow$ leaky P wave, S $\rightarrow$ leaky S wave, LR $\rightarrow$ leaky R wave, f$\rightarrow$ fluid acoustic wave, SCH $\rightarrow$ Scholte wave.

The inverse Laplace transform is evaluated by the Cagniard-de Hoop method, as described by Achenbach [1]. Introducing the following representation of $J_0(x)$

$$J_0(x) = \frac{2}{\pi}\mathrm{Im}\int_1^\infty \frac{e^{ixs}}{\sqrt{s^2-1}}ds \tag{4.19}$$

and substituting it into Eq. (4.17) yields

$$\bar{P} = -\frac{Qs_{\mathrm{S}}^4}{\pi^2}\frac{\rho_1}{\rho_2}\mathrm{Im}\int_0^\infty \frac{\sqrt{\eta^2+s_{\mathrm{P}}^2}}{\sqrt{\eta^2+s_{\mathrm{F}}^2}}\frac{\eta}{D(\eta)}d\eta\int_1^\infty p\frac{e^{ip\eta rs+pz\sqrt{\eta^2+s_{\mathrm{F}}^2}}}{\sqrt{s^2-1}}ds. \tag{4.20}$$

Introducing the substitution $t = -i\eta rs - z\sqrt{\eta^2+s_{\mathrm{F}}^2}$ and $\eta = iv$ yields

$$\bar{P} = \frac{Qs_{\mathrm{S}}^4}{\pi^2}\frac{\rho_1}{\rho_2}\mathrm{Im}\int_0^{-i\infty} \frac{\sqrt{s_{\mathrm{P}}^2-v^2}}{\sqrt{s_{\mathrm{F}}^2-v^2}}\frac{v}{D(iv)}dv\int_1^\infty p\frac{e^{-pt}}{\sqrt{s^2-1}}ds, \tag{4.21}$$

where

$$L^{-1}\left(\int_1^\infty p\frac{e^{-pt}}{\sqrt{s^2-1}}ds\right) = \frac{d}{dt}\left(\frac{H(t+z\sqrt{s_{\mathrm{F}}^2-v^2}-vr)}{\sqrt{\left(t+z\sqrt{s_{\mathrm{F}}^2-v^2}\right)^2-v^2r^2}}\right), \tag{4.22}$$

and L represents the Laplace transform. Therefore, the inverse Laplace transform of Eq. (4.21) is

$$\begin{aligned} P(t) &= \frac{Qs_{\mathrm{S}}^4}{\pi^2}\frac{\rho_1}{\rho_2}\frac{d}{dt}\left(\mathrm{Im}\int_0^{-i\infty}\frac{\sqrt{s_{\mathrm{P}}^2-v^2}}{\sqrt{s_{\mathrm{F}}^2-v^2}}\frac{v}{D(iv)}\frac{H(t+z\sqrt{s_{\mathrm{F}}^2-v^2}-vr)}{\sqrt{\left(t+z\sqrt{s_{\mathrm{F}}^2-v^2}\right)^2-v^2r^2}}dv\right) \\ &= \frac{Qs_{\mathrm{S}}^4}{\pi^2}\frac{\rho_1}{\rho_2}\frac{d}{dt}G^P(t), \end{aligned} \tag{4.23}$$

where $G^P(t)$ is defined as the Green's function for pressure. The variable v is related to γ in Eq. (4.16) by $v = -\gamma s_{\mathrm{S}}$. According to the analysis in the previous section, there are two poles in the right half complex v plane, which correspond to leaky Rayleigh and Scholte wave arrivals. The integral path along the negative imaginary axis can be deformed to path Γ as shown in Fig. 4.2 The new integration path Γ is defined by the equation $\tau = vr - z\sqrt{s_{\mathrm{F}}^2-v^2}$, which can be solved for v to yield

$$v(\tau) = \frac{\tau\, r + z\sqrt{s_{\mathrm{F}}^2R^2-\tau^2}}{R^2}, \quad \tau \,\text{is real and}\, 0 \le \tau \le \infty, \tag{4.24}$$

where $R = \sqrt{r^2+z^2}$. The benefit of deforming the original integration path to Γ is obvious, because there is no pole along the new path. The Green's function integration along the new path is

$$G^P(t) = \mathrm{Im}\int_{t_p}^{t}\frac{\sqrt{s_{\mathrm{P}}^2-v(\tau)^2}}{\sqrt{s_{\mathrm{F}}^2-v(\tau)^2}}\frac{v(\tau)}{D\left[iv(\tau)\right]}\frac{r-\tau z\Big/\sqrt{s_{\mathrm{F}}^2R^2-\tau^2}}{R^2\sqrt{\left[t-\tau+v(\tau)r\right]^2-v(\tau)^2r^2}}d\tau, \tag{4.25}$$

where $t_p = r\, s_{\mathrm{P}} + |z|\sqrt{s_{\mathrm{F}}^2-s_{\mathrm{P}}^2}$ is the leaky P wave arrival time. $G^P(t) = 0$ when $t < t_{\mathrm{P}}$.

However, when the receiver is located on the interface, i.e., $z = 0$, the integral path Γ is along the real axis, and passes by the Scholte pole. In this case, the principal value of Eq. (4.25) must be taken.

The integrand in Eq. (4.25) has a square root singularity at end point $\tau = t$, which increases the difficulty of numerical integration. This problem can be solved by further introducing the following transformation,

$$\tau = t_1\cos^2(\theta) + t_2\sin^2(\theta), \tag{4.26}$$

where t_1, t_2 are the lower and upper limits of the integration. Then the integration interval $t_1 \le \tau \le t_2$ is mapped to the fixed interval $0 \le \theta \le \pi/2$, while

$$\begin{aligned} d\tau &= 2(t_2-t_1)\sin(\theta)\cos(\theta), \\ \sqrt{\left[t_2\tau+v(\tau)r\right]^2-v(\tau)^2r^2} &= \sqrt{(t_2-t_1)}\cos(\theta)\sqrt{(t_2-t_1)\cos^2(\theta)+2v(\tau)r} \end{aligned} \tag{4.27}$$

Another square root singularity at point $\tau = t_f = s_{\mathrm{F}}R$ can be processed similarly. A similar technique was also used by de Hoop [21].

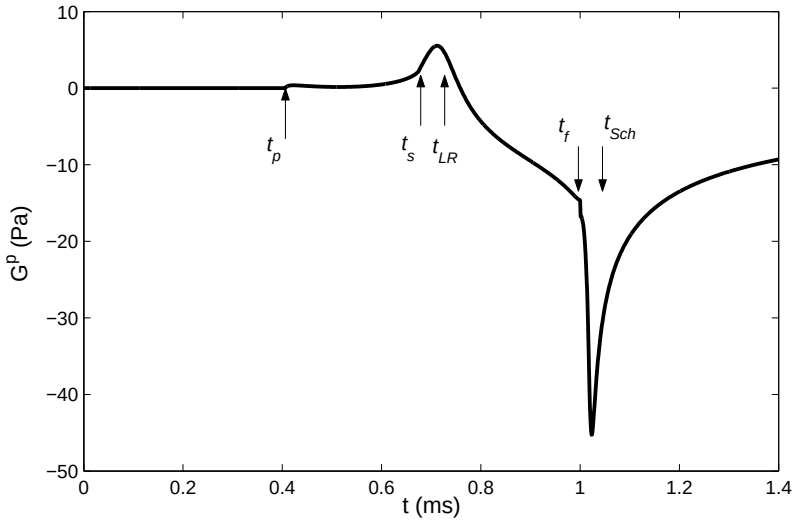

Figure 4.3: Green's function $G^p(t)$ for pressure in the fluid. The receiver is at $r = 1.5m$, $z = 0.05m$. Material parameters for the fluid $\rho_1 = 1000kg/m^3$, $c_F = 1500m/s$, and for the solid $\rho_2 = 2400kg/m^3$, $C_\mathrm{P} = 4000m/s$, $\nu = 0.25$.

The vertical component of displacement in the fluid is also obtained in the same way

$$w(t) = -\frac{Q}{\pi^2}\frac{s_\mathrm{S}^4}{\rho_2}\mathrm{Im}\int_{t_p}^{t}\frac{\sqrt{s_\mathrm{P}^2 - v(\tau)^2}\,v(\tau)}{D\left[iv(\tau)\right]\;R^2}\frac{r - \tau z\Big/\sqrt{s_\mathrm{F}^2R^2 - \tau^2}}{\sqrt{\left[t-\tau+v(\tau)r\right]^2 - v(\tau)^2r^2}}d\tau. \tag{4.28}$$

Figure 4.3 shows the Green's function $G^p(t)$ at a near-surface position $= 1.5m, z = -0.05m$ the fluid. The material configuration simulates a concrete/water system. The arrival times of all wave types are marked. It is noticed that the slope is discontinuous at positions $t = t_p$, t_s and t_f, which correspond to the leaky P-, leaky S- and fluid acoustic waves in water. From the mathematics viewpoint, these discontinuities come from the branch points along the integral path Γ. The poles corresponding to the leaky Rayleigh and Scholte wave arrivals contribute to the large smooth peaks. When the receiving position is very close to the interface, the integral path Γ in Fig. 4.2 will bend to the real axis, and a sharp peak will appear nearby the Scholte wave arrival in Fig. 4.3. The impulse response to a point loading on the interface between a fluid and a solid half space can be obtained from the corresponding step response solution by taking differentiation with respect to time. Then for any transient loading that has arbitrary temporal variation and spatial distribution, the response can be obtained by convolving the impulse response in both time and space domains.

4.2.5 Time-space Domain Solutions in the Solid

Comparing Equation (4.15) to the solution of Lamb's problem for a free surface solid half space [1], we notice that they have the same expression, except for the difference in the definition of $D_H(\xi, p)$. The third term of D_H disappears for the free surface solid half space case. Therefore, the time-domain solution to Equation (4.15) can be obtained by means of Cagniard-de Hoop scheme, as given by Achenbach [1].

We Introduce $\theta = \arctan(z/r)$ and $\theta_{cr} = \arccos(s_{\mathrm{P}}/s_{\mathrm{S}})$, where (r, z) is the receiver's position in the solid. t_{P}, t_{S} and t_H are defined as the arrival times of P-, S- and head waves

$$\begin{aligned} t_{\mathrm{P}} &= s_{\mathrm{P}} R, \\ t_{\mathrm{S}} &= s_{\mathrm{S}} R, \\ t_H &= s_{\mathrm{P}} R\cos(\theta) + \sqrt{s_{\mathrm{S}}^2 - s_{\mathrm{P}}^2} R\sin(\theta). \end{aligned} \tag{4.29}$$

Same as in the pure solid half space, head waves are generated when $\theta < \theta_{cr}$. Therefore the solution is discussed for the following two conditions: $\theta \geq \theta_{cr}$ and $\theta < \theta_{cr}$.

For $\theta \geq \theta_{cr}$, the solution of w is

$$w = -\frac{Q}{\mu\pi^2}\mathrm{Im}\begin{cases} 0 & \text{if } t < t_{\mathrm{P}}, \\ I_1|_{t_{\mathrm{P}}}^{t}, & \text{if } t_{\mathrm{P}} \leq t < t_{\mathrm{S}}. \\ I_1|_{t_{\mathrm{P}}}^{t} + I_2|_{t_{\mathrm{S}}}^{t}, & \text{if } t_{\mathrm{S}} \leq t. \end{cases} \tag{4.30}$$

For $\theta < \theta_{cr}$,

$$w = -\frac{Q}{\mu\pi^2}\mathrm{Im}\begin{cases} 0 & \text{if } t < t_{\mathrm{P}}, \\ I_1|_{t_{\mathrm{P}}}^{t}, & \text{if } t_{\mathrm{P}} \leq t < t_H. \\ I_1|_{t_{\mathrm{P}}}^{t} + I_2|_{t_H}^{t}, & \text{if } t_H \leq t < t_{\mathrm{S}}. \\ I_1|_{t_{\mathrm{P}}}^{t} + I_2|_{t_H}^{t_{\mathrm{S}}} + I_2|_{t_{\mathrm{S}}}^{t}, & \text{if } t_{\mathrm{S}} \leq t, \end{cases} \tag{4.31}$$

where I_1 and I_2 are contributions from P waves and S waves. I_1 and I_2 are defined as

$$I_1|_{t_1}^{t_2} = \int_{t_1}^{t_2} \frac{\sqrt{s_{\mathrm{S}}^2 - 2v(\tau)^2}\sqrt{s_{\mathrm{P}}^2 - v(\tau)^2}v(\tau)}{D\left[iv(\tau)\right]} \frac{r - \dfrac{i\tau z}{\sqrt{(\tau)^2 - s_{\mathrm{P}}^2 R^2}}}{\sqrt{\left[t - \tau + v(\tau)r\right]^2 - v(\tau)^2 r^2}}\, d\tau, \tag{4.32}$$

$$I_2|_{t_1}^{t_2} = \int_{t_1}^{t_2} \frac{2v(\tau)^2\sqrt{s_{\mathrm{P}}^2 - v(\tau)^2}v(\tau)}{D\left[iv(\tau)\right]} \frac{r + \dfrac{\tau z}{\sqrt{s_{\mathrm{S}}^2 R^2 - (\tau)^2}}}{\sqrt{\left[t - \tau + v(\tau)r\right]^2 - v(\tau)^2 r^2}}\, d\tau. \tag{4.33}$$

Figure 4.4 shows the Green's function of displacement w in the solid at position (1.5m,0.1m) for water/concrete configuration. The response at the same position for a free surface solid half space is also displayed. Arrival times of all waves are marked. It is seen that the two responses have the same arrival times of P-, S- and head waves. For the solid with fluid overlay, the Rayleigh wave response is less intensive than that in a free surface half space owning to energy leakage into the fluid. Scholte waves penetrate into the solid, and the penetration depth depends on wave frequency and the relative properties between the solid and fluid. Figure 4.5 displays the Scholte wave decay pattern in the solid and fluid for the water/concrete material configuration. u and w are normalized with respect to the vertical displacement w_0 at $z = 0$. In Fig. 4.5, u and w decay much faster in the solid than in the fluid. The amplitude of w decreases to only 20% of the surface response at the half

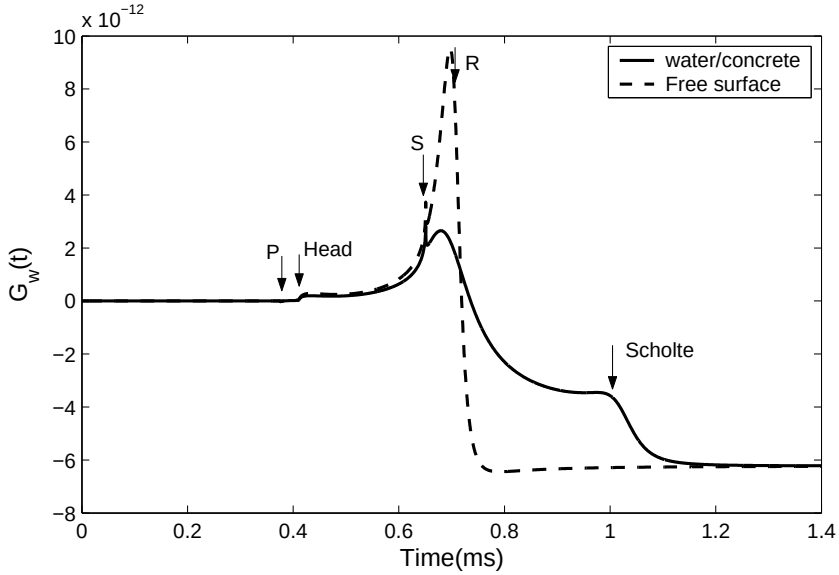

Figure 4.4: Green's function of the vertical displacement w in the solid. The receiving position is at r=1.5m, z=0.1m in the solid. Material parameters are selected to simulate water/concrete configuration as shown in Fig. 4.3.

wavelength depth in the solid.

4.3 Numerical Simulation

To verify the obtained solutions, numerical analyses were performed to simulate the response for fluid-solid half space cases. The elastodynamic finite integration technique (EFIT)[1]. is a numerical time-domain scheme to model elastic wave propagation in homogeneous and heterogeneous, dissipative and non-dissipative, as well as isotropic and anisotropic elastic media [24]. EFIT uses a velocity-stress formalism on a staggered spatial and temporal grid complex. The starting point of EFIT is the integral form of the linear governing equations, i.e. the Cauchy equation of motion, and the equation of deformation rate. EFIT performs integrations over certain control volumes V, and the surfaces of these cells S, assuming constant velocity and stress within V and on each S. This method requires staggered grids and leads to a very stable and efficient numerical code, which also allows easy and flexible treatment of various boundary conditions. In recent years, EFIT has been successfully used for a wide variety of applications, especially in the field of nondestructive testing In recent years, EFIT has been successfully used for a wide variety of applications, especially in the field of nondestructive testing [63].

In the present case of a transient point load at a fluid-solid interface, we used a special axisymmetric EFIT code in cylindrical coordinates [63]. The water/concrete case shown in Fig. 4.3 was studied. The material parameters are: for water $\rho_1 = 1000kg/m^3$, $c_F = 1500m/s$; and for concrete $\rho_2 = 2400kg/m^3$, $C_\mathrm{P} = 1500m/s$, and Poisson's ratio $\nu = 0.25$. The vertical transient point load varies with time as function $f(t) = \sin^2(\pi t/T)$, where the force duration is $T = 200\mu s$. A grid spacing of $\Delta r = \Delta z = 2.5$mm and a time step of $0.44\mu s$ is used in order to guarantee stability as

[1]EFIT analysis was performed by Frank Schubert, Lab EADQ, Fraunhofer Institute for Nondestructive Testing, Germany

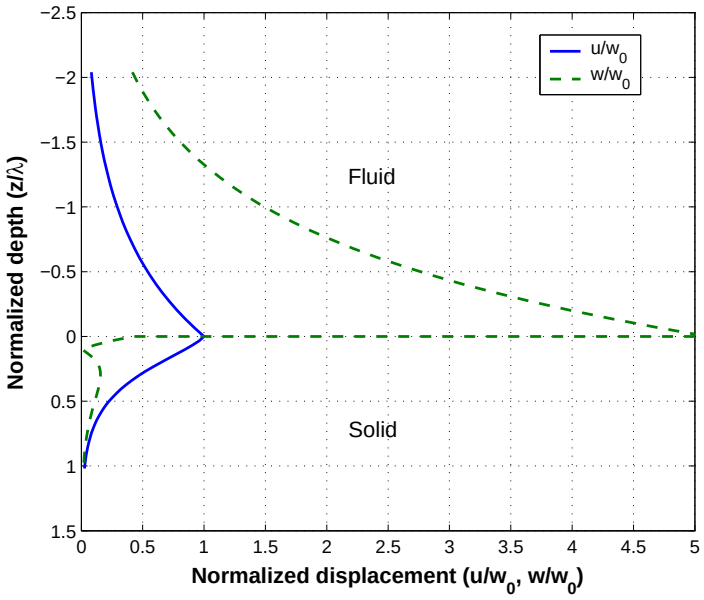

Figure 4.5: Scholte wave decay in the solid and fluid.

well as sufficient discretization of the shortest wavelengths. The dimensions of the model are 2 m in radial and 3 m in axial direction, resulting in 800 $\times$ 1200 grid cells. At the outer boundaries of the model, highly effective absorbing boundary conditions based on the perfectly matched layer (PML) are used in order to suppress interfering reflections[36].

Figure 4.6 shows the cross-sectional snapshot image of pressure field (absolute value) as generated by EFIT, at time $t = 720\mu s$. Only the region with $r > 0$ was calculated, but for better illustration the reversed region with $r < 0$ is also shown here. The half circle in the upper half plane represents the acoustic wave front in water, and the inclined lines represent the leaky Rayleigh wave fronts, which are tangent to the half circle at the leaky angle direction. In this case, the leaky Rayleigh angle determined by Snell's Law is $\theta = 43.8°$, measured from the vertical axis. The Leaky Rayleigh wave front is separable from the subsequent Scholte and fluid acoustic wave fronts at larger values of radial distance r. The 3-D shape of the combined leaky Rayleigh and fluid acoustic wave fronts look like a domed cone. The leaky Rayleigh wave in concrete is also seen, which behaves similar to the ordinary Rayleigh wave, and attenuates exponentially with increasing depth in the solid. In the near-interface region, the Scholte wave effect is strong in both the fluid and the solid.

Figure 4.7 shows the comparison between the analytical solution and EFIT simulation result of pressure at position of $r = 1.5m, z = -0.05m$, with the arrival times of all types of waves denoted. Very good agreement between the analytical and numerical responses is observed.

4.4 Simplified Solution to the Lamb's Problem

In section 4.2, the complete analytical solution of pressure and displacement in the fluid are obtained. However, the integral form solution is not always convenient to use. In this section, the author derive a simplified closed-form solution to the same problem by considering only Rayleigh and Scholte

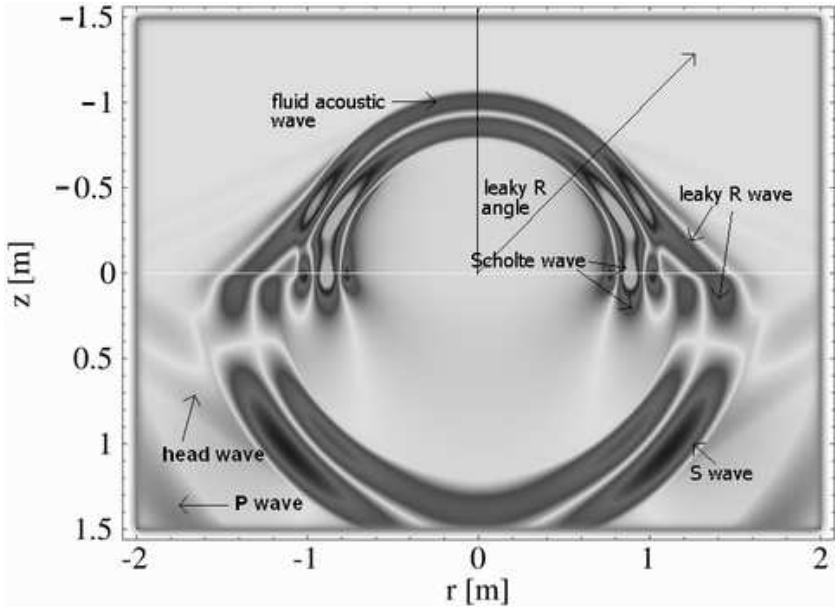

Figure 4.6: Snapshot of absolute values of pressure (in fluid) and stress τ_{zz} (in solid) field by EFIT analysis. The snapshot is taken at $t = 720\mu s$. The interface is subject to a transient point load that varies with time as $f(t) = sin^2(\pi t/T)$ with $T = 200$ μs.

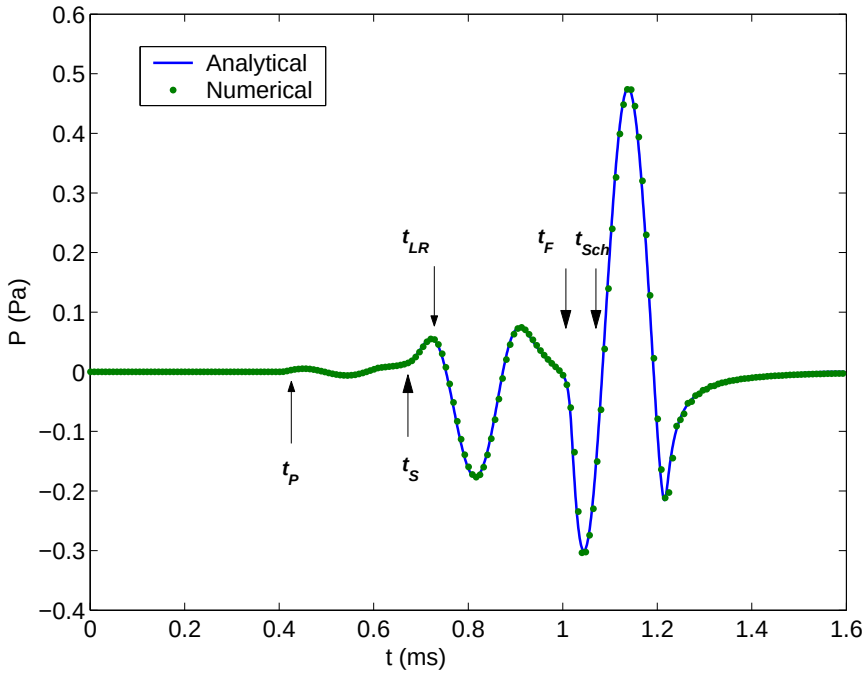

Figure 4.7: Comparison of analytical and numerical(EFIT) solutions. Pressure in the fluid is measured at r=1.5m, z=-0.05m. The interface is subject to a point load that varies with time as $f(t) = sin^2(\pi t/T)$ with T=200μs. Material parameters for the fluid $\rho_1 = 1000kg/m^3$, $C_{\text{F}} = 1500m/s$; for the solid $\rho_2 = 2400kg/m^3$, $C_{\text{P}} = 4000m/s$, $\nu = 0.25$.

pole contributions. This simplification is acceptable when measurements are taken at a large distance from the source. According to the previous analysis, the wave field excited by a normal point load at the interface includes contributions from leaky P, S, Rayleigh waves, fluid acoustic waves, and Scholte waves. Analysis shows that, at large horizontal distances from the source, disturbances near the interface are dominated by leaky Rayleigh and Scholte wave contributions, which can be obtained from the residues at corresponding poles. The similar idea was already used to investigate Rayleigh wave effects in a free surface half space by Chao [15]. Achenbach [1] reproduced Chao's results in detail. The simplified solution provides an easy and quick way to estimate leaky Rayleigh and Scholte wave effects.

4.4.1 Displacement and Stress in the Fluid

Applying the inverse Hankel and Laplace transforms to the transformed solution in Eq. (4.14), the pressure in fluid can be expressed as

$$P(r,z,t) = -\frac{Q}{2\pi}\frac{s_{\mathrm{S}}^4}{2\pi i}\frac{\rho_1}{\rho_2}\int_0^\infty J_0(\xi r)\xi \int_{\varepsilon-i\infty}^{\varepsilon+i\infty}\frac{\alpha_2}{\alpha_1}\frac{p^3}{D_H(\xi,p)}e^{\alpha_1 z+pt}dpd\xi. \tag{4.34}$$

Considering the integrand term, the contributions from the leaky Rayleigh poles are

$$\begin{aligned} I_1 &= \frac{1}{2\pi i}\int_0^\infty J_0(\xi r)\xi \int_{\varepsilon-i\infty}^{\varepsilon+i\infty}\frac{\alpha_2}{\alpha_1}\frac{p^3}{D_H(\xi,p)}e^{\alpha_1 z+pt}dpd\xi \\ &= \int_0^\infty J_0(\xi r)\xi\left[\frac{\alpha_2}{\alpha_1}\frac{p^3}{\partial D_H(\xi,p)/\partial p}e^{\alpha_1 z+pt}\right]_{p=i\xi/s_{\mathrm{S}}\,\gamma_{R1,2}} d\xi, \end{aligned} \tag{4.35}$$

where the expression

$$\left[\frac{\alpha_2}{\alpha_1}\frac{p^3}{\partial D_H(\xi,p)/\partial p}\right]_{p=i\xi/s_{\mathrm{S}}\,\gamma_{R1,2}}$$

represents a pair of complex conjugate constants, denoted as A_1 and $\bar{A}_1$.

Introducing

$$m_{1,2} = -\frac{i}{\gamma_{R1,R2}}\left[\frac{z}{r}\sqrt{u^2-\gamma_{R1,R2}^2}+\frac{t}{s_{\mathrm{S}}r}\right] \tag{4.36}$$

generates

$$[\alpha_1 z+pt]_{p=i\xi/s_{\mathrm{S}}\gamma_{R1,2}} = -\xi r m_{1,2}, \tag{4.37}$$

where $m_1 = \bar{m}_2$. Thus, Eq. (4.35) can be expressed as

$$\begin{aligned} I_1 &= A_1\int_0^\infty J_0(\xi r)\xi e^{-\xi m_1 r}d\xi + \bar{A}_1\int_0^\infty J_0(\xi r)\xi e^{-\xi m_2 r}d\xi \\ &= 2\mathrm{Re}\int_0^\infty A_1 e^{-\xi m_1 r}J_0(\xi r)\xi d\xi \\ &= \frac{2}{r^2}\mathrm{Re}\left[\frac{A_1 m_1}{(1+m_1^2)^{3/2}}\right], \quad \mathrm{Re}(m_1)>0, \end{aligned} \tag{4.38}$$

where we use the zeroth order Hankel transform formula

$$\int_0^\infty J_0(\xi r)\xi e^{-a\xi}d\xi = \frac{a}{(r^2+a^2)^{3/2}}, \quad \mathrm{Re}(a) > 0. \tag{4.39}$$

From Eq. (4.34), the pressure P is expressed as

$$P = -\frac{Q}{\pi}\frac{\rho_1}{\rho_2}\frac{1}{r^2}s_{\mathrm{S}}^4 \mathrm{Re}\left[\frac{A_1 m_1}{(1+m_1^2)^{3/2}}\right] \tag{4.40}$$

Similarly, by introducing

$$\begin{aligned} A_2 &= \xi\left[\frac{\alpha_2 p}{\partial D_H(\xi,p)/\partial p}\right]_{p=\frac{i\xi}{s_{\mathrm{S}}\gamma_{R1}}}, \\ A_3 &= \left[\frac{\alpha_2}{\alpha_1}\frac{p\xi^2}{\partial D_H(\xi,p)/\partial p}\right]_{p=\frac{i\xi}{s_{\mathrm{S}}\gamma_{R1}}}, \end{aligned} \tag{4.41}$$

the vertical and radial components of the displacement in the fluid are obtained

$$\begin{aligned} w_1 &= \frac{Q}{\pi}\frac{s_{\mathrm{S}}^4}{\rho_2}\frac{1}{r}\mathrm{Re}\left[\frac{A_2}{(1+m_1^2)^{1/2}}\right], \\ u_1 &= -\frac{Q}{\pi}\frac{s_{\mathrm{S}}^2}{\mu}\frac{1}{r}\mathrm{Re}\left(\left[1-\frac{m_1}{(1+m_1^2)^{1/2}}\right]A_3\right), \quad \mathrm{Re}(m_1) > 0. \end{aligned} \tag{4.42}$$

Care should be taken with the square root when calculating $m_{1,2}$ from Eq. (4.36). To have bounded results, only the branch that gives $\mathrm{Re}(m_1) > 0$ should be selected.

4.4.2 Displacement and Stress in the Solid Half Space

The response of the leaky Rayleigh wave in the solid can be obtained in a similar way. Introducing

$$\begin{aligned} n_{p1,2} &= \frac{1}{\gamma_{R1,R2}}\left[\pm\frac{z}{r}\sqrt{\gamma_{R1,R2}^2 - q^2} - i\tau\right], \\ n_{s1,2} &= \frac{1}{\gamma_{R1,R2}}\left[\pm\frac{z}{r}\sqrt{\gamma_{R1,R2}^2 - 1} - i\tau\right] \end{aligned} \tag{4.43}$$

yields

$$\begin{aligned} [-\alpha_2 z + pt]_{p=i\xi/s_{\mathrm{S}}\gamma_{R1,R2}} &= -\xi\frac{r}{\gamma_{R1,R2}}\left[\pm\sqrt{\gamma_{R1,R2}^2 - q^2}\frac{z}{r} - i\tau\right] = -\xi r n_{p1,2}, \\ [-\beta z + pt]_{p=i\xi/s_{\mathrm{S}}\gamma_{R1,R2}} &= -\xi\frac{r}{\gamma_{R1,R2}}\left[\pm\sqrt{\gamma_{R1,R2}^2 - 1}\frac{z}{r} - i\tau\right] = -\xi r n_{s1,2}. \end{aligned} \tag{4.44}$$

The real part of Eq. (4.44) must be negative to have bounded responses, therefore the real parts of n_{p1}, n_{p2}, n_{s1}, n_{s2} must by positive. Using the similar argument for dealing with $m_{1,2}$, only those results of n_{p1}, n_{p2}, n_{s1}, n_{s2} that have positive real parts are acceptable. In addition, n_{p1}, n_{p2} and n_{s1}, n_{s2} should be complex conjugate pairs.

Applying the inverse Hankel and Laplace transforms to Eq. (4.15) and calculating the residues at Rayleigh poles yields the displacements and stresses in the solid

$$
\begin{aligned}
w_2 &= \frac{Q}{\pi}\frac{s_{\mathrm{S}}^2}{\rho_2}\frac{1}{r}\mathrm{Re}\left[\frac{B_1}{\sqrt{1+n_{p1}^2}}-\frac{B_2}{\sqrt{1+n_{s1}^2}}\right], \\
u_2 &= \frac{Q}{\pi}\frac{s_{\mathrm{S}}^2}{\rho_2}\frac{1}{r}\mathrm{Re}\left[B_3\left(1-\frac{n_{p1}}{\sqrt{1+n_{p1}^2}}\right)-B_4\left(1-\frac{n_{s1}}{\sqrt{1+n_{s1}^2}}\right)\right], \qquad (4.45) \\
\tau_{zz2} &= -\frac{Q}{\pi}\frac{1}{r^2}\mathrm{Re}\left[\frac{B_5 n_{p1}}{\left(1+n_{p1}^2\right)^{3/2}}-\frac{B_6 n_{s1}}{\left(1+n_{s1}^2\right)^{3/2}}\right], \\
\tau_{zr2} &= \frac{Q}{\pi}\frac{1}{r^2}\mathrm{Re}\left[\frac{-B_7}{\left(1+n_{p1}^2\right)^{3/2}}+\frac{B_7}{\left(1+n_{s1}^2\right)^{3/2}}\right], \qquad (4.46)
\end{aligned}
$$

where the coefficients are

$$
\begin{aligned}
B_1 &= \left[\frac{s_{\mathrm{S}}^2 p^2+2\xi^2}{p\partial D_H(\xi,p)/\partial p}\alpha_2\xi\right]_{p=\frac{i\xi}{s_{\mathrm{S}}\gamma_{R1}}}, \\
B_2 &= \left[\frac{2\xi^3\alpha_2}{p\partial D_H(\xi,p)/\partial p}\right]_{p=\frac{i\xi}{s_{\mathrm{S}}\gamma_{R1}}}, \\
B_3 &= \left[\frac{\left(s_{\mathrm{S}}^2 p^2+2\xi^2\right)}{p\partial D_H(\xi,p)/\partial p}\xi^2\right]_{p=\frac{i\xi}{s_{\mathrm{S}}\gamma_{R1}}}, \qquad (4.47) \\
B_4 &= \left[\frac{2\xi^2\alpha_2\beta}{p\partial D_H(\xi,p)/\partial p}\right]_{p=\frac{i\xi}{s_{\mathrm{S}}\gamma_{R1}}}, \\
B_5 &= \left[\frac{\left(s_{\mathrm{S}}^2 p^2+2\xi^2\right)^2}{p\partial D_H(\xi,p)/\partial p}\right]_{p=\frac{i\xi}{s_{\mathrm{S}}\gamma_{R1}}}, \\
B_6 &= 2B_4, \\
B_7 &= 2B_1.
\end{aligned}
$$

The expressions in Eq. (4.45) are only valid in the region where $\mathrm{Re}(n_{p1,p2})>0$ and $\mathrm{Re}(n_{s1,s2})>0$. Other stress components in the solid can be derived from the following stress-displacement relations

$$
\begin{aligned}
\tau_{rr2} &= (\lambda_2+2\mu)\frac{\partial u_2}{\partial r}+\lambda_2\left(\frac{u_2}{r}+\frac{\partial w_2}{\partial z}\right), \\
\tau_{\theta\theta 2} &= (\lambda_2+2\mu)\frac{u_2}{r}+\lambda_2\left(\frac{\partial u_2}{\partial r}+\frac{\partial w_2}{\partial z}\right). \qquad (4.48)
\end{aligned}
$$

4.4.3 Attenuation and Dispersion of Leaky Rayleigh Waves

In addition to the geometric decay due to the effect of point loading, which varies as $1/\sqrt{r}$ along the interface for the Rayleigh wave, there is another type of attenuation caused by continuous radiation (leakage) of energy into the fluid. In frequency domain, the solutions are exponential functions of $(-\xi r)$, where $-\xi$ has the physical meaning of wavenumber. According to Eq. (4.35), higher

frequency (larger ξ) contents give more attenuation during propagation. Therefore the waveform generated by a transient loading becomes wider with increasing distance, i.e., it shows dispersion property due to leakage-induced attenuation, although the phase velocity of leaky Rayleigh waves does not vary with frequency.

4.4.4 Scholte Wave Response

The real roots of the Scholte equation correspond to Scholte wave propagation along the interface. The Scholte wave solutions can be obtained by calculating the residues at the poles $\gamma = \pm\gamma_{sch}$. For common cases of light fluids lying on stiff solids, the root $|\gamma_{sch}| = s_{sch}/s_{\mathrm{S}}$ is slightly larger than $u = s_{\mathrm{F}}/s_{\mathrm{S}}$. Therefore, Eqs. (4.36) and (4.44) are changed to

$$\begin{aligned}
[\alpha_1 z + pt]_{p=i\xi/\pm s_{\mathrm{S}}\gamma_{sch}} &= -\xi r m_{1,2}^{sch}, \\
[-\alpha_2 z + pt]_{p=i\xi/\pm s_{\mathrm{S}}\gamma_{sch}} &= -\xi r n_{p1,2}^{sch}, \\
[-\beta z + pt]_{p=i\xi/\pm s_{\mathrm{S}}\gamma_{sch}} &= -\xi r n_{s1,2}^{sch}.
\end{aligned} \tag{4.49}$$

where

$$\begin{aligned}
m_{1,2}^{sch} &= -\frac{1}{\gamma_{sch}}\left(\sqrt{\gamma_{sch}^2 - u^2}\frac{z}{r} \pm i\frac{t}{s_{\mathrm{S}} r}\right), \\
n_{p1,2}^{sch} &= \frac{1}{\gamma_{sch}}\left(\sqrt{\gamma_{sch}^2 - q^2}\frac{z}{r} \pm i\frac{t}{s_{\mathrm{S}} r}\right), \\
n_{s1,2}^{sch} &= \frac{1}{\gamma_{sch}}\left(\sqrt{\gamma_{sch}^2 - 1}\frac{z}{r} \pm i\frac{t}{s_{\mathrm{S}} r}\right).
\end{aligned} \tag{4.50}$$

The solutions for the leaky Rayleigh wave are also valid for the Scholte wave by substituting m^{sch}, n_p^{sch} and n_s^{sch} for m, n_p and n_s. The first terms in the expressions of Eq. (4.50) represent the real parts, which are positive and result in the decay in z direction. It can be seen that the Scholte wave decays exponentially in z direction in both the fluid and the solid. For lighter fluid cases, i.e., where the acoustic impedance of the fluid is less than that of the solid, $\sqrt{\gamma_{sch}^2 - u^2}$ is much smaller than $\sqrt{\gamma_{sch}^2 - 1}$ and $\sqrt{\gamma_{sch}^2 - q^2}$. This indicates that the Scholte wave attenuates much more quickly in the solid than in the fluid. Therefore, in contrast to the leaky Rayleigh wave, most of Scholte wave energy is localized in the fluid [30]. The Scholte wave generation efficiency increases with increasing acoustic impedance of the fluid. For example, it is much easier to generate Scholte waves in the water/concrete than the air/concrete configuration. In fact, almost no Scholte wave effect can be observed in air/concrete case. With increasing impedance of the fluid, Scholte waves have deeper penetration depth in the solid. This property provides the possibility for NDT application of Scholte waves, which was studied experimentally by Glorieux et al. [28]. Because there is no leakage during Scholte wave propagation along the radial direction, the decay in the radial direction is only attributed to the geometrical effect. In 2-D cases, the Scholte wave travels without attenuation along the propagation direction [28].

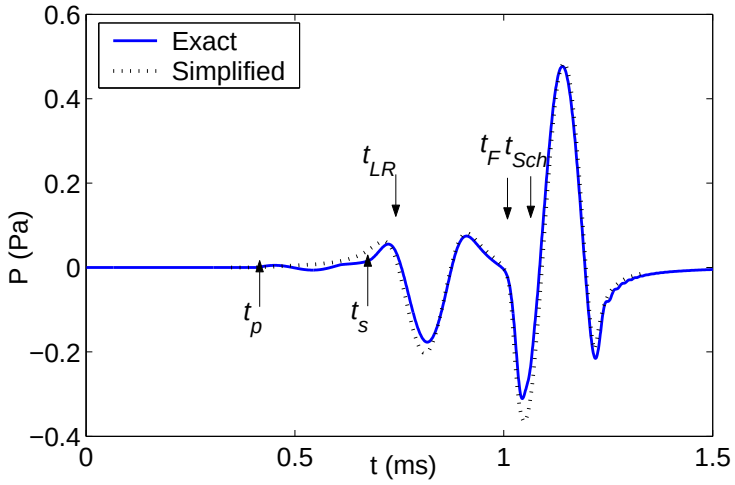

(a)

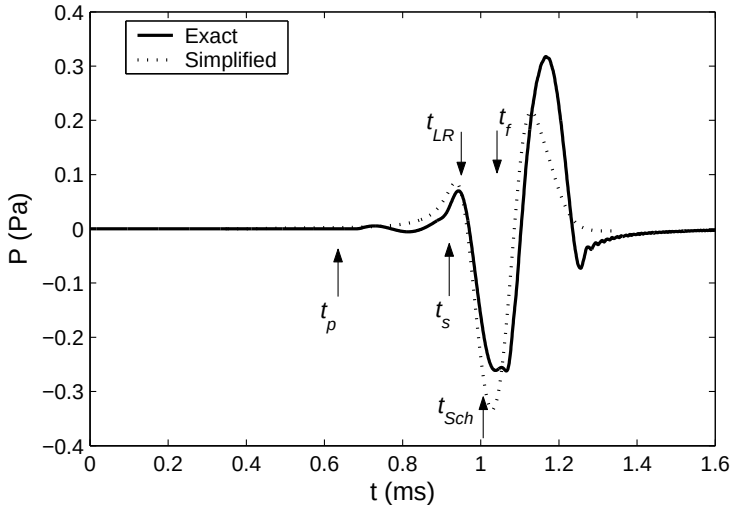

(b)

Figure 4.8: Comparison of the exact and simplified solutions for water/concrete case. Pressure in the fluid measured at position (a) $r = 1.5m, z = -0.05m$,and (b) $r = 1.5m, z = -0.5m$. The interface is subject to a point load that varies with time as $f(t) = sin^2(\pi t/T)$ with T=200μs. Material parameters for the fluid $\rho_1 = 1000kg/m^3$, $C_{\mathrm{F}} = 1500m/s$; for the solid $\rho_2 = 2400kg/m^3$, $C_{\mathrm{P}} = 4000m/s$, $\nu = 0.25$.

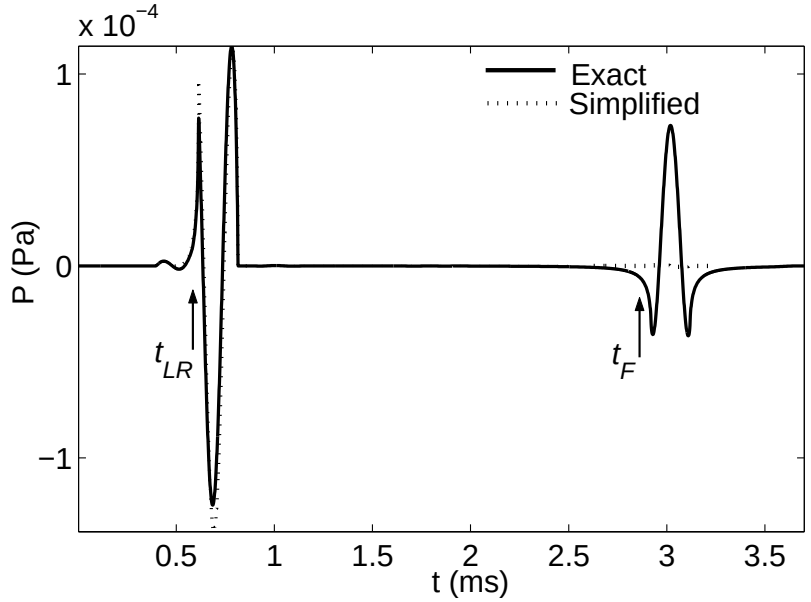

(a)

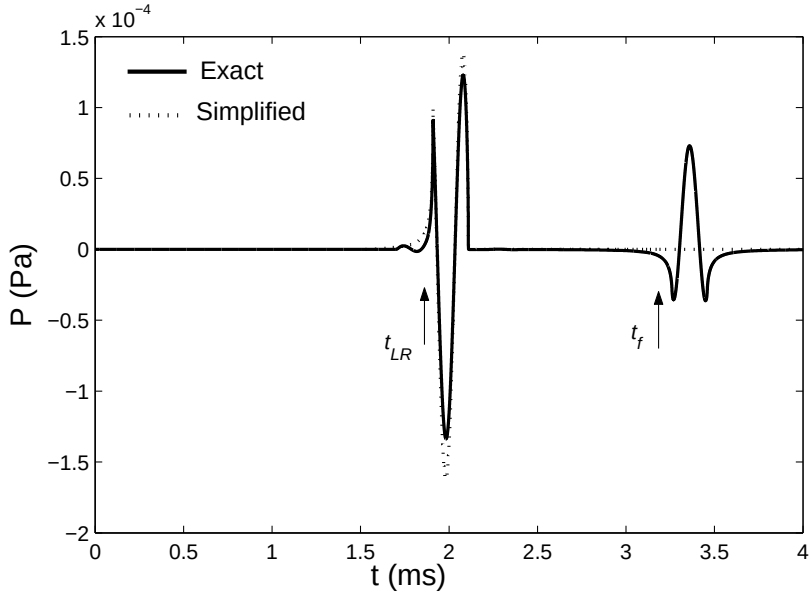

(b)

Figure 4.9: Comparison of the exact and simplified solutions for air/concrete case. (a) r =1.0m, z=-0.05m, and (b) r =1.0m, z=-0.5m. The interface is subject to a point load that varies with time as $f(t) = sin^2(\pi t/T)$ with T=200μs. Material parameters for the air $\rho_1 = 1.29kg/m^3$, $C_{\text{F}} = 343m/s$; for the solid $\rho_2 = 2400kg/m^3$, $C_{\text{P}} = 4000m/s$, $\nu = 0.25$.

4.4.5 Comparison of the Exact and Simplified Solutions

Figure 4.8 shows the comparison of the exact and simplified analytical solutions for fluid pressure for the water/concrete case. In Fig. 4.8(a), when the receiver position is close to the interface ($r = 1.5m, z = -0.05m$), good agreement is observed around the leaky Rayleigh and Scholte wave arrival times. The small yet noticeable differences before the leaky Rayleigh and Scholte wave arrivals are due to the absence of leaky body waves and fluid acoustic waves in the simplified solution. When the receiver is away from the interface, as shown in Fig. 4.8(b) for receiver position ($r = 1.5m, z = -0.5m$) , the degree of agreement between the simplified and exact analytical solutions decreases. Generally speaking, the simplified solution provides better estimation of pressure for larger r and smaller $|z|$ cases, where the contribution of body waves is negligible.

Figures 4.9(a) and 4.9(b) show the comparison of the exact and simplified solutions for the air/concrete case. The receiver positions are $r = 1.0m, z = -0.05m$ and $r = 1.0m, z = -0.5m$, respectively. Good agreement is observed near the leaky Rayleigh wave arrival time for both positions, while obvious differences can be seen near the Scholte and fluid acoustic wave arrival times. The reason is that the leaky Rayleigh wave is well separated from the fluid acoustic wave, and Scholte wave contribution is very small compared to the acoustic wave contribution in the fluid for air/concrete case, even in the near-interface region. Therefore, for the air/concrete configuration, the pressure field in the fluid is dominated by the leaky Rayleigh and acoustic waves. In air-coupled sensing, the leaky Rayleigh wave is usually the component in which we are interested. The acoustic wave contribution in the fluid can be separated by increasing measuring distance r between receivers and the source, or eliminated by employing the directional property of the air-coupled sensor [74].

The excitability of leaky Rayleigh waves induced by an impact point load $f(t) = sin^2(\pi t/T)$ can be inferred from Fig. 4.9. For a typical impulse force with a modest peak value of 1.0kN and duration $T = 200\mu s$, the output pressure of the leaky Rayleigh wave is around 0.1-0.15Pa, which is approximately equivalent to a sound pressure level of 75dB. Such a pressure is large enough to be detected readily by an air-coupled sensor, even when material attenuation effects are considered. The excitability of leaky Rayleigh waves is also dependent on the impact force duration. Shorter impact duration gives higher output pressure of leaky Rayleigh waves. For example, when the duration is decreased to $T = 50\mu s$, the output peak pressure of the leaky Rayleigh wave will increase to 1.2Pa (95dB). Most impactors used for concrete testing will generate forces with duration between $50 - 200\mu s$.

4.5 Explosive Sources in Fluid

de Hoop derived the solution of fluid pressure excited by an explosive point source [21] and a line source [20] in the fluid. Explosive sources have been used to generate Scholte waves in sea floor to characterize properties of ocean bottom [8, 12, 55]. For an explosive point source model shown in Fig. 4.10, the Green's function of fluid pressure is given by de Hoop [21] in transformed domain as

$$\tilde{G}_f^r(\xi, p) = \frac{R_f(\xi, p)}{2p\alpha_1} \exp\left[-\alpha_1(z + h)\right], \tag{4.51}$$

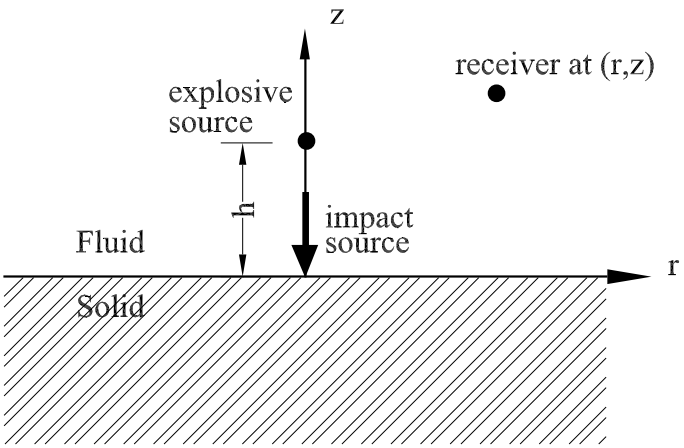

Figure 4.10: Transient point loads applied to the fluid-solid half-space system.

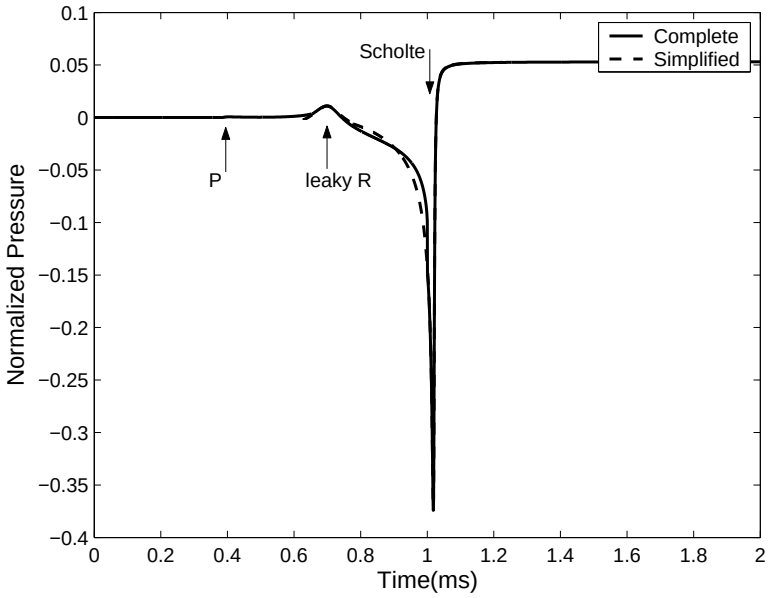

Figure 4.11: The complete and simplified solution of Green's function $G_f^r(t)$ for $r = 1.5m$ and $z = h = 0.01m$. Material parameters for the fluid: $\rho_1 = 1000kg/m^3, C_{\mathrm{F}} = 1500m/s$; for the solid, $\rho_2 = 2400kg/m^3, C_{\mathrm{P}} = 4000m/s, \nu = 0.25$.

where $\tilde{G}_f^r$ is the Green's function of the reflected wave pressure in transformed domain. z and h are heights of the receiver and point source, and they have positive signs in the fluid. p and α_1 have the same definition as in section 4.2. $R_f(\xi, p)$ represents the ratio between the reflected waves and the incident waves, and is defined as

$$R_f(\xi,p) = \frac{D_R - \dfrac{\rho_1}{\rho_2}\dfrac{\alpha_2}{\alpha_1}p^4 s_{\mathrm{S}}^4}{D_R + \dfrac{\rho_1}{\rho_2}\dfrac{\alpha_2}{\alpha_1}p^4 s_{\mathrm{S}}^4}, \tag{4.52}$$

where

$$D_{\mathrm{R}}(\xi,p) = (s_{\mathrm{S}}^2 p^2 + 2\xi^2)^2 - 4\xi^2\alpha_2\beta. \tag{4.53}$$

The time-space domain expression of $G_f^r(t)$ is also given by de Hoop in integral form. Fig. 4.11 shows the Green's function $G_f^r(t)$ vs. time for a source/receiver spacing $r = 1.5m$, while $z = h = 0.01m$. Material parameters are selected to simulate the water/concrete half space system.

With the same approach as in section 4.4, a simplified solution of $G_f^r(t)$ can also be obtained from the residue at corresponding poles. The solution corresponding to the Scholte wave response is given by

$$G_f^r \;=\; \frac{1}{r}\mathrm{Re}\left[\frac{A_1}{(1+m^2)^2}\right], \quad \mathrm{Re}(m) > 0, \tag{4.54}$$

where

$$m = \frac{1}{\gamma_{sch} r}\left[(z+h)\sqrt{\gamma_{sch}^2 - u^2} - \frac{it}{s_{\mathrm{S}}}\right] \tag{4.55}$$

$$A_1 = \left[\frac{\xi}{2p\alpha_1}\frac{D_R - \dfrac{\rho_1}{\rho_2}\dfrac{\alpha_2}{\alpha_1}p^4 s_{\mathrm{S}}^4}{\partial D_H/\partial p}\right]_{p=\dfrac{i\xi}{s_{\mathrm{S}}\gamma_{sch}}}. \tag{4.56}$$

The leaky Rayleigh wave response can also be obtained by calculating the residue at the pole $p = \dfrac{i\xi}{s_{\mathrm{S}}\gamma_R}$.

The simplified solution $G_f^r(t)$ for $r = 1.5m$ and $z = h = 0.01m$ is also shown in Fig. 4.11. The simplified solution consists contributions from Scholte waves and leaky Rayleigh waves (for the stiff solid/fluid case) only. It is seen that the simplified solution agrees with the complete solution very well nearby arrivals of leaky Rayleigh waves and Scholte waves.

4.6 Applications of Fluid/Solid Interface Waves to Underwater NDT

Fluid-solid interface waves can be used to characterize elastic properties of the solid along which the waves travel. The applications range from geophysics to quantitative non-destructive testing of structures. There are two types of interface waves in a fluid-solid system: the Scholte wave and the

leaky Rayleigh wave. The latter exists only for stiff solid - light fluid cases, where the shear wave velocity of the solid C_{S} is larger than the fluid velocity C_{F} . Both types of interfaces waves can be excited by a transient point load that is normally applied to the solid at the interface. For the stiff solid/light fluid case, leaky Rayleigh waves (or general Rayleigh waves) can be effectively excited and used to characterize properties of solids, for example NDT of concrete using air-coupled sensors [74, 75], underwater NDT of concrete or steel structures and seabed rock [37].

Scholte waves exist for any combination of fluids and solids. The fraction of energy that travels in the fluid and solid respectively depends on the relative densities and velocities of the materials. For the stiff solid/light fluid case, such as underwater concrete structure or seabed rock, more energy will be localized in the fluid than in the solid. On the other hand for a compliant solid with lower modulus and density, such as sea sediment, more energy will be localized in the solid; therefore Scholte waves have deeper penetration in the solid. And in this case, Scholte waves can be used to characterize the properties of the solid. Scholte waves have been successfully applied to characterize marine sediment [8, 45, 55] and underwater geotechnical sites [37], where Scholte waves were excited either by an air gun shot in the water [8, 37, 45, 55] (explosive source) or a mechanical vibrator [37] (normal point load applied to the solid surface). Scholte waves are monitored on either particle velocity recordings at the interface (geophone) or pressure recording in the fluid (hydrophone). Surface wave dispersion curve measurement techniques for solids, such as SASW (Spectral Analysis of Surface Waves) and MASW (Multi-channel Analysis of Surface Waves) methods, can also be applied to measure shear wave velocities of underwater solids [8, 12, 45, 55]. Thus a study of interface wave excitation and sensing in these cases has practical value. The following section studies the effectiveness of interface waves excitation and detection for two cases: stiff solid/water and compliant solid/water.

4.6.1 Interface Waves Responses

Interface wave can be monitored by measuring either pressure in the fluid or particle velocities at the interface. Figure 4.12 shows the pressure $P(t)$ and vertical velocity $V_z(t)$ response excited by an impact point load on the fluid/solid interface. The pressure is measured in the fluid at $r = 1.5m, z = 0.005m$, while the velocity is measured on the interface at $r = 1.5m, z = 0m$. Material parameters are selected to simulate water/concrete configuration. For the fluid: $\rho_1 = 1000kg/m^3, C_{\mathrm{F}} = 1500m/s$ and for the solid, $\rho_2 = 2400kg/m^3, C_{\mathrm{P}} = 4000m/s, \nu = 0.25$. Arrival times of P-, S-, leaky Rayleigh waves and Scholte waves are marked in the figure. Figure 4.8 has shown that the acoustic wave contribution in this case is negligible, therefore the large pulse near Scholte wave arrival is mainly a Scholte wave contribution. It can be seen that the pressure response in the water is similar to the velocity measured at the interface, except there is a phase shift for the Scholte wave pulse.

The particle trajectories of leaky Rayleigh waves and Scholte waves in the fluid are elliptical. According to Viktorov[68], the amplitude ratio between vertical and horizontal components of displacement is

$$|w/u| = \left| \sqrt{1 - C^2/C_{\mathrm{F}}^2} \right|, \tag{4.57}$$

where C is the phase velocity of either the leaky Rayleigh wave C_{LR} or the Scholte wave C_{sch}.

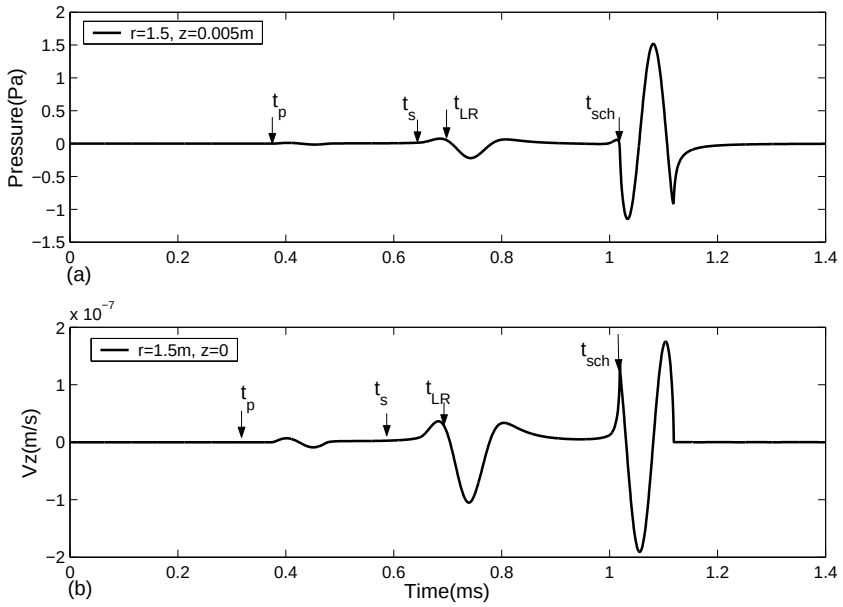

Figure 4.12: Comparison of (a) pressure in the fluid and (b) particle velocity at the interface between water/stiff solid half-spaces. Material parameters for water: $\rho_1 = 1000kg/m^3, C_{\rm F} = 1500m/s$; for the solid, $\rho_2 = 2400kg/m^3, C_{\rm P} = 4000m/s, \nu = 0.25$.

Because Scholte wave velocity $C_{\rm sch}$ is always less than $C_{\rm F}$, $w/u < 1$ always. Therefore the major axis of the trajectory ellipse is in the propagation direction. For fluid/stiff solid configurations, $C_{\rm sch}$ is very close to $C_{\rm F}$, therefore u will be much larger than w , and the trajectory ellipse will be very flat. For leaky Rayleigh waves, the major axis of the trajectory ellipse is in the vertical direction when $C_{\rm LR} > \sqrt{2}C_{\rm F}$. The same relation applies to particle velocity too.

Fluid pressure is linearly related to the magnitude of particle velocities, considering contributions from all directions. Because the horizontal component dominates the Scholte wave response, it can be inferred that the pressure response of Scholte waves will be stronger than the vertical component response of particle velocity. From Fig. 4.12, it can be seen that for the impact force $f(t) = \sin^2(\pi t/T)$ with input force magnitude of 1.0 kN, the peak pressures of the leaky Rayleigh wave and Scholte wave are 0.23 kPa and 1.09 kPa respectively, both of which can be readily measured by hydrophones with sensitivity above -200 dB (0.1 V/kPa). However, for the same loading condition, the peak velocity responses at the interface induced by leaky Rayleigh waves and Scholte waves are only 0.105 mm/s and 0.19 mm/s respectively, which are difficult to detect using most geophones without further amplification. Therefore we conclude that measuring pressure of interface waves with hydrophones is more effective than measuring particle velocity V_z with geophones for normal point load excitation.

4.6.2 Excitability of Scholte Waves at the Fluid/Compliant Solid Interface

Scholte waves can be excited by an explosive source in the fluid or a normal point load on the solid at the interface. To investigate the excitability of Scholte waves by different types of sources, pressure responses for the water/compliant solid configuration are considered, where shear wave velocity in

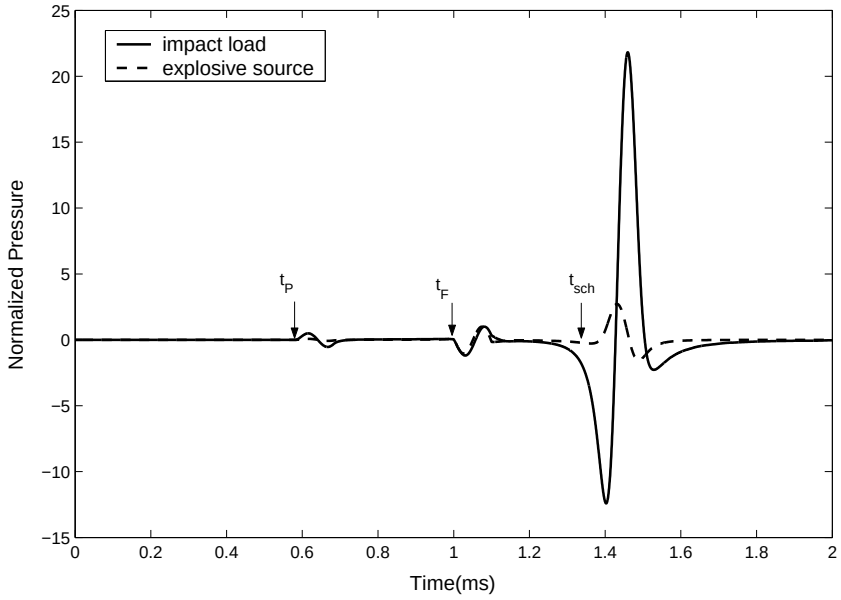

Figure 4.13: Comparison of fluid pressures excited by a normal point load and an explosive source for the water/compliant solid configuration. The normal point load is applied at the water/solid interface and the explosive source is in water at r=h=0m. Pressures are normalized with respect to that of acoustic waves. Material properties for the solid are $\rho_2 = 1200kg/m^3, C_{\rm P} = 2700m/s, \nu = 0.31$.

the solid $C_{\rm S}$ is lower than $C_{\rm F}$. Because the Scholte wave velocity is lower than both of $C_{\rm S}$ and $C_{\rm F}$, the Scholte wave pulse arrival can be differentiated from acoustic waves in water in time domain signals.

Figure 4.13 shows pressure responses at $r = 1.5m, z = 0.05m$ in water resulting from an impact point load and an explosive source respectively. The explosive source is placed in water, infinitely close to the interface. The solution of pressure owing to an explosive source in the fluid is described by de Hoop et al.[21]. Material properties for the compliant solid are $\rho_2 = 1200kg/m^3$, $C_{\rm P} = 2700m/s$ and $\nu = 0.31$. Because $C_{\rm S}$ is lower than $C_{\rm F}$, leaky shear waves and leaky Rayleigh waves do not exist. Only leaky P waves, direct acoustic waves and Scholte waves exist, and they are indicated by the three pulses shown in Fig. 4.13. Pressure amplitudes are normalized with respect to that of the direct acoustic wave pulse. It is seen in Fig. 4.13 that the normalized Scholte wave amplitude excited by a normal point source is 8 times of that by an explosive source. Therefore, the normal point load is more effective to generate Scholte waves than than the explosive source. A similar conclusion is obtained for leaky P waves. Reducing the relative amplitude of acoustic waves will improve measurement accuracy of interface waves, especially when it is difficult to differentiate interface waves from acoustic waves in the time domain because their arrival times are very similar.

4.6.3 Excitability of Leaky Rayleigh Waves at the Fluid/Stiff Solid Interface

To investigate the excitability of leaky Rayleigh waves by a transient normal point load, a fluid/stiff solid case is studied. The assumed material properties are selected to simulate a water/concrete configuration. In this case, Scholte wave velocity $C_{\rm sch} = 1471m/s$ is close to the fluid acoustic velocity

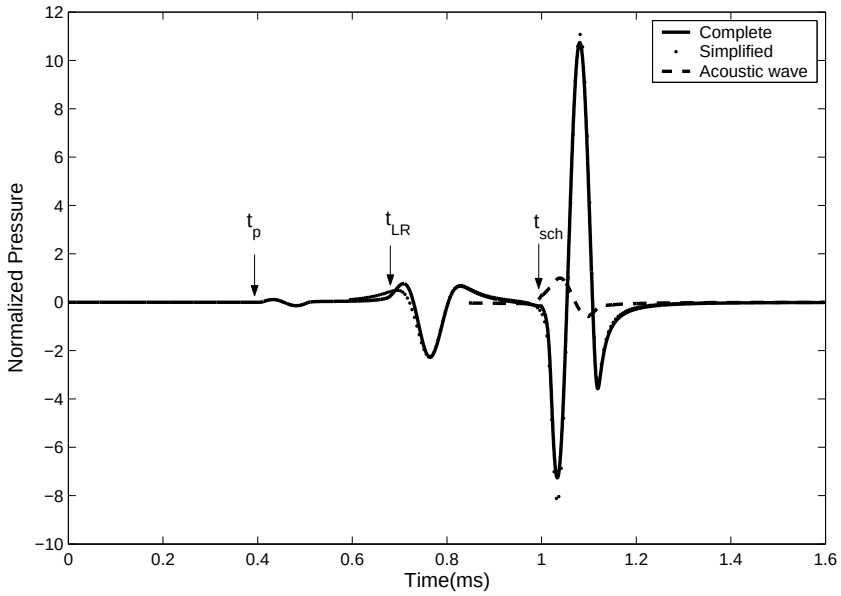

Figure 4.14: Complete and simplified solutions of pressure generated by a normal point load for the water/stiff solid configuration. The pressure is measured at $r = 1.5$ m, $z = 0.05$ m and normalized to the acoustic wave response. Material properties are the same as those in Fig. 4.12.

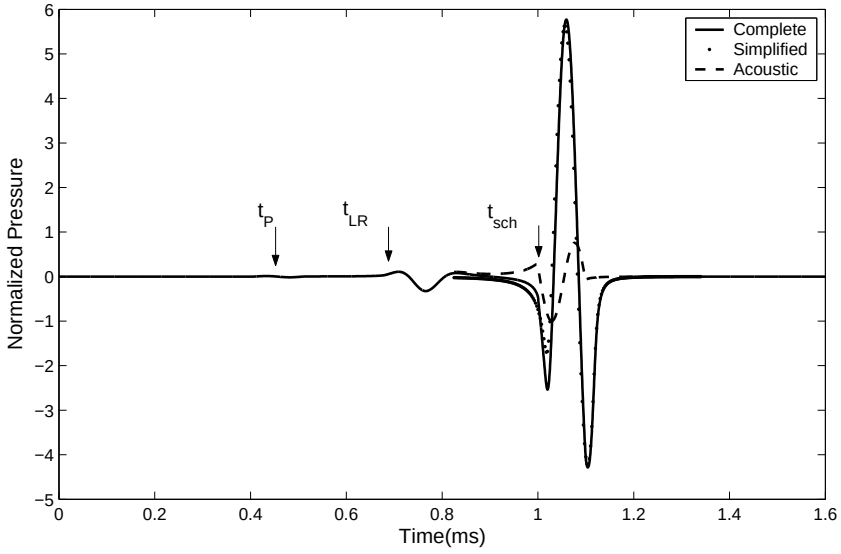

Figure 4.15: Complete and simplified solutions of pressure generated by an explosive load for the water/stiff solid configuration. The pressure is measured at r=1.5m, z=0.05m and normalized to the acoustic wave response. Material properties are the same as those in Fig. 4.12.

in water $C_{\mathrm{F}} = 1500m/s$. Therefore, the Scholte wave response cannot be directly differentiated from the fluid acoustic waves in the time domain signal. However, for responses excited by a normal point load, a simplified solution of leaky Rayleigh and Scholte wave responses has been derived in section 4.4. By calculating residues from corresponding poles, the simplified solution contains contributions only from leaky Rayleigh and Scholte waves. Figure 4.14 shows the complete and simplified solution of pressure at $r = 1.5m, z = 0.05m$ in water. The largest pulse in the figure is from the Scholte wave and acoustic wave contribution, and the pulse at $t = 0.6ms$ contains contribution from the leaky Rayleigh waves. Overall the two solutions agree well. The difference in two solutions nearby the Scholte wave arrival is because the direct acoustic waves are not considered in the simplified solution. The acoustic wave response can be isolated and obtained as the difference between the completed and simplified solutions. In Fig. 4.14, the responses are normalized with respect to peak amplitude of this acoustic wave response. By comparing the curves in Fig. 4.14, we can conclude that the response is dominated by leaky Rayleigh wave and Scholte waves. The normalized amplitude of Leaky Rayeligh wave is about 2.3, and that of the Scholte waves is about 10.7.

Figure 4.15 shows the normalized pressure at the same position generated by an explosive load in the fluid. The complete solution is given by de Hoop's [21], while the simplified solution is derived in section 4.5 using the residue approach. Similarly, the acoustic wave response is obtained from the difference between the complete and simplified solutions, and shown in Fig. 4.15 as a dashed line. It can be seen the response is dominated by the Scholte waves that has normalized amplitude of 5.8, while the leaky Rayleigh wave amplitude is only 0.33. Considering the results from Fig. 4.14 and Fig. 4.15, we can conclude that the normal point load is more effective to excite leaky Rayleigh waves than the explosive source. In this case, with the same acoustic wave excitability, the leaky Rayleigh wave excitability from the normal point load is about 7 times of that of an explosive source (normalized leaky Rayleigh wave response: 2.3 in Fig. 4.14, and 0.33 in Fig. 4.15). Both sources are very effective to excite Scholte waves.

4.6.4 Effect of Explosive Source Height on Interface Wave Excitability

The excitability of interface waves by an explosive load depends on the height of the source. Figure 4.16 shows pressure responses generated by an explosive source at six positions with height h=0$\sim$0.5 m. The pressures were calculated at r=1.5 m, z=0.05 m in water for the water-compliant solid configuration. As shown in the figure, arrival times of leaky P waves vary linearly with the source height h, while the amplitude is relatively insensitive to the source height. The second and third pulses in the signals are from acoustic wave and Scholte wave contributions. To further investigate the decay pattern of Scholte waves with increasing source height, the peak amplitude of each wave pulse is plotted vs. the source height h in Fig. 4.17. It is seen that Scholte waves decay quickly, on the order of h^{-2} with source height. This observation agrees with Ritzwoller's [55] results.

The effect of source height on pressures in the water/stiff solid configuration is shown in Fig. 4.18. This figure shows some interesting findings. Unlike Scholte waves, the amplitude of leaky Rayleigh waves is insensitive to the variation of source height. Leaky Rayleigh waves do not decay with increasing source height, but in fact show a slight increase in amplitude. Therefore, when an explosive source is used to generate leaky Rayleigh waves, the source can be positioned at any

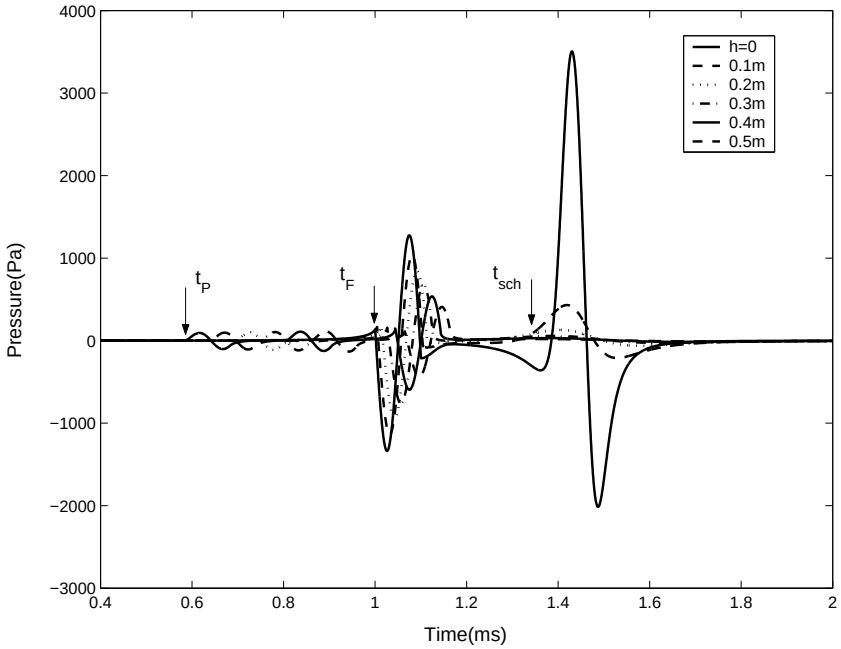

Figure 4.16: Pressure responses vs. height of the explosive source for the water/compliant solid configuration. Source height $h = 0\ 0.5$ m. The pressures are calculated at r=1.5m, z=0.05m in water. Material properties are the same as those in Fig. 4.13.

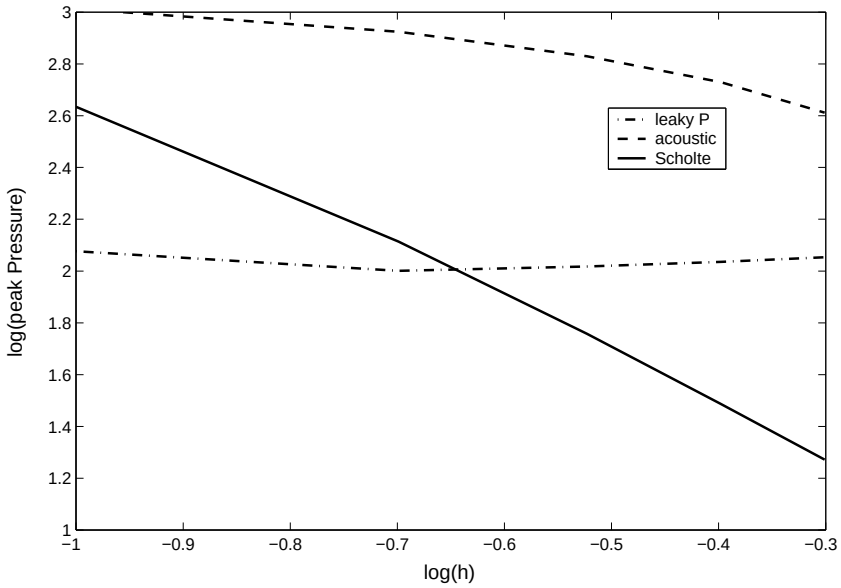

Figure 4.17: Decay of leaky P, acoustic and Scholte waves with increased source height for the water/compliant solid configuration. Material properties are the same as those in Fig. 4.13.

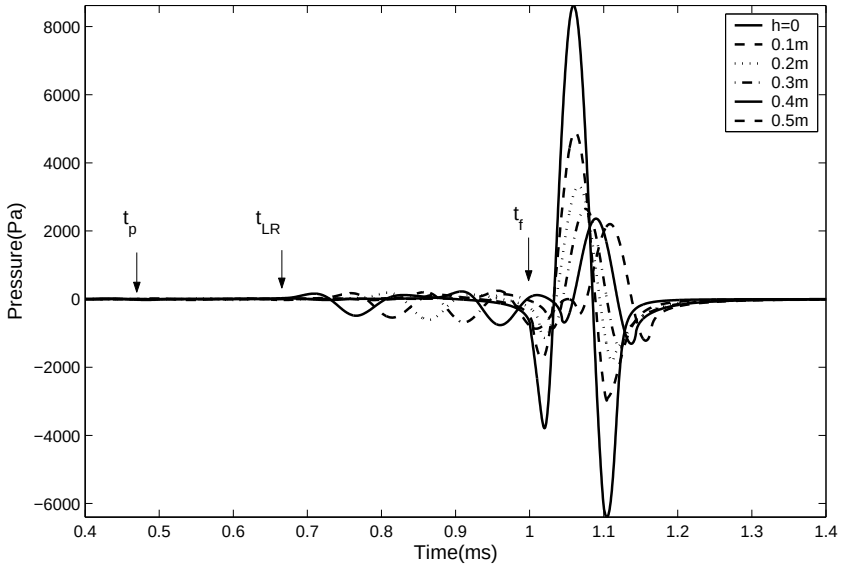

Figure 4.18: Pressure responses vs. height of the explosive source for the water/stiff solid configuration. Source height $h = 0\ 0.5$ m. The pressures are calculated at $r = 2.5$ m, $z = 0.05$ m in water for the water/stiff solid configuration. Material properties are the same as those in Fig. 4.12.

height above the interface. The only requirement is to maintain proper source-receiver spacing, so that leaky Rayleigh waves can be separated from the acoustic waves in the time domain.

4.7 Applications to Air-coupled Sensing

Figure 4.9(a) shows that the signal measured in air is dominated by leaky Rayleigh waves and direct acoustic waves nearby the interface. The contribution of leaky P-, S-waves and Scholte waves are so small that they can be neglected. The snapshot of wave field (displacement) shown in Fig. 4.19 illustrates the contribution of each type of waves.

In section 4.4.5, we have derived the excitability of leaky Rayleigh waves induced by an impact point load. For a typical impulse force, the excitability of leaky Rayleigh waves is about 0.1Pa/kN, equivalent to a sound pressure level of 75 dB. Such a pressure is large enough to be detected readily by an air-coupled sensor or microphone. The normal room noise level is in the range of 40-60 dB, which is below this leaky Rayleigh wave level. Furthermore, the ambient noise effects can also be reduced by using directional air-coupled sensors, such as microphones with hyper-cardioid polar patterns.

The direct acoustic wave pressure P_F is in the same order of leaky Rayleigh waves P_{LR}. Depending on measuring locations, P_F may be larger or smaller than P_{LR}. The direct acoustic wave does not provide any information about the mechanical properties of the solid, and its existence interferes the signal explanation; therefore it needs to be eliminated or suppressed. Because the acoustic waves in air (≈ 340 m/s) travel much slower than the leaky Rayleigh waves in the concrete (2100-2700 m/s), the acoustic waves can be separated by simply increasing the measuring distance along the surface.

It can be seen from Fig. 4.19 that the leaky Rayleigh wave response decays with radial distance

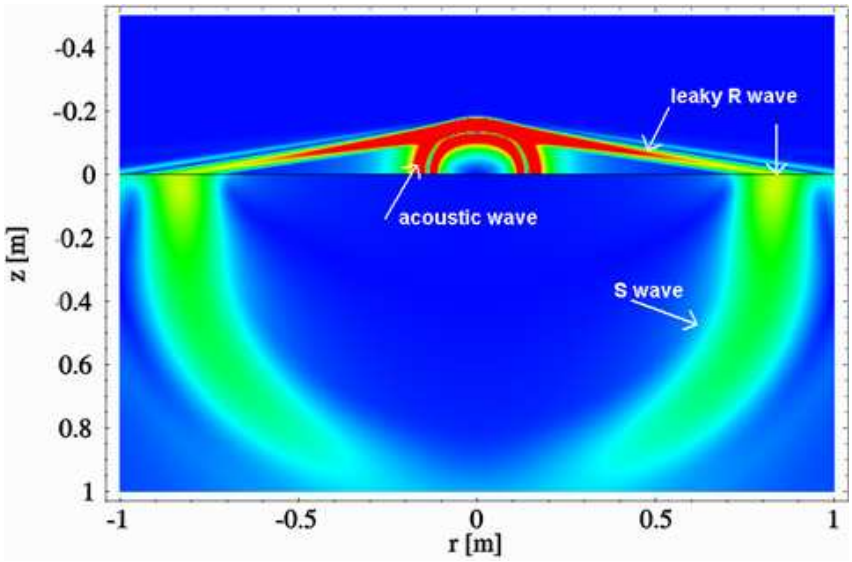

Figure 4.19: Snapshot of wave field (displacement) in air-concrete half spaces (EFIT simulation). Material parameters for air: $\rho_F = 1.21kg/m^3, C_{\mathrm{F}} = 343m/s$; for concrete, $\rho_2 = 2400kg/m^3, C_{\mathrm{P}} = 4000m/s, \nu = 0.25$.

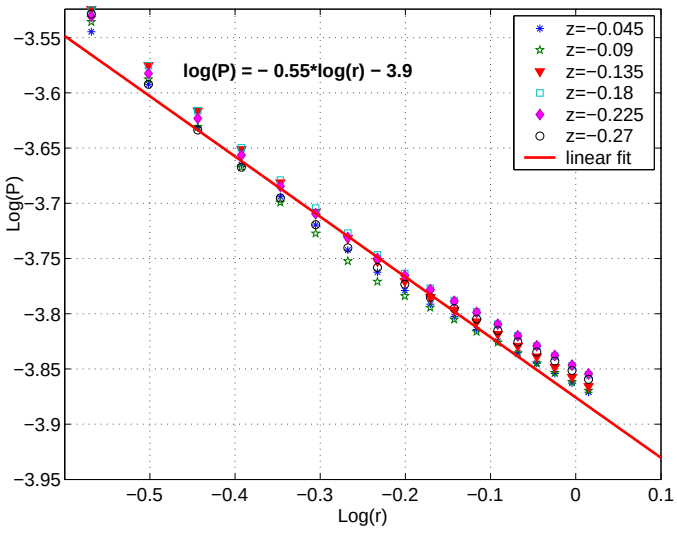

Figure 4.20: Attenuation of the leaky Rayleigh wave along the radial direction, in the range of $r = 0.27 \sim 1.035m; z = -0.045 \sim -0.27m$

r along the wavefront. The peak amplitude occurs in the leaky direction. To further study the attenuation of leaky Rayleigh waves along radial direction, the peak values of leaky Rayleigh waves in the region of $r = 0.27 \sim 1.035m, z = -0.045 \sim -0.27m$ are plotted in Fig. 4.20. For each given height z, P_{LR} exponentially attenuates with distance r. In the Log(P)$\sim$Log(r) plot, the slope of fitted line is -0.55, which is close to -0.5 in the free surface half space case. Thus leaky Rayleigh waves decay at a slightly faster rate than the ordinary Rayleigh waves in the free surface solid because energy leaks into air.

Also, leaky Rayleigh waves show dispersive phenomenon during propagation, which is displayed as wave pulses becoming wider with increased distance. However, this type of dispersion is different from the dispersion of Rayleigh waves in layered solids, which causes phase velocity variation with frequency. Leaky Rayleigh waves propagate at a constant velocity along the fluid/solid interface.

4.8 Conclusions

Theoretical analyses were presented in this chapter for complete and simplified solutions to the Lamb's problem in a fluid/solid system. The following conclusions are drawn based on the analyses:

1. *A transient point load normally applied to the interface is an effective way to generate Leaky Rayleigh waves in the fluid.* For air-coupled sensing in concrete, the excitability of leaky Rayleigh waves is around $0.1 \sim 1.0$ Pa/kN, depending on the impact force duration. Leaky Rayleigh waves have large enough amplitude to be detected by air-coupled sensors in air. Considering the frequency range used for concrete tests, microphones are good candidates as air-coupled sensors.

2. *Scholte waves can be effectively excited by either a normal impact point load or an explosive source.* Scholte waves can be generated in any fluid/solid combination, but the largest excitability is obtained in fluid/compliant solid systems. Therefore, Scholte waves are commonly used for geophysical sea sediment characterization. The normal impact load applied on the fluid/solid interface induces higher Scholte wave excitability.

3. *The height of explosive sources has significant effect on Scholte wave excitability.* The Scholte wave excitability decreases rapidly with the increasing source height, as a function of h^{-2}. However, the source height has very little influence on the leaky Rayleigh wave excitability.

4. *Leaky Rayleigh waves can be separated from the direct acoustic waves by careful testing setup configuration.* Small sensing height $|z|$ is recommended for easy separation of direct acoustic waves and leaky Rayleigh waves. Smaller $|z|$ also results in a smaller blind zone, where no leaky Rayleigh wave exists.

5. *Both the complete and simplified solutions are derived for the Lamb's problem in a fluid/solid system.* The simplified solutions provide an easy way to quickly estimate interface wave responses and extract interface waves from other waves.

With the guidance of theoretical analysis, the next chapter investigates the feasibility of using air-coupled sensors to detect surface waves in concrete.

5 Measuring Leaky Rayleigh Waves in Concrete Using Air-coupled Sensors

5.1 Testing Setup and Equipment

5.1.1 Testing Setup

Figure 5.1 shows the testing scheme for air-coupled leaky surface wave sensing in concrete. The whole testing system includes an impact source, air-coupled sensors and a data acquisition system. An impact point source is applied at the surface to generate surface waves in concrete. The resulting motion at each surface point of the solid causes an acoustic wave to "leak" into the surrounding air. The superposed leaky waves that emanate from each point in motion form leaky bulk (P- and S-waves) and surface wave wavefronts. A sensitive air-coupled sensor or microphone is placed above the concrete surface at height h. The horizontal projection of spacing between the source and sensor is r.

In addition to leaky waves (P-, S- and surface waves), the air-coupled sensor also senses the direct acoustic waves generated by the source. Since the acoustic waves do not carry any useful information about the solid, the testing setup should be designed to reduce the effect of acoustic waves. One solution is to increase the source-receiver spacing r, so that the acoustic waves arrive much later than leaky waves and thus can be separated in time. Another solution is to use directional air-coupled sensors, which attenuate waves that have large incident angle. Increasing r also increases the incident angle of acoustic waves.

The leaky angle θ is determined by Snell's law as

$$\sin(\theta) = \frac{C_{\text{air}}}{C_{\text{LR}}}, \tag{5.1}$$

where C_{air} and C_{LR} are the acoustic wave velocity in air and leaky Rayleigh wave velocity in solids. For concrete, the normal values of C_{air} and C_{LR} are 343 m/s and $2000 \sim 2200$ m/s, respectively. Thus θ varies between 8 to 10 degrees. Since most air-coupled sensors have a sensing field angle larger than 10 degrees, the leaky surface waves can be effectively detected if the sensor is installed with its axis normal to the testing surface.

The expected arrival times for leaky surface and direct acoustic waves can be calculated from the equations

$$\begin{aligned} t_{\text{LR}} &= \frac{r}{C_{\text{LR}}} + \sqrt{\frac{1}{C_{\text{air}}^2} - \frac{1}{C_{\text{LR}}^2}}, \\ t_{\text{air}} &= \frac{\sqrt{r^2 + h^2}}{C_{\text{air}}}. \end{aligned} \tag{5.2}$$

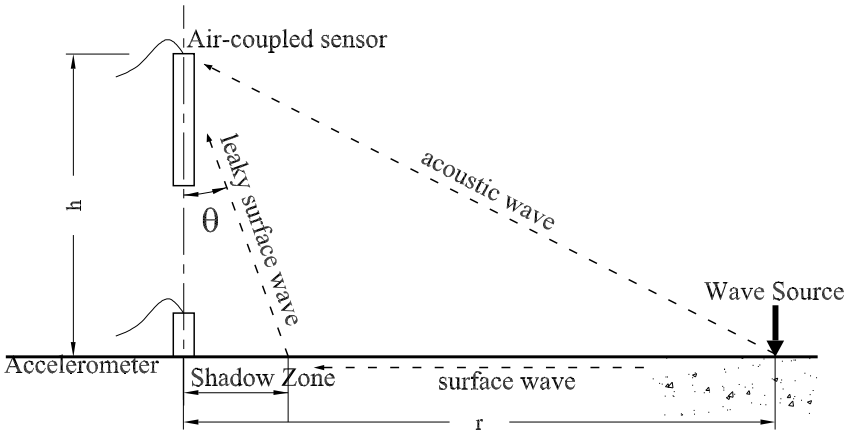

Figure 5.1: Testing scheme for air-coupled leaky surface wave detection.

5.1.2 Shadow Zone

A shadow zone exists nearby the sensor region, where no leaky surface waves can be detected, as shown in Fig. 5.1. The shadow zone size is $h\tan(\theta)$. The shadow zone complicates data analysis, and reduces the effective testing region. Therefore, the shadow zone should be minimized. Because the leaky angle θ is relatively stable, which varies around 8 to 10 degrees for normal concrete, the only way to minimize shadow zone size is to reduce the sensor height h.

For leaky surface wave sensing, larger r and smaller h is recommended to reduce negative effects of the direct acoustic waves and shadow zone.

5.1.3 Air-Coupled Sensors

Air-coupled sensors were developed in the 1970s and used for wood inspection and paper manufacturing quality control. The potential advantages and limitations of using air-coupled sensors to NDT applications have been recognized in 1980s [66]. Air-coupled sensing is particular useful for inspection of wood and paper products, art objects, and advanced composite materials used in the aerospace industry [29].

The most common transducers used for air-coupled experiments are based on piezoelectric and electrostatic designs. Piezoelectric air transducers are inherently resonant devices, and require special backing to obtain suitable damping coefficients. Another problem is the huge difference of the acoustic impedance between the piezoelectric element and that of air. A quarter-wavelength thick matching layer at the frequency of interest is thus usually introduced at the front surface. However, the application of a matching layer limits the overall bandwidth of the device. Thus these devices are usually used over a narrow bandwidth. [26].

Another type of transducer design is based on electrostatic or capacitance principles. These transducers have much broader bandwidths and high sensitivities. Grandia et al. [29] reviewed the NDE applications of different types of air-coupled sensors, and summarize the frequency re-

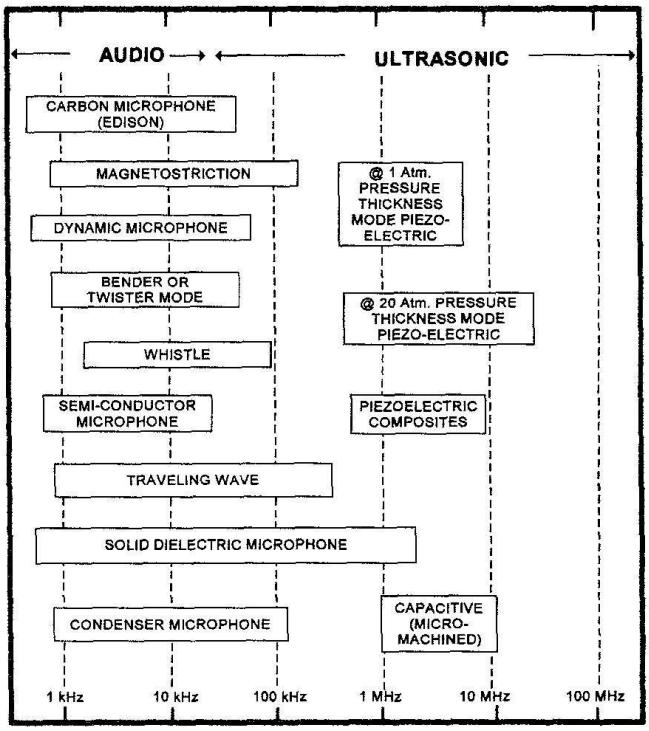

Figure 5.2: Frequency range of various air-coupled sensors [29].

gions that can be covered using different type transducers, as shown in Fig. 5.2. The electrostatic transducers include condenser microphones and micro-machined capacitive transducers. The most popular test and measurement microphones are the capacitor condenser designs.

5.1.4 Air-Coupled Sensor: Microphones

In chapter 4, the excitability of leaky surface waves in concrete was derived. For a typical impact force with duration between 50 and $200\mu s$ and amplitude of 1 kN, the excitability is between 1.0 to 0.1 Pa/kN, equivalent to the sound pressure level of 95 to 75dB. Shorter duration results in higher sound level. Unlike NDT of metals, low frequency waves, usually below 100 kHz, are usually used in civil engineering. Microphones are very sensitive air-coupled sensors, which have flat frequency response up to $20 \sim 25$ kHz. Therefore, microphones are good candidates for low frequency air-coupled sensing application.

When choosing the optimum microphone for air-coupled sensing in concrete, the parameters to consider include sensitivity, frequency response and directional property. Dynamic response and range are not an issue since the sound level used in NDT application has relatively narrow dynamic range.

Based on the selection criteria, several types of microphones were investigated for leaky surface wave detection. A highly directional microphone, the Shure SM89 shotgun microphone, was selected initially as the air-coupled sensor to detect leaky Rayleigh waves; it is shown in Fig. 5.3. The microphone has an end face diameter $d = 20$ mm and length = 386 mm. It has a flat frequency

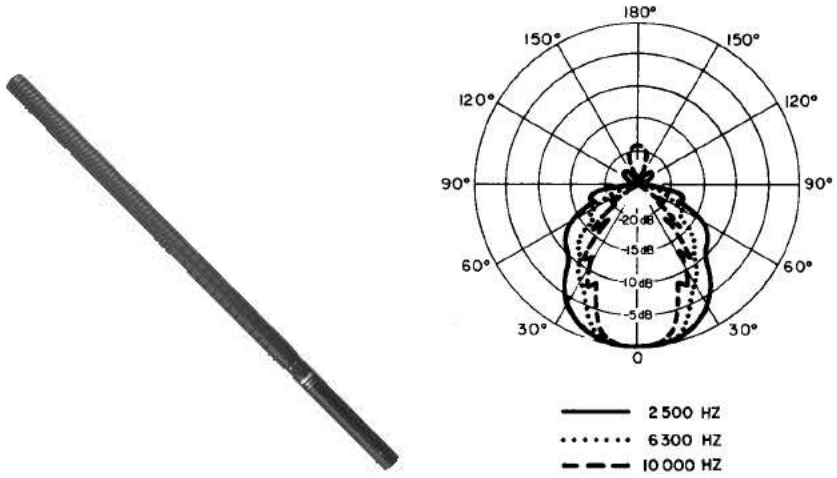

(a) (b)

Figure 5.3: Shure SM89 shotgun microphone. (a)The SM89 microphone; (b)The cardioid polar pattern

response up 20 kHz and hyper-cardioid sensing field (highly directional) that helps reduce the effect of ambient noise. The polar pattern sensing field is shown in Fig. 5.3(b). It can be seen that the microphone applies high attenuation on waves of high frequency and large incident angle. For example, with 30 degree incident angle, waves of 10 kHz will be attenuated by -10 dB; with 45 degree angle, signal attenuation becomes -20 dB. Since the direct acoustic waves usually have a large incident angle (more than 45 degree in most test setup), the effects of direct acoustic waves can be greatly reduced with the directional microphone. The leaky angle of Rayleigh waves is less than the microphone's receiving range, thus the leaky Rayleigh waves can be detected without attenuation. An array of SM89 microphones have been successfully used to image surface defects in concrete by measuring surface wave transmission ratio (section 6.4).

The sensitivity of the microphone is 22 mV/Pa. A phantom power supply is needed to bias the sensor and amplify signals.

However the physical length of the microphone (38 cm long from the tip to the sensing element) prevents the sensing element from being very close to the test surface, which causes a shadow zone size about 6 cm. To reduce the shadow zone size, smaller microphones were investigated.

Figure 5.4 shows a regular cardioid musical microphone. Its smaller size enables a smaller height h, and therefore smaller shadow zone. The smallest possible height is about 5 cm. The musical microphone has a 180 degree cardioid sensing field. Although it is less directional than the SM89, it works very well in the field to measure surface wave dispersion curves.

Both microphones mentioned above have a cutoff frequency below 25 kHz. To characterize thin layered structures with leaky surface waves or determine depth of shallow delaminations with the impact-echo method, high frequency sensing is needed. In these situations, the ordinary microphones cannot meet the frequency requirement. Figure 5.5 shows a PCB measurement microphone. It is a free-field, pre-polarized condenser microphone with a broader frequency range (4 Hz-80 kHz at 2 dB). It has 1/4" diameter, and its small size enables improved space resolution in scanning tests. The sensitivity of the microphone is 4 mV/Pa. The PCB microphone is able to detect significantly

Figure 5.4: The musical microphone.

Figure 5.5: PCB measurement microphone with diameter of 1/4 inch.

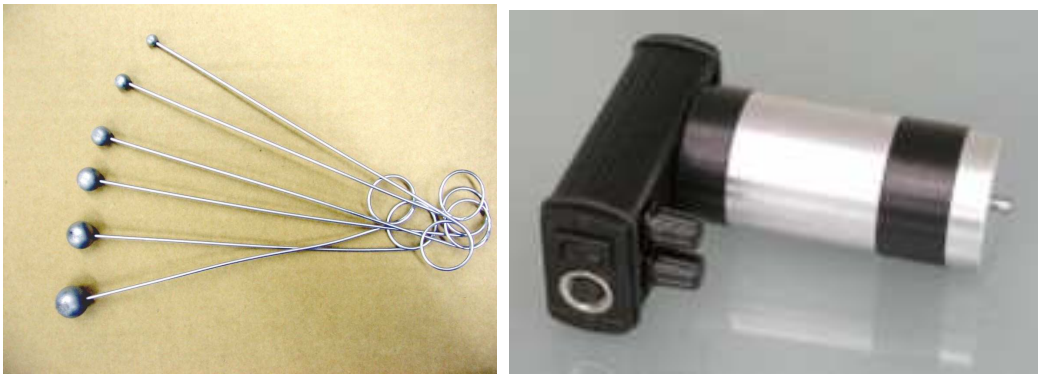

(a) (b)

Figure 5.6: Impactors. (a) Steel ball impactors with diameters from 5mm to 15mm. (b) Electrically controlled impactor.

higher frequencies.

5.1.5 Impact Source

A set of different size of steel balls are used to generate transient waves in concrete, as shown in Fig. 5.6(a). Diameters of the balls range from 5 mm to 15 mm. Smaller balls generate shorter forcing function on the surface and are effective to excite high frequency waves. They also give sharper leading edges at P waves arrival in signals that are used to determine P wave velocity in concrete. Larger balls generate lower frequency waves that have deeper penetration depth in solids.

An electrically-controlled impactor, shown in Fig. 5.6(b), was used to generate repeatable impulse forces when the amplitude information is needed to study the attenuation of leaky surface waves. The impactor operates on the basis of high speed tubular solenoids. The electrical trigger signal can be monitored for consistency and works as the trigger signal by connecting the impactor to an oscilloscope. The impulse energy can be adjusted and the impulse force duration is about 100μs.

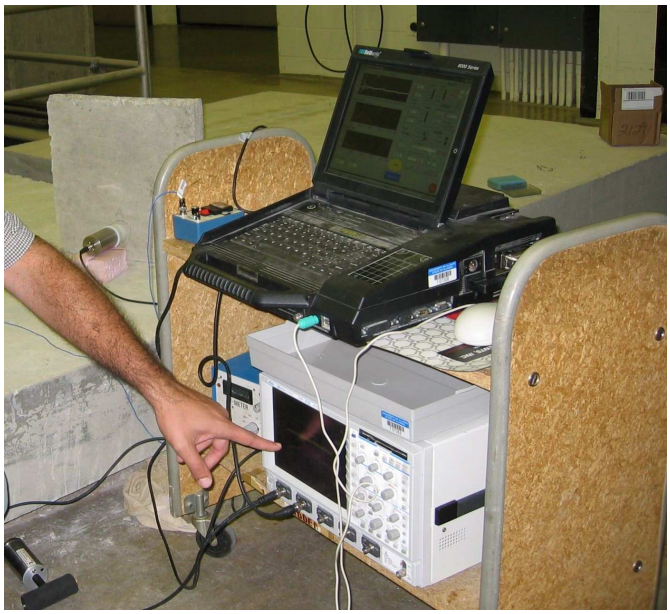

Figure 5.7: Data collecting system. It includes a fieldwork laptop computer and a digital oscilloscope.

5.1.6 Data Acquisition

A 4-channel digital oscilloscope is used for signal digitizing and acquisition. Programs within the Labwindows® environment were developed to control signal acquisition procedure and perform signal processing. Data can be saved for further post-processing using Matlab®. Figure 5.7 shows the data acquisition system that includes a fieldwork laptop computer and a digital oscilloscope.

5.2 Leaky Rayleigh Wave Detection in Concrete

5.2.1 Signal Quality of Air-coupled Sensing

Figure 5.8 shows a typical signal detected by the SM89 microphone from a concrete floor. The sensing element of the microphone was located 0.45 m above the floor. The test was performed in a lab with normal ambient noise level. Assuming the surface wave velocity in the concrete is 2100 m/s, we obtained the arrival times of leaky surface waves and direct acoustic waves from Eq.(5.2): $t_{\mathrm{LR}} = 1.77$ ms and $t_{\mathrm{a}} = 3.19$ ms. The signal shows a clear and sharp peak nearby the leaky Rayleigh wave arrival time. Very good signal-to-noise ratio can be observed. The effect of direct acoustic waves is very small owing to the highly-directional property of microphone.

To compare the signals obtained from contact and non-contact sensors, an accelerometer was placed on the surface directly under the microphone. Properties of the accelerometer are: contact area $= 25mm^2$; mass = 0.7g; nominal voltage acceleration sensitivity $= 1.02$mV/(m/s^2); nominal 10% flat frequency response over $1 \sim 25$ kHz; wax-mounted resonant frequency 75kHz. Figure 5.9 shows the comparison between signals detected by the microphone and the contact accelerometer. It can be seen the microphone signal has better S/N ratio, because accelerometers tend to amplify high frequency noise in the system. In addition, body wave effects in the air-coupled signal are smaller

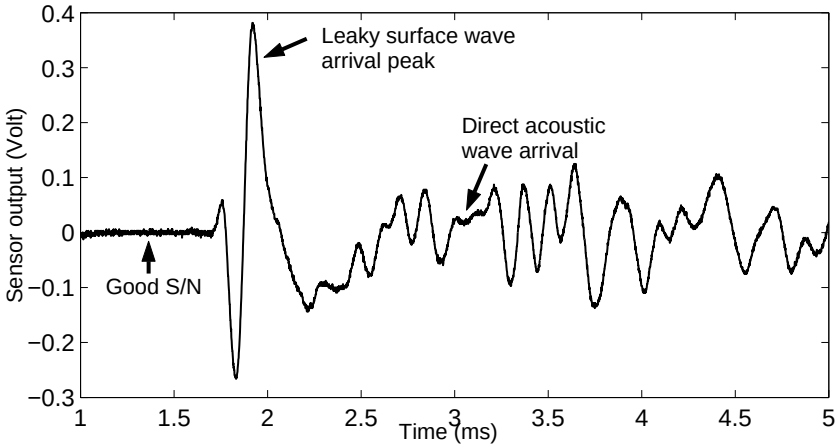

Figure 5.8: A typical signal detected by the SM89 microphone. The sensor position is at $r = 1.0$m, $h = 0.45$m. The amplitude of direct acoustic wave is very small compared to that of leaky surface wave.

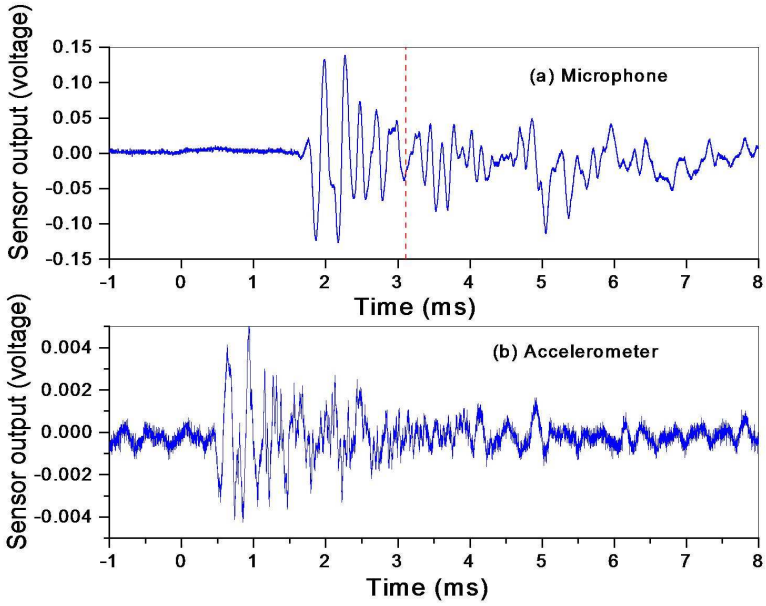

Figure 5.9: Comparison of signals measured by a microphone and an accelerometer. (a) Microphone at $r = 1.0$m, $h = 0.43$m; (b) Accelerometer, $r = 1.0$m. The dashed line in (a) represents expected arrival time of direct acoustic wave.

than in the contact signal. It is also noted that the microphone has much higher sensitivity than the accelerometer. The peak amplitude of the air-coupled signals is 30 times of that of the contact signal.

To further investigate the effectiveness of air-coupled surface wave sensing, tests were performed on a thick concrete wall and a thin concrete floor slab.

5.2.2 Thick Wall Test

The test was performed on a concrete reaction wall for structural testing. The wall has a thickness of 915mm. The P wave velocity obtained from impact-echo test is $C_{\mathrm{P}} = 3810m/s$, and the corresponding R wave velocity is $C_{\mathrm{R}} = 2087m/s$, assuming Poisson's ratio $= 0.22$. To clearly show the wave motion variation trends with increasing distance r, waterfall plots are used to display the signals in cascade form with a step of $\triangle r = 5$ cm and $\triangle r = 10$ cm. Figure 5.10 shows the waterfall plots of signals from the wall test. The distance between the microphone and the wall surface is $h = 43$ cm, and the horizontal source-receiver spacing r ranges from 0 to 210 cm. Within the range of $r = 0 \sim 60$ cm, the spacing increment is $\triangle r = 5$ cm; within $r = 70 \sim 210$ cm, $\triangle r = 10$ cm. The expected arrivals of the direct acoustic waves are also superimposed on the waterfall plots to illustrate the effect of acoustic waves. For small distance r, such as $r < 20$ cm, very good agreement is observed between the wave leading edges and the expected direct acoustic wave arrivals, as shown in Fig. 5.10(a). With increasing of distance r, the acoustic wave arrival curve begins to deviate from the leading edges of signals. For large distance $r = 70$ cm ~ 210 cm, as shown in Fig. 5.10(b), the effect of direct acoustic wave decreases. At the same time, the leaky surface waves arrive first and dominate the waveform.

In Fig. 5.10(b), we notice that the leaky surface wave pulse does not change shape during propagation from $r = 70$cm to $r = 210$ cm, except that the amplitude decreases due to geometrical decay and material attenuation. If the arrival times of points of consistent phase (e.g. peaks) between signals are connected, an approximately straight line is obtained. This phenomenon indicates that the leaky surface waves are non-dispersive in this case. Fig. 5.11 plots the leading edge and $\pm$ peak arrival time of the signals vs. the distance r. In Fig. 5.11(a), the expected acoustic wave arrival time is also superimposed, which matches the leading edge arrivals very well for small r. This result indicates that the signals are dominated by the direct acoustic waves in the near-source region. By linear fitting the positive peak arrivals, the slope gives the leaky surface wave velocity of 2086 m/s, which is very close to the surface wave velocity inferred from the impact-echo test. The fitting line of negative peak arrivals gives $C_{\mathrm{LR}} = 2030$ m/s. The difference is less than 3%, which indicates that no obvious dispersion occurs in the test. According to wave motion theory for a half space, the surface wave dispersion is negligible when the wavelength is smaller than the thickness of a plate or the top layer. In this case, the wavelength of detected surface waves is in a range of 0.2 m to 1.0 m, equal or less than the wall thickness. The thick wall can approximately be regarded as a half-space relative to the leaky surface wave wavelength in this case. Therefore, we expect little or no dispersion.

Fig. 5.12 shows the leaky surface wave peak arrival time vs. the distance r for microphone height $h = 78.5$ cm. Using the same data processing method, the resulting surface wave velocity is 2059 m/s ~ 2095 m/s. The result is similar to the value shown in Fig. 5.11. Therefore, the

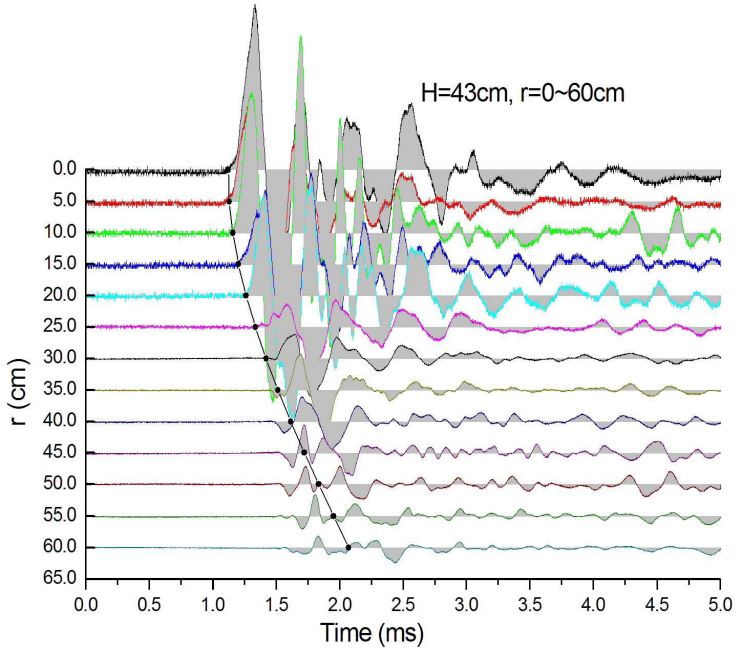

(a)

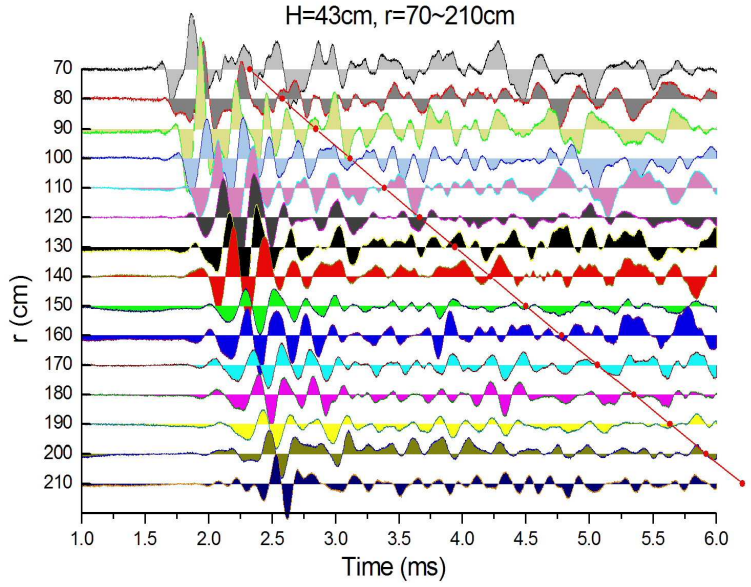

(b)

Figure 5.10: Waterfall plot of signals measured from the concrete wall. The microphone is located at h=43 cm, and (a) $r = 0 \sim 60$ cm; (b) $r = 70 \sim 210$cm. The solid line indicates expected arrival time of direct acoustic waves.

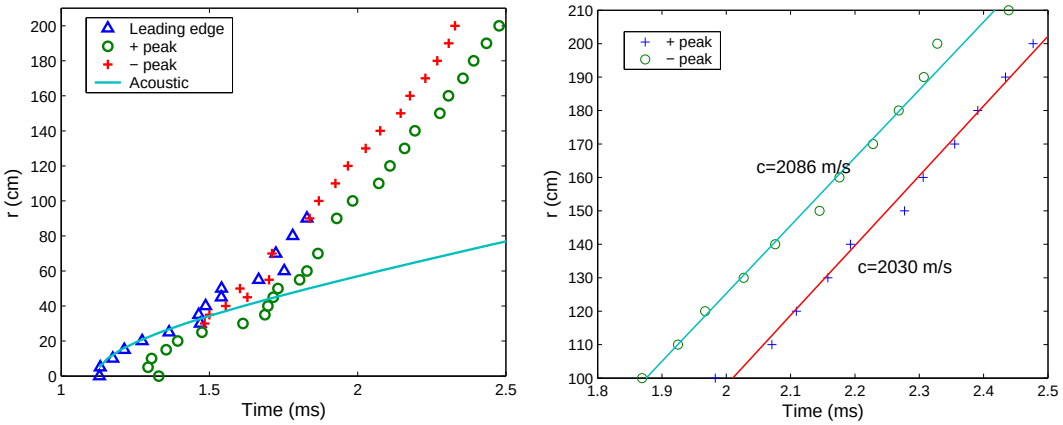

(a) $r = 0 - 2.1$m (b) $r = 1.0 - 2.1$m

Figure 5.11: Leaky surface wave peak arrival time t vs. distance r. The spacing between the microphone and wall surface is 43 cm.

microphone height h has no influence on leaky surface wave velocity measurement. The only effect of large h is the creation of a large shadow zone.

5.2.3 Thin Floor Slab Test

A similar test was performed on a thin floor slab. The thickness of the floor is 95 mm, and the bottom surface of the slab appears partially debonded from the sub-layer. The P wave velocity from impact-echo test is 4000m/s, and the surface wave velocity $C_R = 2191$ m/s, assuming Poisson's ratio $\nu = 0.22$.

The testing setup was the same as that for the previous wall test. The microphone was positioned $h = 78.3$ cm above the floor surface. The waterfall plot of signals is shown in Fig. 5.13. it can be seen that the leaky surface wave pulse becomes wider during propagation. Obvious dispersion of the leaky Rayleigh wave is observed.

The peak arrivals are plotted vs. distance r in Fig. 5.14. Difference can be observed between the results from the floor slab tests and wall tests. First, the surface wave velocities given by the fitting line slope of signal's peaks are much lower than the expected surface wave velocity. Second, the positive peak fitting line is not parallel to the negative peaks fitting line. Therefore they give different apparent group velocities: 1463m/s and 1706m/s. The dispersion is caused by the fact that the thickness of top layer floor slab is less than the Rayleigh wave wavelength. Adler et al. [3] found that the velocity dispersion of surface waves in weakly bonded plates is between the Rayleigh and A0 mode Lamb waves depending on bonding quality. Therefore, the bonding quality of layered concrete slab may be estimated by measuring velocity dispersion curve of leaky Rayleigh waves.

These tests show that the microphone can successfully detect leaky Rayleigh or Lamb waves in concrete slabs with different thicknesses. Further studies will be focused on flaw detection in concrete structures using an air-coupled sensing method.

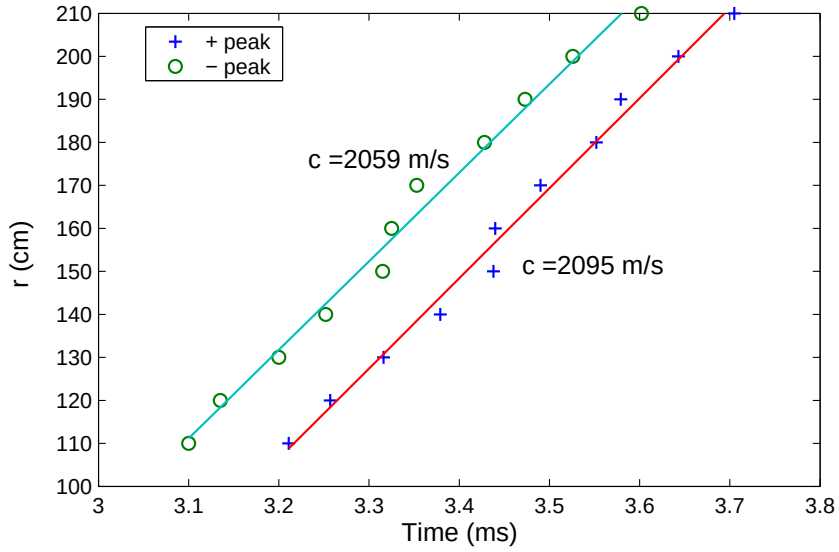

Figure 5.12: Leaky surface wave arrival time t vs. distance r for $h = 78.5$ cm in the thick wall test.

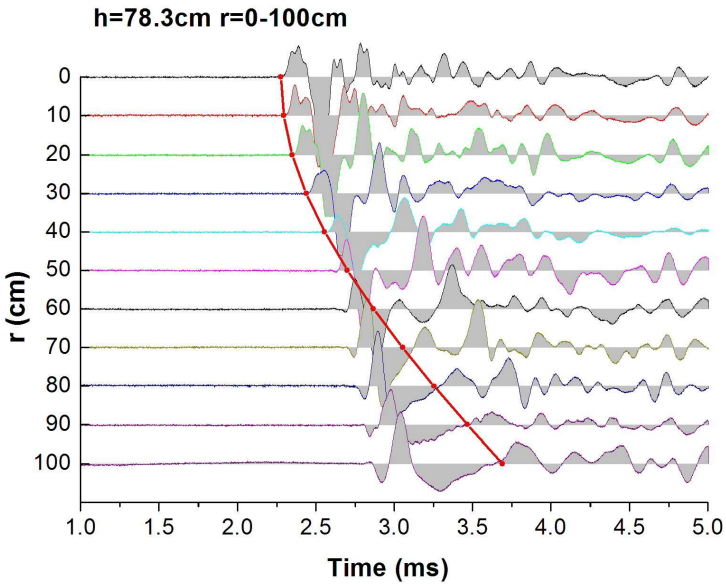

Figure 5.13: Waterfall plot of signals for the thin floor test. The microphone height is $h = 78.3$ cm.

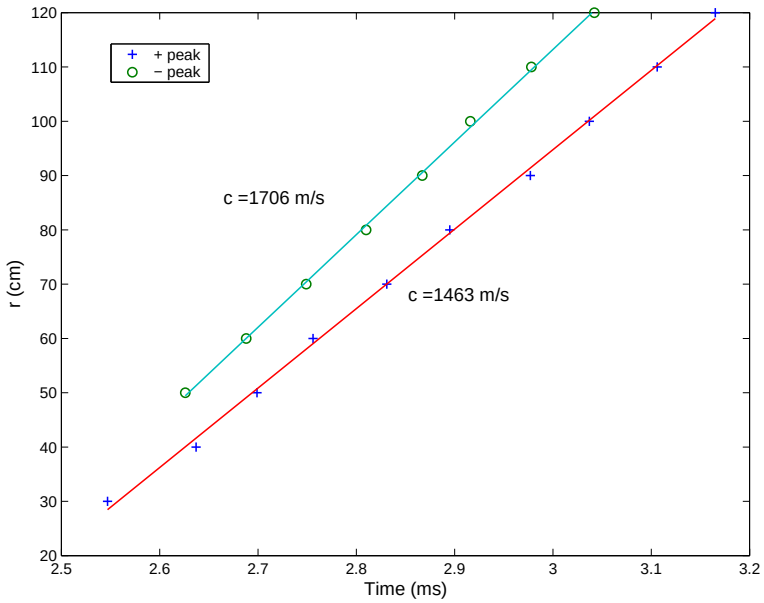

Figure 5.14: Leaky surface wave arrival time t vs. distance r for $h = 78.3$ cm in the thin floor test.

5.3 Results and Conclusions

The signal shown in Fig. 5.8 indicates that the microphone is very effective to detect leaky surface waves that propagate in concrete. The measured signal has high sensitivity and good S/N ratio within the frequency range of interest. Its performance in the preliminary experimental studies also shows the microphone is a good candidate for non-contact concrete inspection.

The leaky Rayleigh waves that propagate in slabs show similar dispersive property to the ordinary Rayleigh waves in the solid-vacuum case. Therefore, air-coupled sensing methods can be used to measure surface wave dispersion curves in layered structures, e.g. pavement, and to further characterized the properties of layered solids.

6 Application of Leaky Surface Wave Detection to NDT of Concrete

The experimental studies in chapter 5 show that the microphone is effective to detect leaky surface waves propagating in concrete. Strong dispersion of surface waves was observed in a thin concrete floor slab. In this chapter, the air-coupled sensing method will be applied to surface wave dispersion curve measurement using the SASW and MASW approaches. Field tests were carried out on a full-scale continuously-reinforced concrete pavement (CRCP). The obtained dispersion curves can be used to characterize the properties of the concrete top layer, and even sub-layers, in pavements. The surface wave energy transmission ratio was used to construct a 2-D image showing locations of cracks in concrete floor.

6.1 Full-Scale Concrete Pavement

The air-coupled SASW and MASW tests were carried out on a full-scale continuously reinforced concrete pavement (CRCP) at the University of Illinois. The pavement was built to study the failure mechanism of CRCP under accelerated traffic conditions [32]. Two strips, each includes five experimental sections, were built. Strip No.1 (sections 1-5) were subjected to simulated traffic loading. Strip No.2 (sections 6 to 10) are reference sections and have not been loaded. The overall thickness of top layer concrete is 250 mm, except sections 4 and 5 of strip No.1 have a top layer thicknesses of 350 mm. The NDT tests were performed on section 5 (350 mm) and section 6 (250 mm).

The layered structure of the pavement is listed in Table 6.1. The Young's modulus of concrete was measured at 28 days, and the measured 28-day compressive strength is 39 MPa. The values of E for subbase and subgrade are given by Kohler through back-calculation from the M-E PDG software model [32].

Table 6.1: The layered structure of pavement.

Layer	Thickness	E (MPa)
Concrete	250mm (350mm for sect. 5)	47.5e3
Asphalt treated base	100 mm	–
Granular subbase	150 mm	290
Subgrade	–	76

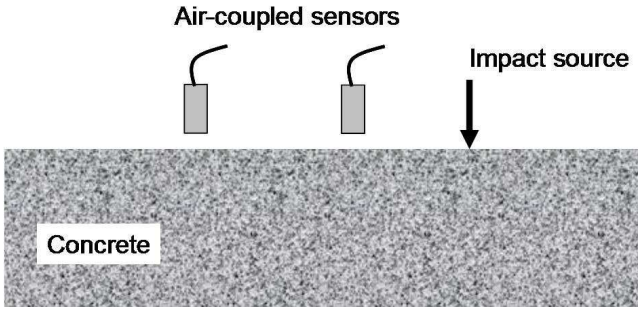

Figure 6.1: Scheme of the air-coupled SASW test.

Figure 6.2: Microphone array frame for the air-coupled SASW test.

6.2 Air-coupled SASW

6.2.1 Testing Setup

The testing scheme of air-coupled SASW test is shown in Fig. 6.1. Two musical microphones shown in Fig. 5.4 were used to sense leaky surface waves in concrete generated by the electrically controlled impactor (Fig. 5.6(b)). An aluminum frame was designed to hold the microphones at desired spacings, as shown in Fig. 6.2. With this frame, the microphone spacing can be set to $10 \sim 60$ cm. The microphone height can be adjusted in a limited range by adjusting the connection between the beam and legs.

6.2.2 Principle of SASW

The SASW test is performed by applying a vertical impact point force on the surface and the transient signals are recorded by two surface receivers placed along a straight line with the impact source. The signals are composed mainly of surface wave contributions over a certain frequency range.

The phase velocity of surface waves is calculated from the phase angle difference between the two signals. Several repeats are made and the the signals are averaged to improve signal-to-noise ratio. The assessment of signal quality is made using the coherence function, which is a measure of the degree by which input and output signals are linearly correlated. A value close to unity is an index of good correlation and hence the recorded signals can be considered genuine and unaffected by ambient noise. To eliminate any asymmetry in the system, the impactor moves to the other side of sensors and the procedure is repeated. The resulting phase velocity is based on the average of velocities from both sides. This procedure not only compensates for any internal phase distortion, it

is also an attempt to mitigate the effects of local discontinuities, lateral inhomogeneities and bedding inclination [25]. The signal processing procedures is summarized here. Typical signals and results are shown in Figs. 6.3 to 6.5.

- Apply Hanning windows to the recorded time signals $y_1(t)$ and $y_2(t)$. The windows are centered at the leaky surface wave pulse arrival.
- Transfer the time domain signals to frequency domain.

$$Y_1(f) = FFT(y_1(t)), Y_2(f) = FFT(y_2(t)). \tag{6.1}$$

- Compute auto-power and cross-power spectra

$$\begin{aligned} G_{11}(f) &= Y_1(f) * \overline{Y_1(f)}, \\ G_{22}(f) &= Y_2(f) * \overline{Y_2(f)}, \\ G_{12}(f) &= Y_1(f) * \overline{Y_2(f)}, \end{aligned} \tag{6.2}$$

  where the top bar denotes the complex conjugate.

- Determine phase angle difference $\triangle\varphi(f)$ between the two signals $y_1(t)$ and $y_2(t)$. $\triangle\varphi(f)$ is calculated from phase angle of the complex-valued cross-power spectra G_{12}.
- Compute the phase velocity of surface waves $C_R(f)$

$$C_R(f) = \frac{2\pi f \triangle x}{\triangle\varphi(f)}, \tag{6.3}$$

  where $\triangle x$ is the receiver spacing.

6.2.3 Field Test Results from the Layered Pavement

The air-coupled SASW test results from section 6 (250 mm thick top layer) of the pavement are shown in Fig. 6.3 to Fig. 6.5. The receiver spacing was 35 cm, and the source-to-receiver spacing was 40 cm. Fig. 6.3 shows the time domain signals recorded by the musical microphones. The arrivals of leaky surface waves and acoustic waves are marked on the figure. With this configuration, the acoustic waves arrive much later than the leaky surface waves, and thus the effect of acoustic waves can be eliminated by windowing process. Figure 6.4 shows the signals after applying Hanning windows that are centered at the leaky surface wave arrival peaks. The Hanning window length was selected based on the impact source duration. The coherence and phase velocity of surface waves are presented in Fig. 6.5. The dispersion curve indicates a surface wave velocity of the top layer pavement of 2350 m/s. It is also noted that the signals have very good coherence within 0-30 kHz range, although the nominal cutoff frequency of the microphones is below 25 kHz. The theoretical A0 mode Lamb wave dispersion curve for the top layer concrete is also plotted. When $10kHz < f < 40kHz$, there is good match between the experimental and theoretical dispersion curves. Because multiple modes of surface waves exist in the layered pavement, while the SASW

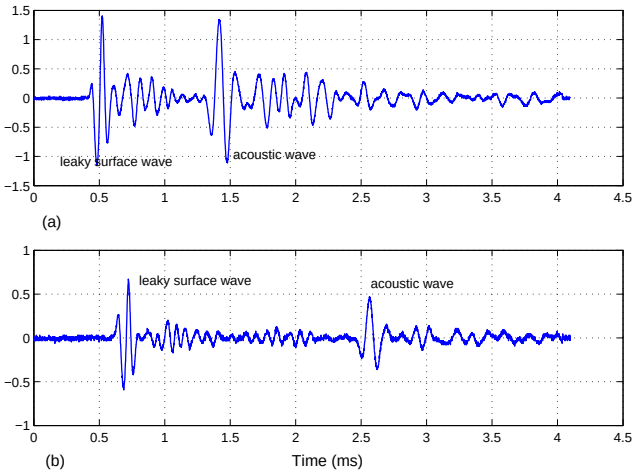

Figure 6.3: Air-coupled time domain signals from section 6 of the pavement. (a) Channel 1, (b) Channel 2.

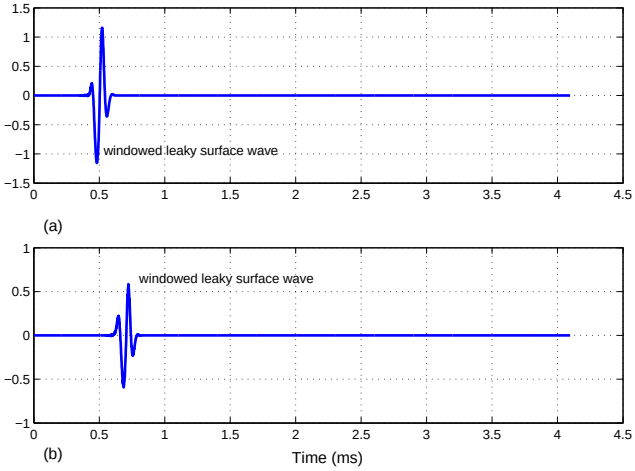

Figure 6.4: Windowed signals containing leaky surface waves. (a) Channel 1, (b) Channel 2.

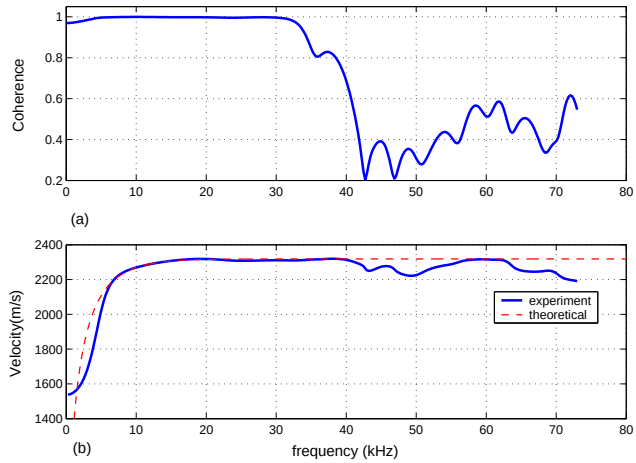

Figure 6.5: Air-coupled SASW test result from section 6. (a) Coherence and (b) Phase velocity of surface waves.

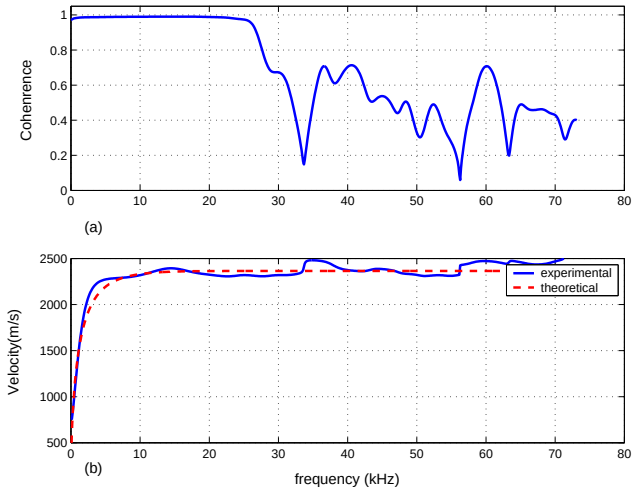

Figure 6.6: SASW test results from section 5 of the pavement with contact sensors. (a) Coherence and (b) Phase velocity of surface waves.

cannot resolve different modes, in the low frequency range, the experimental curve does not match the theoretical curve.

The SASW test with two contact sensors was conducted on section 5 (350 mm thick) of the pavement. Same signal processing was applied. The test results are shown in Fig.6.6, with the theoretical A0 mode dispersion curve superimposed. Similar surface wave dispersion curves are obtained from the air-coupled and contact SASW tests. The phase velocity in Fig. 6.6 (section 5) increases to the top layer surface wave velocity $C_R = 2350$ m/s at a lower frequency than in Fig. 6.5(section 6), because section 5 is thicker than section 6. The comparison of Fig. 6.5 and Fig. 6.6 shows the the air-coupled sensing method can be effectively applied to the SASW tests. In practice, many different receiver spacings and impact sources are needed to construct a compact dispersion curve over a wide frequency range. Air-coupled sensors will greatly improve testing efficiency by eliminating the need of surface coupling.

6.3 Air-coupled MASW

Since only two receivers are used, the SASW test cannot separate different modes of surface waves that propagate in a layered structure. The dispersion curve actually measures a superposition of all propagating wave modes at the specific receiver locations. This superposed effect, often termed apparent phase velocity or pseudo-phase velocity, changes with receiver spacings and thus the evaluation of data needs to consider the position of receivers [59]. The multi-channel analysis of surface waves (MASW) enables separation of different modes and overcomes limitations in the SASW tests due to higher wave modes.

6.3.1 Testing Setup

A true multi-channel survey requires an expensive and bulky multichannel recording device and many receivers deployed simultaneously over a small area. Ryden et al. [56] proposed the MSOR

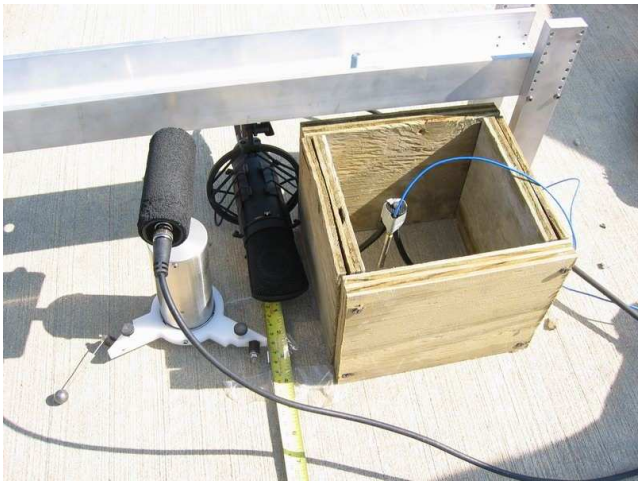

Figure 6.7: The air-coupled MASW testing setup on the CRCP pavement.

method, where only one receiver and a single-channel recording device are used, while the impact source moves consecutively along a line. Ryden showed the MSOR setup gives the same results as the true MASW method provided two conditions are met: consistent triggering and lateral homogeneity of the test site.

The MSOR setup was used in this research. Two sets of microphones (the musical and the PCB microphone) and a contact sensor were used to record signals, as shown in Fig. 6.7. The source-receiver spacing ranges from 20 cm to 210 cm at 5 cm steps. Therefore one whole data set includes 39 signals. The electrically-controlled impactor provides consistent input force and trigger signals.

A LabWindows program was developed to record signals from four channels simultaneously, as shown in Fig. 6.8. This program controls most functions of the oscilloscope, and save acquired signals into the computer.

6.3.2 Field Tests from Layered Pavements

Figure 6.9 presents the raw time domain signals in multi-channel format, recorded by the contact sensor and the musical microphone respectively. In Fig. 6.9(b), the wave fronts of leaky surface waves and acoustic waves are clearly identified. For MASW analysis, a rectangular window is applied to the raw air-coupled signals to eliminate the acoustic wave effect. The windowed signals are then transformed to frequency-phase velocity domain using the MASW transformation method [44, 59]. Figure 6.10 shows the frequency-phase velocity images corresponding to the signals in Fig. 6.9. It can be seen that the contact sensor and the microphone give similar results. The low frequency range of the microphone results have slightly lower quality owing to effects of acoustic waves and windowing. The windowed signals have shorter effective length, and thus contain less useful information than the signals recorded by the contact sensor, which are not affected by the acoustic waves. The acoustic wave effect can be reduced by applying sound insulation to the air-coupled sensor.

The high amplitude of the frequency-phase velocity spectrum image corresponds to surface wave modes with high excitability. The A0 mode Lamb wave dispersion curve for a free slab, which cor-

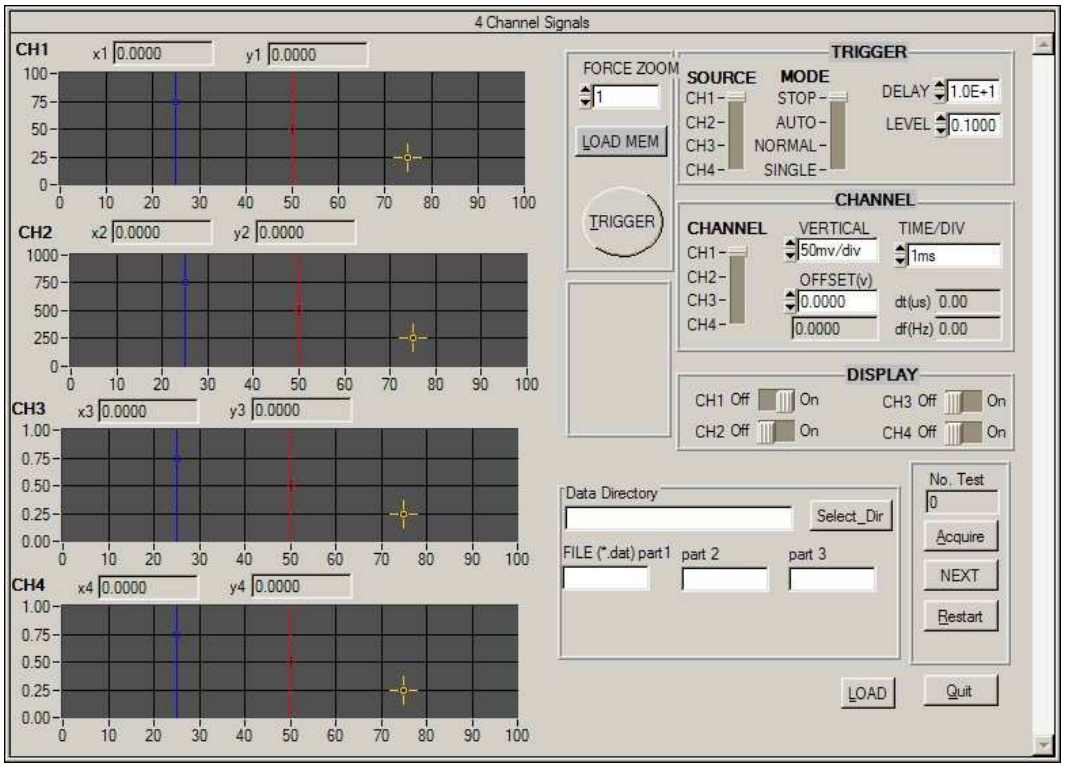

Figure 6.8: The user interface for the 4-channel data acquisition program.

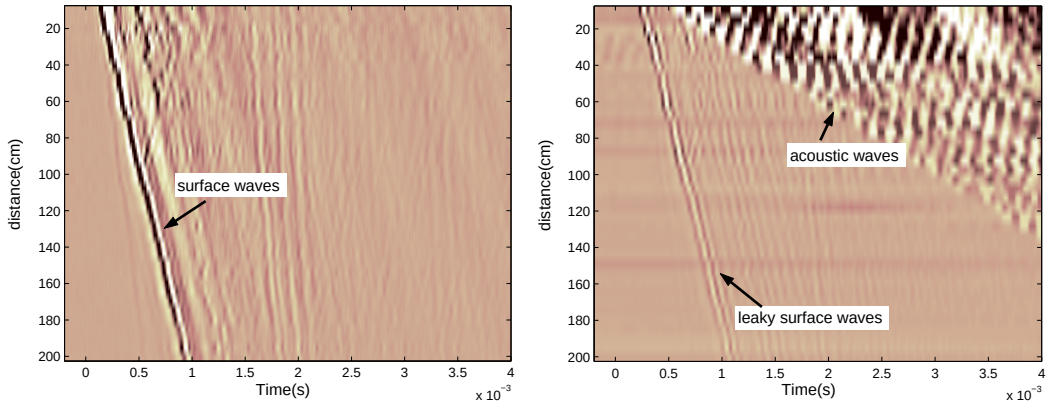

(a) (b)

Figure 6.9: Multi-channel time domain signals recorded on section 5 of the CRCP pavement. (a) with the contact sensor; (b) with the musical microphone.

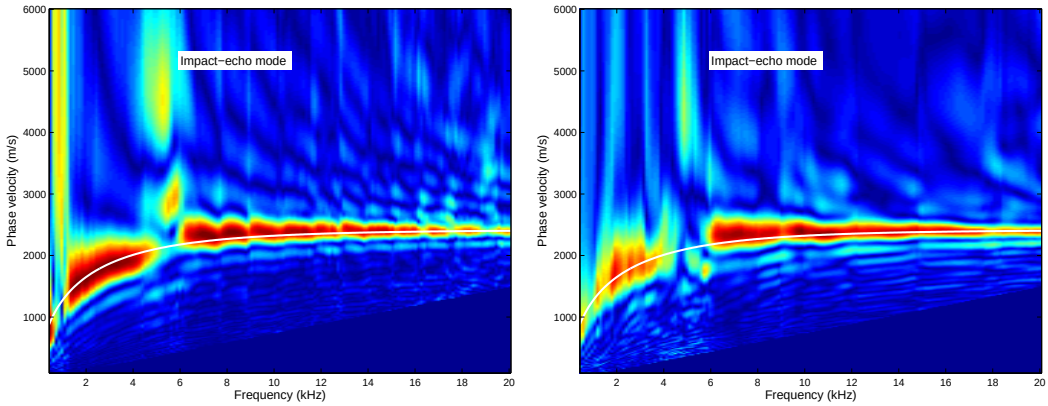

(a) (b)

Figure 6.10: Frequency-phase velocity image of the time domain signals in Fig. 6.9. (a) with the contact sensor; (b) with the musical microphone. The theoretical A0 mode Lamb wave dispersion curve is superimposed as the white curve.

responds to the top layer, is superimposed on the spectrum images in Fig. 6.10. Material properties of the top layer concrete pavement are: shear wave velocity $C_S = 2600$ m/s, Poisson's ratio $\nu = 0.3$ and thickness of 350 mm. There is a good match between the Lamb-wave dispersion curve and the measured data. This observation agrees with Ryden's findings [58]: Lamb-wave dispersion curves for a free plate can accurately represent that of a real pavement if large stiffness contrast exists between the top layer and the underlying half-space.

Testing efficiency can be improved by adopting a compromise between MASW and MSOR in testing setup. For example, by using n air-coupled sensors in the n-channel set up, the work load of MSOR will be reduced to $1/n$, whereas the work load of installing n air-coupled sensors will not increase much since no surface coupling is needed.

6.3.3 Feasibility of Air-Coupled Impact-Echo

In addition to the fundamental mode of Lamb waves, a resonant mode around 5.4kHz is also excited, which is marked as the "impact-echo mode" in the images. The impact-echo mode can be clearly identified in both the contact sensor and microphone signal images.

The conventional theory of impact-echo is based on multiple P-wave reflections between the top and bottom surfaces, as shown in Fig. 3.6. However, Gibson's analysis [27] links the the impact-echo mode to the zero-group-velocity frequency of S1 Lamb wave mode. At this frequency, the S1 mode has the highest excitability in response to a point source at the surface. The Lamb wave theory provides a solid theoretical basis for the empirically established "correction factor" ($\beta = 0.96$) used in impact-echo data analysis.

Due to the large impedance difference between air and concrete, it is very difficult to sense leaky P waves from concrete structures. Thus according to the conventional impact-echo theory based on multiple P wave reflections, air-coupled sensors would not be able to be used in the impact-echo test. However, the new theory shows that the impact-echo mode is a resonant mode, where large amplitude oscillation is excited. The high energy contained in the resonant mode enables the application of air-coupled sensing. Therefore, the Lamb wave theory also suggests the feasibility of

Figure 6.11: Test set-up showing microphones and the rack mount. The microphones in the photo have a fixed horizontal spacing of 40 cm.

using air-coupled sensors to the impact-echo test.

6.4 2-D Imaging of a Cracked Concrete Slab

Air-coupled sensing not only improves test efficiency by eliminating the need for surface coupling, it also provides more useful information because of improved signal consistency. In civil engineering, most stress wave-based NDT techniques use wave velocity information only. In fact, wave attenuation is more sensitive to defects in concrete, but the inconsistent surface coupling prevents its application. With the non-contact advantage of air-coupled sensing, we are able to use amplitude information to study the influence of defects on wave attenuation.

To investigate the effect of defects on the attenuation of leaky Rayleigh waves, a 2-D scan test was performed on a concrete floor that contains surface-opening cracks. The experiments were carried out at the Newmark Laboratory at the University of Illinois at Urbana.

6.4.1 Testing Setup

The electrically-controlled impactor shown in Fig. 5.6(b) was used to generate repeatable point impulse forces. Experiments showed that the generated forces are consistent in amplitude and duration. The electrical output signal can be monitored for consistency and works as the trigger signal. The impulse energy can be adjusted and the impulse force duration is about 100 μs. The typical signal frequency range generated by the impactor is $0 \sim 25$ kHz.

Three Shure SM89 microphone were used to detect leaky waves from the concrete slab simultaneously. After amplification, the signals of microphones were calibrated to a consistent acoustic source. In this test, an airborne ultrasound transmitter was used as the calibration source. The microphones were mounted in line using a mounting system that allows accurate placement of the sensors with regard to sensor separation and height from the test surface. A photo of the multiple-sensor frame in use is shown in Fig. 6.11. In this case three microphones were used with 40 cm spacing between each other and 67 cm height from the test surface. The impact source is applied at a surface point along the line defined by the three aligned microphones, and the spacing between the source and the first microphone is 80 cm. The propagating leaky waves generated by the source are detected by the microphones and are sent to separate channels of a digital oscilloscope. Each transient signal is collected for duration of 5 ms, and digitized with 4096 points at a sampling resolution 1.2 μs. The

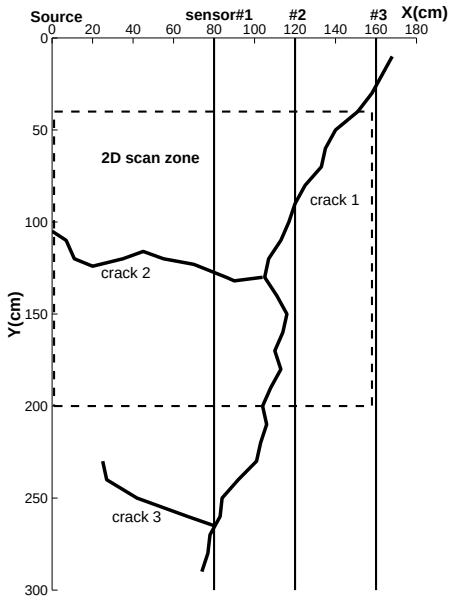

Figure 6.12: Concrete floor slab with surface-opening cracks. Impact point source and three microphone locations are shown for Y scan ($y = 0 \sim 290$cm). 2-D scan zone (dashed line) is in the range of$x = 0 \sim 160$cm and $y = 40 \sim 200$cm.

digitized data are transferred to a computer using the GPIB interface system for storage and further analysis.

An existing concrete floor slab was identified for testing. A map of the floor slab specimen, showing crack locations, microphone and impact positions and scan lines is shown in Fig. 6.12. This slab has some regions that are apparently defect-free and other regions that contain individual tightly-closed surface cracks. The thickness of the slab varies between 180 mm to 210 mm, as determined by the impact-echo method. The surface wave velocity determined by SASW method is 2250 m/s. The surface of the concrete is smooth. No extra treatment or preparation was applied to the surface, and the leaky wave tests were carried out in ambient acoustic noise conditions. Three in-line microphones were used simultaneously to collect data from a single impact event. Two 1-D scan tests were performed on the floor. First the microphone mounting frame was aligned along x direction and moved in y direction, and a series of 30 parallel linear data sets were collected in the region of $x = 0 \sim 160$ cm and $y = 0 \sim 290$ cm, with 10 cm spacing in y direction between each data set. Because the scanning line is along y direction, this scan pattern is defined as y-scan. For each data set, the impactor trigger signal and three leaky wave signals were collected. This scan configuration provides paths with no cracking between microphones #1 and #3 ($y = 0 \sim 30$cm), cracking only between #1 and #2 ($y = 140 \sim 220$ cm), cracking only between #2 and #3 ($y = 40 \sim 80$ cm) and cracking among several regions. The x-scan test was performed in the region of $x = 0 \sim 160$ cm and $y = 40 \sim 200$ cm. The microphone mounting frame was aligned along y direction and moved in x direction. The impact point and microphone locations are along $y = 40$ cm, 120 cm, 160 cm and 200 cm, respectively.

6.4.2 Data Processing and Imaging

The leaky surface wave velocities C_{LR} and attenuations were used to construct 1-D scanning images. To construct a 2-D scan image, the normalized x-scan and y-scan parameters at the same position are summed to give a normalized 2-D parameter. Along each scan line, the leaky wave velocity C_{LR} is determined from the delay in the arrival time of the first large positive peak in the leaky wave signal between two adjacent microphone locations with known separation (40 cm). For the region of $x = 0 - 80$ cm (y-scan case), C_{LR} is determined from the initiation of leaky surface waves measured by microphone #1. Therefore, for the y-scan configuration, there are $3 * 30 = 90$ velocity data obtained in total. The obtained velocities were then normalized with respect to the crack-free region leaky surface wave velocities $C_{\mathrm{LR}} = 2250$ m/s. The normalized velocities were used to construct a leaky surface wave velocity scan image.

The attenuation was calculated based on the leaky surface wave pulse energy ratio between the leaky wave signals detected by two adjacent microphones. The detailed flow chart that illustrates energy ratio calculation is shown in Fig. 6.13. The energy ratio is used instead of peak amplitude ratio because the pulse energy is less affected by dispersion, which distorts waveforms during wave propagation and makes amplitude measurement unreliable. For each scan line, a Hanning window is first applied to the raw signals to extract leaky surface wave signals, where the length of Hanning window is determined by the impact force duration. The root-mean-square (RMS) of each windowed signal is then calculated and denoted as A_1, A_2 and A_3, where the subscript $1 \sim 3$ represents microphone $\#1 \sim \#3$. The definition of RMS is

$$A = RMS = \sqrt{\frac{1}{n}\sum_{i=1}^{n} x_i^2} \tag{6.4}$$

where n is number of points in the digitized signal x_i. The attenuation of leaky surface waves can be expressed as the energy ratio between adjacent microphones, i.e., $R_1 = A_2/A_1$ and $R_2 = A_3/A_2$. Larger energy ratio indicates higher transmission and less attenuation. R_1 and R_2 are further normalized with respect to the energy ratio obtained in crack free regions. For the region between the impact point and microphone #1, because no energy ratio can be obtained, A_1 is normalized with respect to A_{1m} obtained from the crack free region.

6.4.3 Results and Discussion

1-D and 2-D scan imaging

Figure 6.14 shows the y-scan leaky surface wave velocity and energy ratio images. Dark regions indicate low velocity or transmission. The actual crack positions are also superimposed on the images for comparison. It can be seen that the velocity image has low contrast, which indicates that leaky surface wave velocity C_{LR} is relatively insensitive to existence of cracks. In addition, the low velocity regions do not match the actual crack position well. On the contrary, the energy ratio image shown in Fig. 6.14(b) has clear and sharp contrast, and the dark regions agree well with the actual crack positions. Therefore, we can reach the conclusion that leaky surface wave energy ratio is a more sensitive criterion for crack indication than velocity. This result can be explained by surface

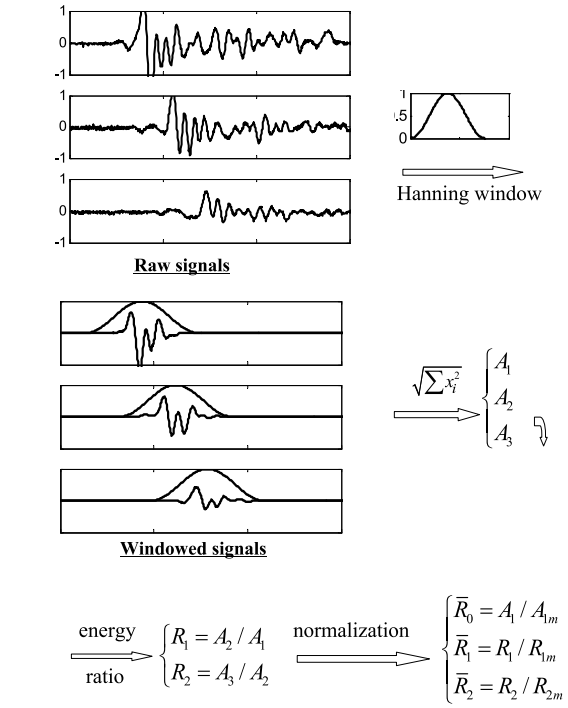

Figure 6.13: Flow chart for leaky surface wave energy ratio calculation. $A_1 \sim A_3$ represent the RMS of each windowed signal detected by microphones $\#1 \sim \#3$. A_{1m}, R_{1m} and R_{2m} are the RMS and energy ratios obtained from crack-free regions. The normalized values are used for image construction.

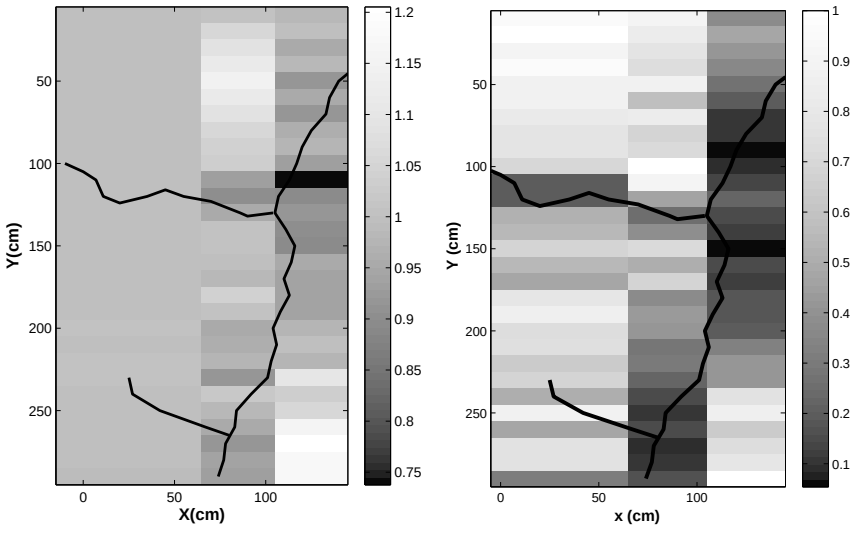

(a) (b)

Figure 6.14: Leaky surface wave y-scan images. (a) velocity; (b) energy ratio. Dark regions represent low velocity or transmission. The actual crack positions are superimposed on the images for comparison.

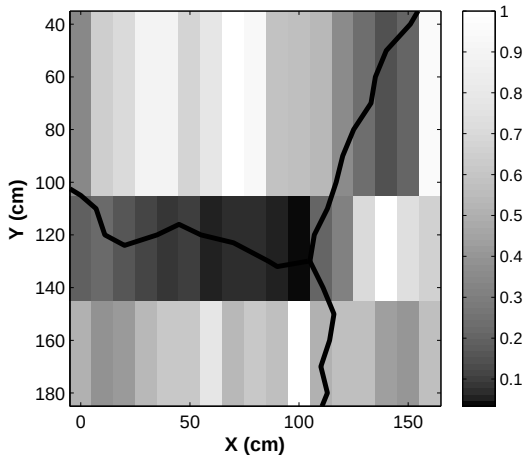

Figure 6.15: Leaky surface wave x-scan energy ratio image. The actual crack positions are superimposed on the image for comparison.

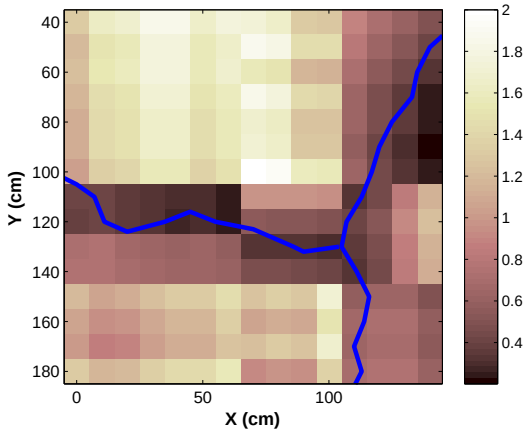

Figure 6.16: Leaky surface wave 2-D scan energy ratio image. The actual crack positions are superimposed on the image for comparison.

wave propagation theory. In these tests, a relatively low frequency (5 kHz$\sim$$25$ kHz) impact source is used, which excites leaky surface waves with wavelength around $10 \sim 50$ cm. Even for deep cracks that penetrate through the floor slab (20 cm), leaky surface waves can still propagate through the crack via sub-layers, but with energy loss. Therefore, leaky surface wave velocity is not as affected by existence of cracks as energy ratio.

The x-scan leaky surface wave energy ratio image is shown in Fig. 6.15. It can be seen that crack #2 has been clearly identified by low energy ratios, because the wave propagation direction is perpendicular to the crack. In region of $y = 140 \sim 180$ cm, crack #1 is nearly parallel to wave propagation direction, so it is difficult to identify the crack in this image. However, the accuracy can be improved by combining two images obtained from the different scanning directions. By summing the normalized x-scan and y-scan parameters at the same position, a 2-D scan image can be constructed, as shown in Fig. 6.16. The 2-D image clearly shows locations of all cracks as regions of low transmission.

Shadow Zone Effect

The shadow zone complicates data analysis, since the image should be corrected for shadow zone size. For 2-D imaging, it should be corrected in both directions. In this test, microphone hight $h = 76$ cm and the leaky angle $\theta = 8.8°$, which gives a shadow zone size of 12 cm. Because the leaky angle is relatively stable, which varies around 8 to 10 degrees for normal concrete, the only way to minimize shadow zone size is to reduce microphone height h. Smaller h also helps separate leaky surface waves from acoustic waves, which enables small source-to-sensor spacing and improves the image resolution. The sensing element of the microphone used in this test is 36 cm from the tip; therefore the minimum h we can obtain with this type of microphone is 36 cm. To reduce h, smaller microphones should be used, e.g. the musical microphone in Fig. 5.4 or the PCB microphone in Fig. 5.5.

This preliminary study shows the potential to use leaky surface waves to detect and image surface-opening cracks. Further theoretical and experimental research is needed to extend this technique to subsurface defect detection.

6.5 Results and Conclusions

The experimental studies presented in this chapter investigate the application of air-coupled sensors to conventional surface wave NDT of concrete. Field tests indicate that the air-coupled sensors are able to replace contact sensors in the SASW and MASW tests, and test efficiency can be greatly improved by eliminating the need of surface coupling. The accuracy of test results is comparable to that with contact sensors.

The non-contact advantage of air-coupled sensing enables us to study the influence of defects on wave attenuation. The preliminary surface-breaking crack detection test shows leaky surface waves are sensitive to the existence of cracks when waves propagate across cracks. The crack positions are clearly located by the 2-D scanning test. The energy ratio criteria is more sensitive than the surface wave velocity to the existence of cracks.

7 Air-coupled Impact-Echo

7.1 Introduction

The use of acoustic sensors to detect delaminations in concrete can be dated back to 1973, when the Texas Transportation Institute developed an automated delamination detection device called Delamatec© [39, 40]. The essential components of Delamatect© consist of automated tappers, a strip chart recorder, and acoustic receivers. For good concrete, the obtained time domain record is flat and very close to zero but becomes irregular when indicating a delamination. However, application of the Delamtect© has been limited due to poor accuracy.

Impact-echo has become one of the most commonly used NDT methods for concrete defect detection since it was first proposed in the 1980s [13]. It can be used to determine the location and extent of flaws such as cracks, delaminations, voids, honeycombing, and debonding in concrete structures. Impact-echo is especially effective in locating and estimating the depth of delaminations [60], which are the most serious problem affecting the service life of reinforced concrete bridge decks and parking garage slabs.

Impact-echo is an elastic wave-based NDT technique, where a steel ball applies an impact force on the surface and generates elastic waves in the concrete. The transient surface motion is detected by a sensor, and the time domain signal transformed to the frequency domain. The slab thickness, or depth of defects H, is related to P-wave velocity C_P and peak frequency f of frequency spectrum by $H = \beta C_P/2f$, where β is approximately 0.96 for plate-like structures.

Like many other elastic wave based NDT methods, impact-echo is a point inspection method. Therefore, it can be very time consuming and labor intensive to test large structures or pavements. One solution to improve test efficiency is to develop a contact-less impact-echo scanning method. By eliminating the contact between sensors and concrete surfaces, an automated impact-echo scanning system is enabled. This idea is similar to Delamatec© to some degree, but the signals of air-coupled impact-echo are analyzed in the frequency domain instead of the time domain. Furthermore, the development in hardware and computer imaging techniques enables rapid scanning and imaging of concrete structures.

In chapter 6, it has been shown that the impact-echo mode can be detected by air-coupled sensors in the MASW test. Therefore, air-coupled sensors were applied in this study for non-contact impact-echo tests.

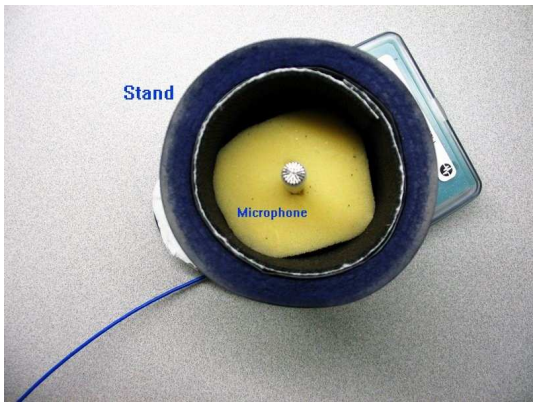

Figure 7.1: Microphone with insulation stand.

7.2 Testing Setup and Equipment

7.2.1 Testing Setup

The effect of direct acoustic waves is not a big concern in air-coupled surface wave tests, because the acoustic waves can be isolated by increasing the source-receiver spacing r. In Fig. 6.9(b), the leaky surface waves are completely separated from the acoustic waves when $r \geq 20$ cm. The leaky surface wave pulse can be extracted by applying a Hanning window. However in the impact-echo test the whole signal is needed for analysis since it takes a longer time to set up the impact-echo mode (similar to resonant tests). To obtain reliable and consistent results with air-coupled impact-echo, the direct acoustic waves must be suppressed. Solutions are sought from two aspects:sensors and impactors. Good insulation should reduce the energy of acoustic waves detected by the sensor. The impactor must excite the impact-echo modes in concrete without generating excessive acoustic noise.

7.2.2 Air-Coupled Sensors

Two types of microphones were used in the air-coupled impact-echo tests: the musical microphone and the PCB measurement microphone. The PCB measurement microphone has small size (1/4" diameter) and broad frequency range (4-80 kHz at $\pm$2dB). The PCB microphone is able to detect higher frequencies corresponding to thicknesses of shallow delaminations. Its small size enables improved spatial resolution in impact-echo scanning tests.

A special microphone stand was designed to support the PCB microphone; it provides sound insulation to shield ambient noise and direct acoustic waves. Figure 7.1 shows the PCB microphone and the insulation stand. The stand is made of a layer of rubber, an aluminum shell and a foam layer. The foam and aluminum work together to absorb and reflect most ambient noise and direct acoustic waves, while the inner rubber layer absorbs the leaky waves from the concrete surface and prevents the waves from forming resonance within the stand. The microphone is inserted into the stand through a hole on the bottom. The microphone height can be easily adjusted.

Experimental studies were carried out to investigate the sound insulating efficiency of the stand. Figure 7.2 shows the testing scheme. The sensor and stand were placed on slab No.1, and a point

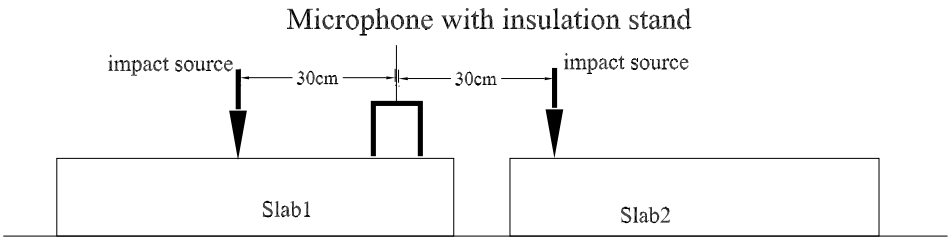

Figure 7.2: Scheme for testing the insulation efficiency of the microphone stand.

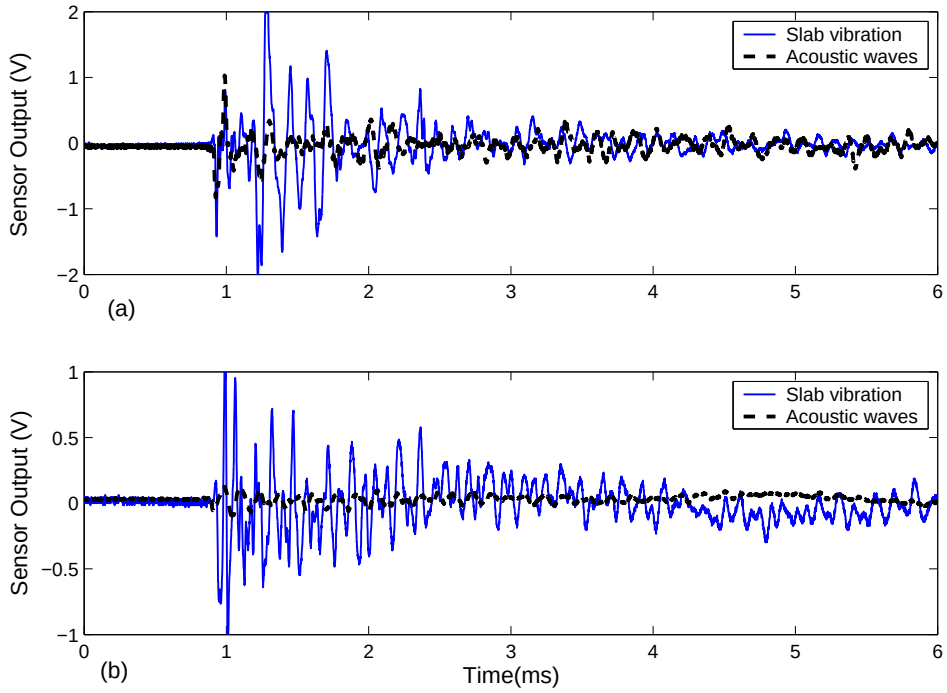

Figure 7.3: Signals showing the insulating effect of the stand. (a) Slab vibration and acoustic wave signals recorded by the microphone without insulation. (b) Signal recorded by the microphone with insulation.

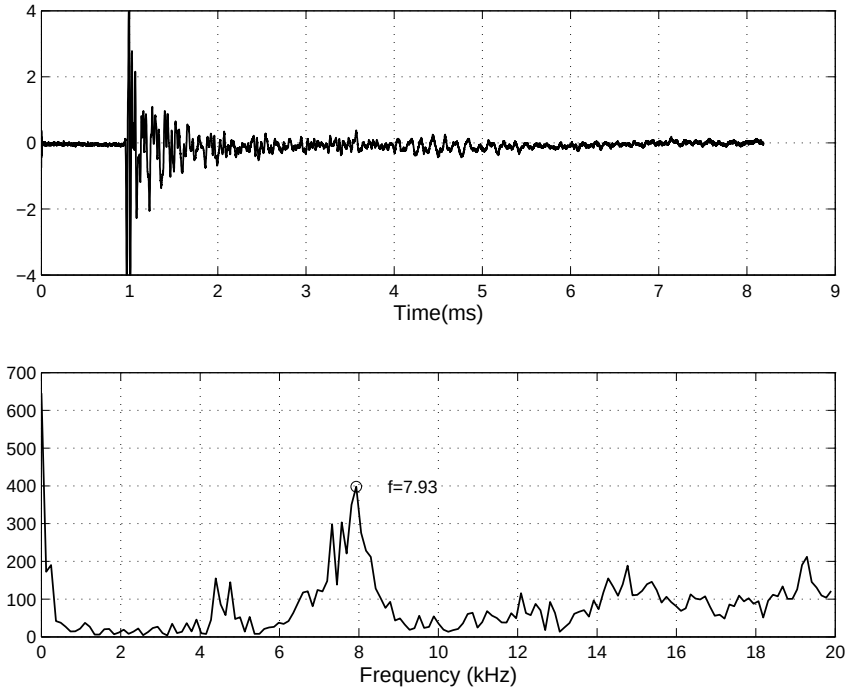

Figure 7.4: A typical signal from an air-coupled impact-echo test. (a) Time domain signal. (b) Amplitude spectrum. The peak frequency at 7.93kHz is marked.

impact force was applied on slab No.1 and No.2, respectively, with the same source-to-receiver spacing. When the impact was applied to slab No.1, the microphone should sense the slab vibration and the direct acoustic waves. When the impact was applied to slab No.2, only direct acoustic waves should be detected. The signals are shown in Fig. 7.3 for two testing configurations: with and without the microphone insulation stand. The source-to-receiver spacing is 30 cm. It can be seen that the amplitude of direct acoustic waves is about 50% of that of slab vibration if there is no sound insulation between the microphone and the source. With the insulation stand, the acoustic wave effect is reduced to 10%. Therefore, this microphone insulation design can effectively reduce the influence of ambient noise and the direct acoustic waves.

Experiments indicate that the microphone height affects the test results. There is an optimal distance h between the sensor and the testing surface. The optimal h is around 2.5cm$\sim$3.0cm. When the sensor is too close to or too far from the testing surface, the peak frequency will shift from the correct impact-echo frequency.

Figure 7.4 shows a typical signal recorded by the PCB microphone from a concrete slab. The frequency amplitude spectrum shows a clear and sharp peak at frequency $f = 7.93$ kHz, which corresponds to the full-thickness impact-echo frequency. Similar results are obtained with a contact sensor on the same slab.

7.2.3 Impactors

A set of spring-loaded steel balls, as shown in Fig. 5.6(a), are used for the air-coupled impact-echo test. Similar to the contact impact-echo test, selection of proper ball size is critical for detecting

defects at different depths. The electrically-controlled impactor in Fig. 5.6(b) generates too much acoustic noise from the unit itself, and is not suitable for air-coupled impact-echo application.

7.3 Concrete Specimens Containing Artificial Defects

Two concrete slabs were cast. The slabs are nominally 0.25m thick with lateral dimensions 1.5 m by 2.0 m. The 28-day compressive strength of the concrete is 42.3 MPa. P-wave velocity of the concrete, determined by UPV measurement, is 4100 m/s to 4200 m/s, which results in the full-thickness impact-echo frequency of 7.81 kHz ~ 8.06 kHz.

Slab No.1 contains two continuous embedded ducts: one plastic and one metal. Each duct is divided into three sections: fully-grouted, partially-grouted and ungrouted. The voids in the partially-grouted and ungrouted regions are simulated by filling with foam. The diameter of the ducts is 70 mm, and the centerlines of the ducts are 125 mm below the surface. The same specimen also contains a surface-opening notch that has a linearly increasing depth, varying from 10 mm to 150 mm across the width of the slab. The notch was generated by inserting two greased metal sheets before casting concrete. The plan view and cross-section of the slab are shown in Fig. 7.5. The metal sheets should have been removed from the concrete after initial setting to form a surface-opening notch in the slab. Unfortunately, only 1/3 the length of the sheets in the shallow crack region was successfully removed from the slab, and the other part remains in the concrete. The problem was probably caused by insufficient greasing of the metal. But a notch is still formed by the gap between the two metal sheets.

Slab No.2 contains artificial delaminations and voids with different sizes and depths. The plan view and cross-section of the slab are shown in Fig. 7.6. Since the loading capacity of the slab is significantly reduced by the artificial defects, the slabs are reinforced in two dimensions and at two layers. The top layer of rebars are supported by five steel seats. The concrete cover thickness is 60 mm. Wire mesh (150×150 mm) were placed above each rebar layer. Artificial delaminations were simulated by embedding six double plastic sheets. Three double sheets are located 60 mm below the surface (top sheet), and three are 200 mm below the top surface (bottom sheet). The actual position of plastic sheets were measured in the slab form before casting concrete. The measured depths of defects are shown in Table 7.1. Internal voids were simulated by embedding 300 mm and 100 mm diameter soft foam blocks. The plastic sheets and foam blocks were secured to the wire mesh with tie wire. The picture in Fig. 7.7 shows the location of defects and rebars layout.

7.4 Effect of Source-to-Receiver Spacing on Test Result

The effect of source-to-receiver spacing on air-coupled impact-echo was investigated. The results are shown in Figs. 7.8 and 7.9, where both the musical microphone and the PCB microphone were investigated. The microphones were positioned 3 cm above a 250 mm thick concrete slab, and the source-receiver spacing x varies from 3 cm to 30 cm. The PCB microphone was placed in the insulation stand. There was no sound insulation for the musical microphone. The full thickness impact-echo frequency lies between 7.8 kHz and 8.06 kHz, depending on the impact locations.

In Fig. 7.9, the normalized amplitude vs. x plot indicates if the peak frequency is the dominant

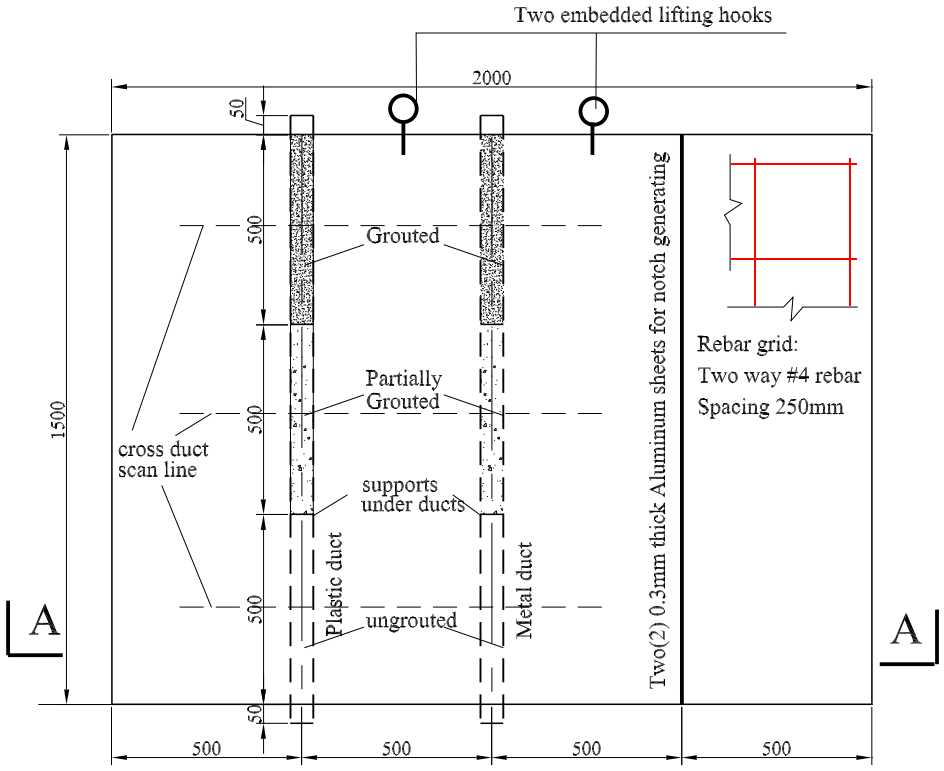

(a) Plan View of Slab No.1

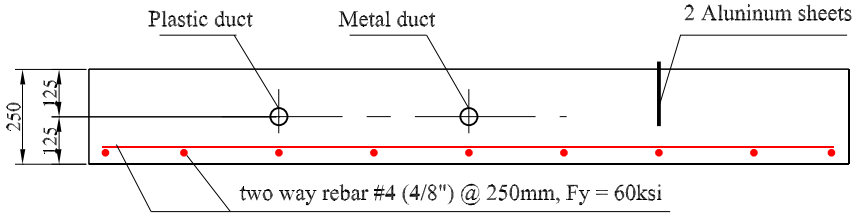

(b) Section A-A of Slab No.1

Spray oil on both sides of the aluminum sheets before casting concrete

Figure 7.5: Slab No.1 containing ducts and a notch. (a) Plan view and (b) cross-section. Location of defects are marked.

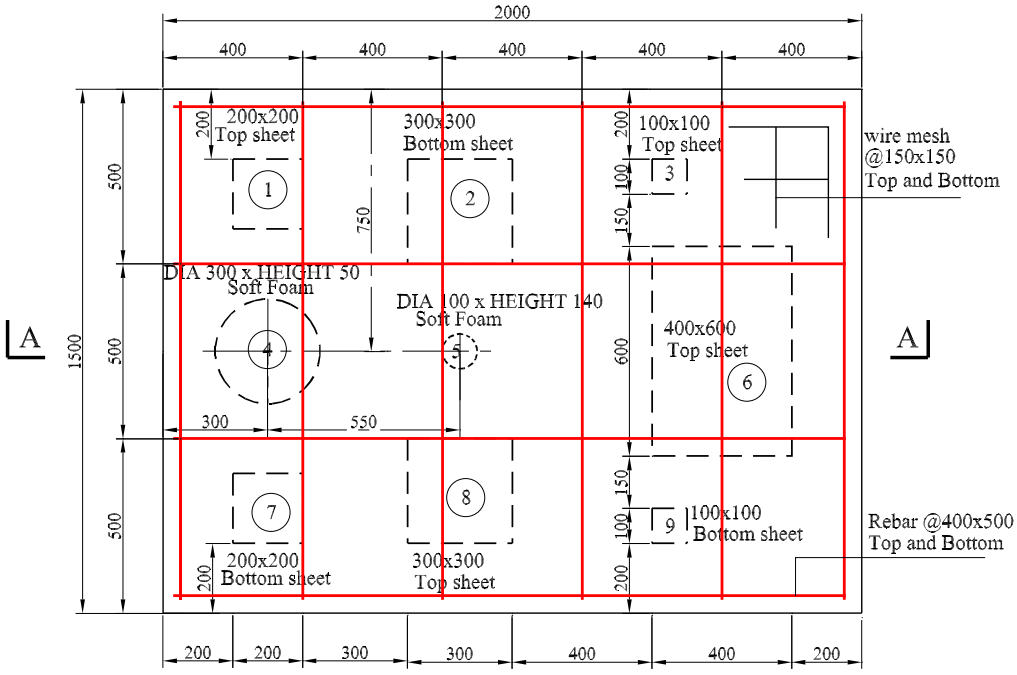

(a) Plan View of Slab No.2

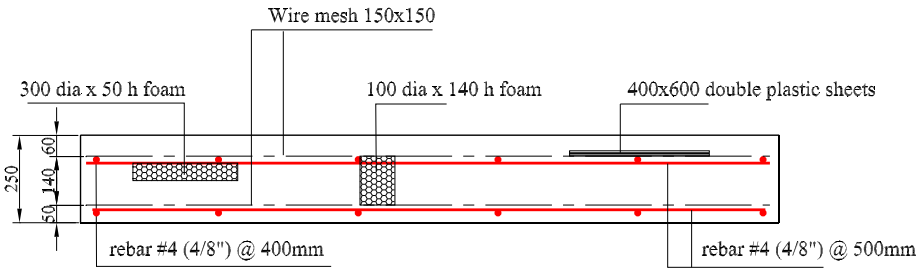

(b) Section A-A of Slab No.2

Note:
1. Top sheets are 60mm below the concrete top surface
2. Botom sheets are 200mm below the concrete top surface
3. Wire meshs are placed on rebar grid to help fix plastic sheets and foams.
4. All plastic sheets are double-layer sheets.
5. Two lifting hooks along the 2000mm side

Figure 7.6: (a) Plan view and (b) cross-section of slab No.2. Location of artificial delaminations and voids are marked.

Figure 7.7: Photo of the form for slab No.2 containing artificial delaminations and voids.

peak frequency within $5 \sim 20$ kHz range. For example, at $x = 24$ cm, although the correct frequency at 8.06 kHz is detected, it is not the highest peak. The normalized peak amplitude at $f = 8.06$ kHz is about only 0.72. Without a prior knowledge of the slab properties, wrong results may be obtained. Therefore, the source-to-receiver spacing should be confined within the region having 1.0 normalized amplitude.

For the musical microphone without sound insulation, Fig. 7.8 shows that within the range of $x = 5 \sim 15$ cm, even without insulation, good agreement with expected results is obtained. For the PCB microphone with good sound insulation, the usable spacing range is $x = 5 \sim 20$ cm (Fig. 7.9). Gibson [27] shows that the impact-echo frequency corresponds to the zero group velocity point of S1 mode of Lamb waves. Therefore in theory, impact-echo frequency should not change with source-receiver spacing. However the excitability of S1 mode decreases dramatically as source-receiver spacing increases, as shown in Fig. 7.10 [27]. When excitability is low, effects of ambient noise and direct acoustic waves become significant, potentially disrupting the results. Therefore, as in the contact impact-echo test, care should be taken to choose proper source-receiver spacing for air-coupled impact-echo. In addition, smaller spacing gives better spatial resolution for impact-echo imaging.

7.5 Air-coupled Impact-Echo for Delamination Detection

7.5.1 Point Test Results of Air-Coupled Impact-Echo

Air-coupled impact-echo tests were carried out over solid areas and all defect regions on slab No.2. The nine defects are numbered 1 to 9 from the left top corner to the right bottom corner, as marked in Fig. 7.6. The sensor was positioned over the center of each defect when defect regions were

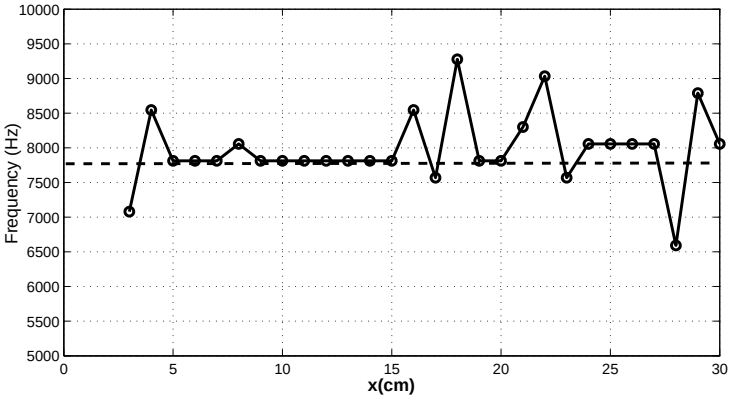

Figure 7.8: Impact-echo frequency vs. the source-receiver spacing for the musical microphone. The dashed line shows the expected full thickness impact-echo frequency for the slab at 7.8 kHz.

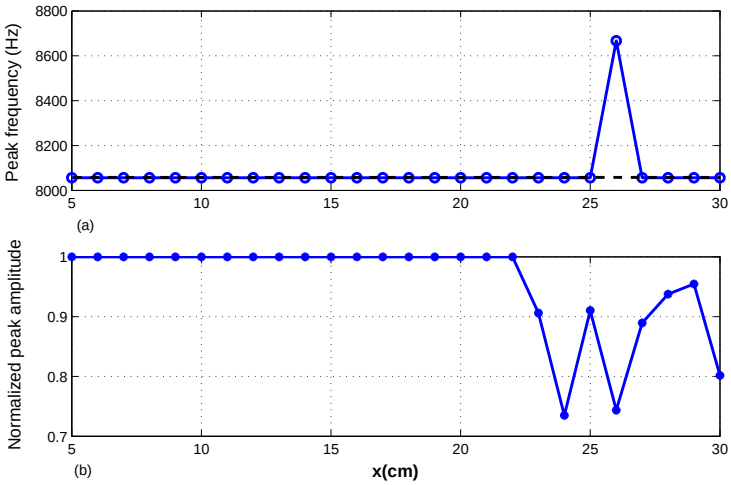

Figure 7.9: Effect of source-to-receiver spacing x on the air-coupled impact-echo test result for the PCB microphone. (a) Peak frequency and (b) normalized peak amplitude. The dashed line shows the expected impact-echo frequency at 8.06 kHz corresponding to the slab thickness of 250 mm.

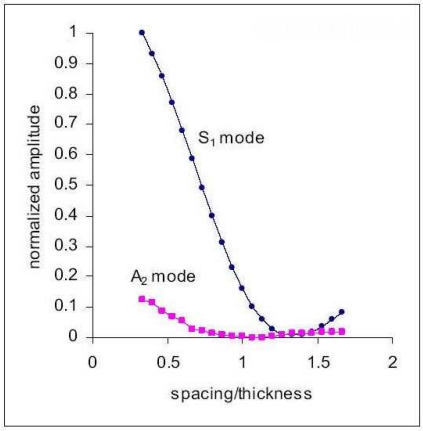

Figure 7.10: Out-of-plane S1 mode excitability vs. the normalized source-to-receiver spacing [27].

tested. The source-to-receiver spacing is between 5 and 10 cm, and the sensor was 3 cm above the concrete surface.

The air-coupled impact-echo test results over defects are listed in Table 7.1. Test points are grouped according to type of defects. For example, test points Nos. 1, 3, 6 and 8 are shallow delaminations about 55 mm below the top surface. There is no defect at point No.0, and the full thickness frequency 7.81 kHz was obtained. For shallow delaminations, the peak frequencies of air-coupled impact-echo tests are lower than the full thickness frequency. In these cases, the peak frequencies do not correspond to the impact-echo mode, but are set up by flexural modes. Flexural mode frequencies are affected by depth, areal size of defects and edge support conditions. With similar depth and support conditions, larger defect areas result in lower frequencies. The results show that shallow delaminations are easy to detect with air-coupled impact-echo by observing peak frequencies shifting lower in the frequency spectra. The voids (point Nos.4 and 5) behave like shallow delaminations, since the top surfaces of the voids are only 75 mm and 50 mm below the surface; low frequency flexural modes are observed.

Flexural mode frequency measurement is very consistent, and less affected by ambient noise than the impact-echo mode frequency. The flexural mode frequency measured by a microphone without sound insulation agrees with the result measured by a contact sensor. This conclusion is verified by the research of Asano et al. [4]: the impact sound (direct acoustic waves) frequency matches the flexural mode frequency.

Test point Nos. 2, 7 and 9 are over deep delaminations at depth of $190 \sim 195$ mm. The measured impact-echo peak frequencies at 10.62 kHz for points 2 and 7 give thicknesses of 185 mm, which agree well with the actual depth of 190 mm. However, no depth information was obtained for point No.9, because the defect is too small and deep. The peak frequency slightly shifts to lower frequency range, which indicates possible presence of defects using the flexural mode response model.

Since the signals over shallow delaminations are dominated by the flexural mode vibration, the depth of delaminations cannot be inferred from the peak frequency. According to the impact-echo equation $f = 0.96V_P/2H$, the impact-echo mode frequency is very high for shallow delaminations. Therefore, a broader frequency range should be investigated if depth information is to be obtained. Figure 7.11 shows the air-coupled impact-echo signal obtained over a shallow delamination (defect No.8). In the frequency spectrum, in addition to the peak at 2.68 kHz corresponding to the flexural mode, there is another peak at 33.2 kHz. It is the impact-echo mode which gives the depth of delamination at 59 mm. The result agrees very well with the actual depth of 55 mm . To obtain the peak at $f = 33.2$ kHz, a very small ball (5 mm diameter) was selected to excite the impact-echo mode. The excitability of the high frequency modes drops quickly with increasing ball size. It is difficult to detect the 33.2 kHz peak with the commercial impact-echo sensor (contact sensor) because it measures vertical displacement at the concrete surface, and displacement sensors are insensitive to higher frequency content. The high frequency mode can also be measured by an accelerometer, but accelerometers are insensitive to low frequency content. The air-coupled sensor measures pressure (equivalent to particle velocity), and have satisfactory response in both low and high frequency range.

Table 7.1: Results from air-coupled impact-echo tests on slab No.2, with the PCB microphone.

Test point No.	Size (mm)	Dominant Freq (kHz)	Tested thickness(mm) $H = 0.96 * V_p/2f$	Measured thickness (mm)
0 (solid)		7.81	252	250
1 (shallow)	200×200	4.15	Flexural mode	55
3 (shallow)	100×100	7.44	Flexural mode	55
6 (shallow)	400×600	1.22	Flexural mode	55
8 (shallow)	300×300	2.69	Flexural mode	55
4 (void)	Φ300	2.93	Flexural mode	75
5 (void)	Φ100	7.09	Flexural mode	50
2 (deep)	300×300	10.62	185	190
7 (deep)	200×200	10.62	185	195
9 (deep)	100×100	7.69	–	190

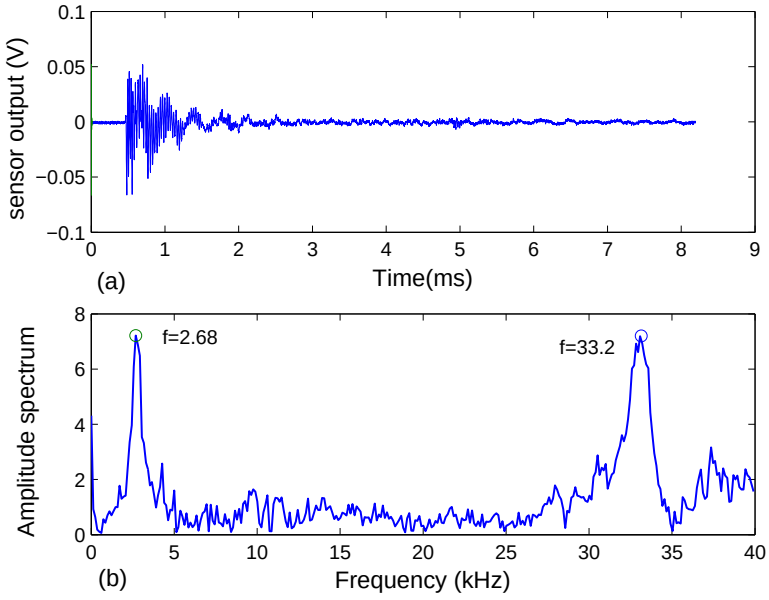

Figure 7.11: Typical air-coupled impact-echo signal obtained over a shallow delamination. (a) Time domain; (b) Frequency amplitude spectrum. The peak at 33.2kHz in frequency spectrum is the impact-echo frequency, which gives the depth of delamination at 59mm. The design depth is 55 mm below the top surface.

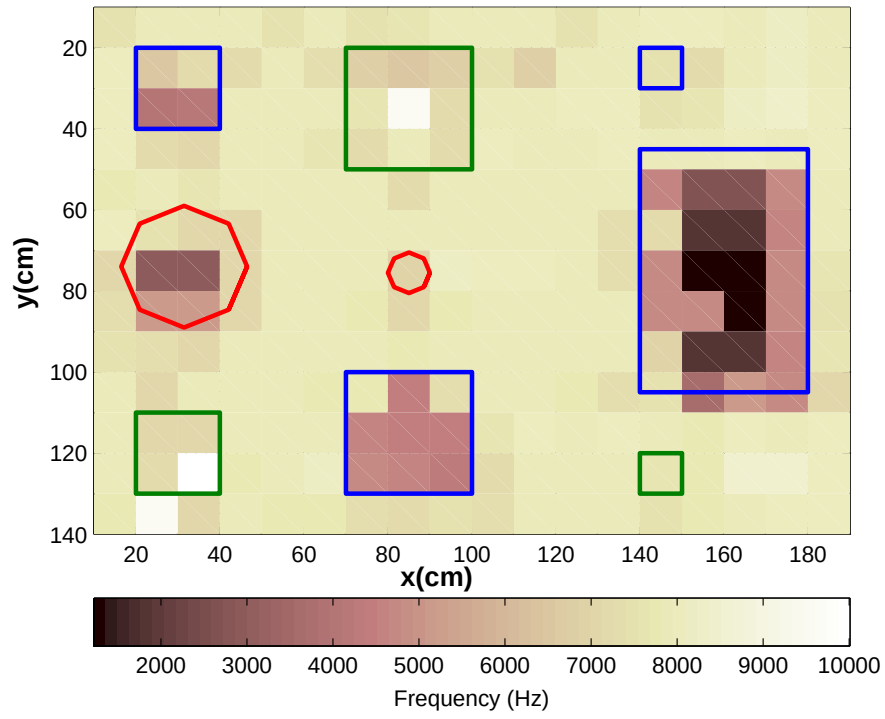

(a)

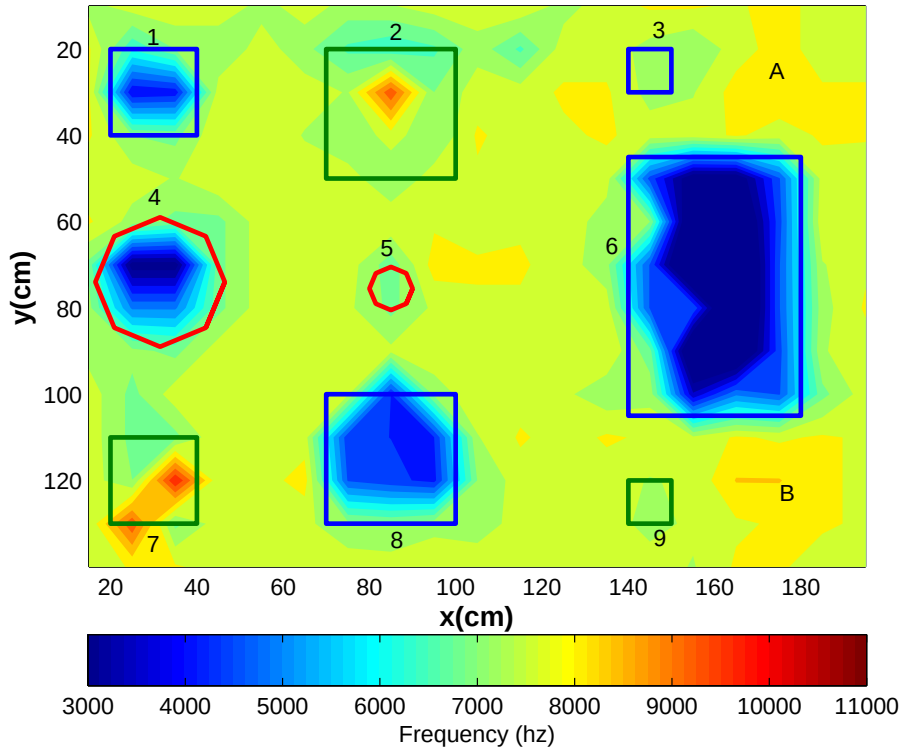

(b)

Figure 7.12: 2-D images of slab No.2 built up using air-coupled impact-echo data. (a) Pcolor image (b) contour image. The solid lines indicate location of defects.

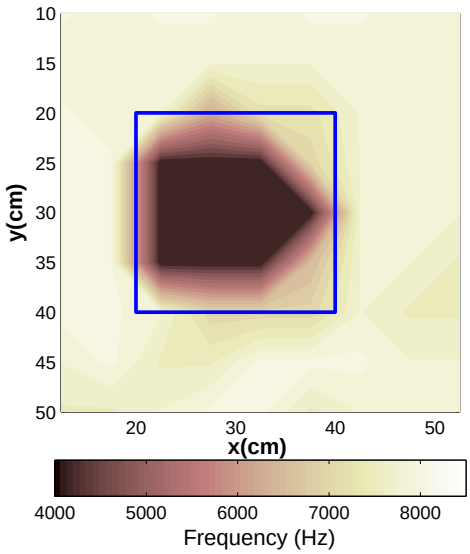

(a) Defect No.1.

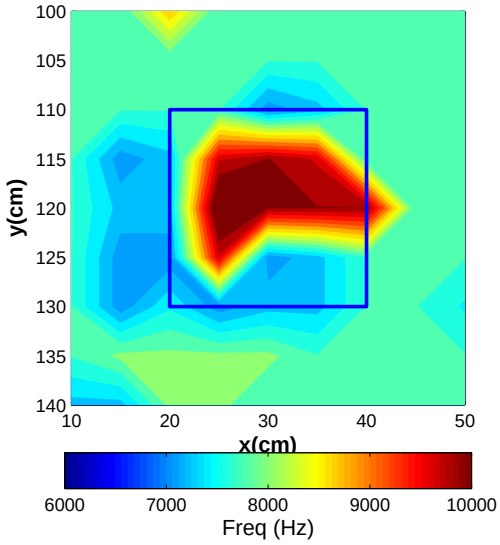

(b) Defect No.7.

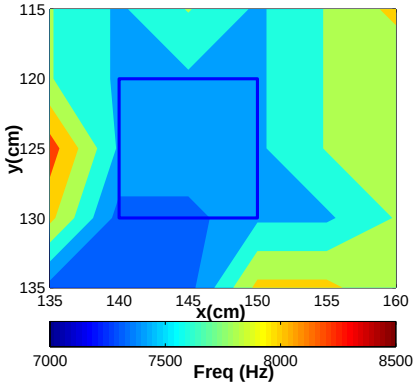

(c) Defect No.9.

Figure 7.13: 2-D contour images of defects (a) No.1 , (b) No. 7 and (c) No. 9 in slab No.2. Defect No.1 is a shallow delamination at depth of 55 mm, and defects Nos.7 and 9 are deep delaminations at depth of 190 mm.

7.5.2 2-D Imaging of Concrete Slab using Air-Coupled Impact-Echo

A 2-D scanning test was conducted over the entire area of slab No.2. The measurement grid spacing is $\Delta x = \Delta y = 10$cm in both directions; therefore in total $19 \times 14 = 261$ signals were obtained, no data were collected along the slab edges. A 2-D matrix, '*peakfreq*', composed of the peak frequency of each signal's amplitude spectrum at each point, is used for image construction. Figure 7.12 shows the 2-D scan images of slab No.2. Two type of imaging formats are used to present the images. Figure 7.12(a) uses the '*pcolor*' command in Matlab to plot constant color at each cell with the color associated with the corner having the smallest $x-y$ coordinates. For example, the value of $peakfreq(i,j)$ determines the color of cell in the ith row and jth column. Figure 7.12(b) is a contour plot, which uses the '*contourf'* command in Matlab. '*contourf'* first computes the contour matrix from data in matrix $peakfreq$, and then draws a contour plot of matrix $peakfreq$ with contour levels at the values specified in vector v. The areas between the isolines are filled with constant colors. The large number of elements in v produces a smooth contour image. However, refining vector v will not improve the spatial resolution of the image unless the scan spacing Δx and Δy are refined. In gray scale images, low frequency is plotted in dark color and high frequency in light color. In color images, warm colors represent high frequencies, and cold colors low frequencies. The design location of defects are also superimposed on the image with solid lines. Because '*pcolor*' and '*contourf'* use different algorithms to construct images, their results show some differences.

From Fig. 7.12, it can be seen that most defects are identified in the image except for defect Nos.3, 5 and 9. For large and shallow delaminations and voids, i.e. defect Nos. 1, 4, 6 and 8, the approximate areal size of damage regions are also determined, and agree well with the actual size and shape. For the small defects Nos. 3, 5 and 9, the image shows slightly lower frequencies than the normal full-thickness frequency, which indicates very minor damage level. The small defects can still be differentiated from the surrounding solid regions. Hot spots (high frequency) are observed over defect Nos. 2 and 7, which indicate existence of deep delaminations. However, the size of damage region cannot be accurately determined. The high frequency corresponding to the depth of delaminations is observed only in a small region near the center of damaged area. The peak frequency shifts to a lower frequency range when the test point is over edges of defects.

In addition to the designed nine defects, the regions marked 'A' and 'B' in Fig. 7.12(b) show a different color from the surrounding solid regions. The color represents a slightly higher frequency than the full-thickness frequency at 7.8kHz. However, there are no designed defects in regions 'A' and 'B'. Close examination of the picture in Fig. 7.7 reveals two steel chairs at location 'A' and 'B', which were used to support the top layer rebars. Existence of these steel chairs affects the result of impact-echo.

Refined 2-D scans were conducted over defect Nos.1, 7 and 9, using 5 cm scan spacing. The imaged regions for defect Nos.1 and 7 are 40×40 cm squares, and for defect No.9 a 25×20 cm rectangle. The scanning results are shown in Fig. 7.13. The refined scans give good definition of defect size, especially for the shallow delamination defect No.1. For defect No.7, high frequencies are observed in the center area, while lower frequencies are observed near the defect edges. The depth of delamination can be estimated accurately from the peak frequency at the defect center. Defect No.9 is too small and deep, therefore the impact-echo mode is difficult to excite. Existence of the defect however does reduce the stiffness of this region, and the peak frequency shifts to a

lower frequency region.

From Figs. 7.12 and 7.13, we also notice the measured frequency over a defect region is non-uniform. For shallow delaminations, the lowest flexural mode frequency is obtained from the center of the defect, and the frequency increases as the test point moves close to edges of the defect. For deep delaminations, the highest frequency, corresponding to the impact-echo mode, is obtained over the central portion of defect region. Low frequency (lower than the full thickness frequency 7.8kHz) is observed over the edges of the defect.

From the images, it can be seen that small spacing is needed to locate small defects. The scan spacing should be less than 1/2 of the expected defect size. In practice, a 2 cm spacing is sufficient to generate a scan image with spatial resolution that meets most requirements.

7.6 Air-coupled Impact-Echo for Grouted Tendon Ducts

Air-coupled impact-echo tests were conducted over slab No.1 to examine the grouting quality of the ducts. Scanning tests were first conducted along the centerline of the ducts to investigate the ability to differentiate grouted from ungrouted ducts. The scanning direction is from the ungrouted end to the fully-filled end. Cross-duct scanning tests were also carried out. The scan spacing is 5 cm for both tests.

Figures 7.14 and 7.15 show the air-coupled impact-echo scanning images along the metal and plastic ducts respectively. At each test point along the ducts, the impact-echo frequency spectrum is plotted in gray scale. A B-scan image is constructed by plotting spectrum of all test points along the ducts. Dark color for high amplitude and light for low amplitude. To improve contrast of the image, the amplitude spectra data are raised to the 4th power.

According to the design for both ducts, $Y = 0 \sim 50$ cm section is ungrouted, $Y = 50 \sim 100$ cm is half-grouted, $Y = 100 \sim 150$ cm is fully-grouted. It can be seen from Fig. 7.14 that there is clear distinction between the fully-grouted section and the remaining sections for the metal duct. The fully-grouted section shows higher frequency than the ungrouted and partially grouted sections, which indicates higher stiffness in the fully-grouted section. Although there are some differences between the ungrouted and partially-grouted sections, it is difficult to differentiate them because the difference in frequency is very small.

The scan results from the plastic duct are shown in Fig.7.15. No conclusion can be made based on the image to evaluate the grouting condition within the duct. The same limitation also applies to the contact impact-echo test. Fig. 7.16 shows the result of a scanning impact-echo test along the plastic duct, where a contact sensor was used. The grouting condition cannot be determined from the image either. It is probably because the plastic duct is very rigid. The grouting condition has little effect on the stiffness of duct regions. Therefore the impact-echo scans cannot differentiate sections with different grouting conditions.

Cross-duct scan tests were conducted along three lines in the direction normal to the centerline of ducts. The three lines pass the midpoint of each section, as shown in Fig. 7.5. Figure 7.17 shows three B-scan images obtained from the different sections using air-coupled impact-echo. The plastic and metal ducts are located at $x = 20$ cm and $x = 75$ cm respectively. At duct locations, the peak of amplitude spectra shifts to low frequency range. It can be seen the duct locations are clearly identified on the images, even in the fully-filled sections. By comparing these images, the

peak frequency obtained at the ungrouted and half-grouted duct sections drops more than that at the fully-grouted section. This agrees with the scanning result along the ducts.

Figure 7.18 shows 1.5 GHz GPR scanning images along the same ungrouted, half-grouted and fully-grouted duct sections. The two arches in the images are electro-magnetic wave reflections from the ducts: the plastic duct on the left, and metal duct on the right. For the plastic duct, the arch-shaped reflections exist over the ungrouted and half-grouted sections, but disappear over the fully-grouted section. It shows the GPR is effective for differentiating fully-grouted conditions in plastic ducts. The metal ducts cause strong reflections. The strong reflections cause a 'masking' effect that prevents detection of voids within the duct. The impact-echo test works in the contrary way. Therefore, combining advantages of GPR and impact-echo would help improve the accuracy of duct characterization.

7.7 Conclusions

The experimental work presented in this chapter investigates application of the air-coupled impact-echo technique to locate delaminations and voids, and determine duct filling condition in reinforced concrete slabs. A 1/4 inch diameter PCB measurement microphone with a specially-designed insulation stand works as the air-coupled receiver. Two 250 mm thick reinforced concrete slabs were cast. One contains delaminations and voids at different depth, and the other contains two ducts with different grouting conditions.

Experiments show that air-coupled impact-echo works well to locate and determine depth of delaminations and voids in concrete. 2-D air-coupled impact-echo scans were conducted over the entire slab. Refined scans on local defect regions were also carried out. The areal size of shallow delaminations and voids are easily identified by low frequency regions in the 2-D image. The depth of shallow delaminations can be determined by using a small steel ball impactor to excite the high frequency impact-echo mode. The microphone shows advantage over conventional contact sensors in detecting high frequency content in this case. Deep delaminations ($H = 190$ mm) larger than 200×200 mm are also successfully identified, and the depth can be calculated from the peak frequency measured near the center of defect area. For small voids and delaminations, the peak frequency shifts to the lower frequency range. The existence of small defects can be determined from the 2-D scanning image, but no depth information can be obtained.

Air-coupled impact-echo scans along the metal duct indicate grouting conditions within the duct. The impact-echo frequency along all sections of the duct are lower than the full thickness impact-echo frequency. In the ungrouted and half-grouted regions, the frequency is significantly lower than that in the fully-grouted region, but it is difficult to differentiate between ungrouted and half-grouted regions.

Impact-echo scans (air-coupled and contact) cannot determine grouting condition within the plastic duct. It is probably because the plastic duct is very rigid, which masks the stiffness variation caused by grouting conditions.

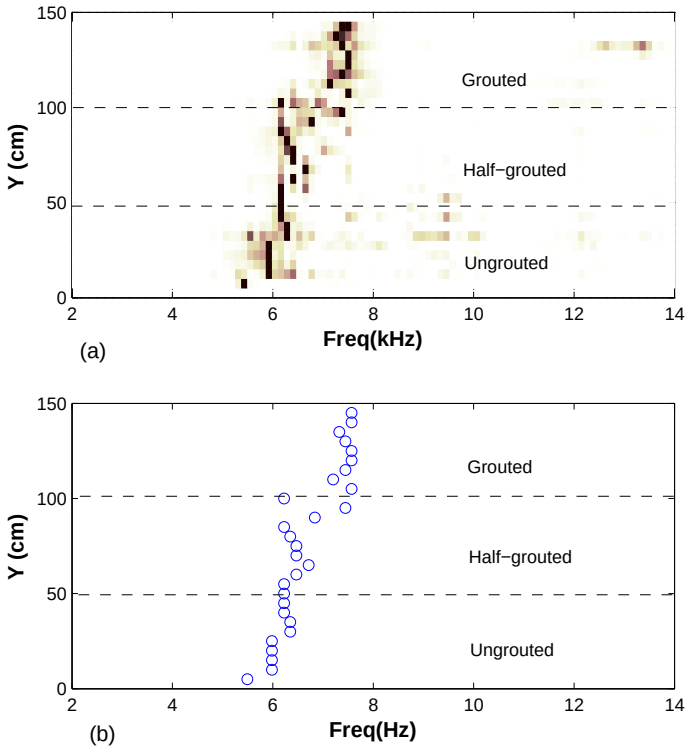

Figure 7.14: Air-coupled impact-echo scans along centerline of the metal Duct. (a) Impact-echo spectrum image. (b) Peak frequency along the metal duct. Y is the scan distance along the duct.

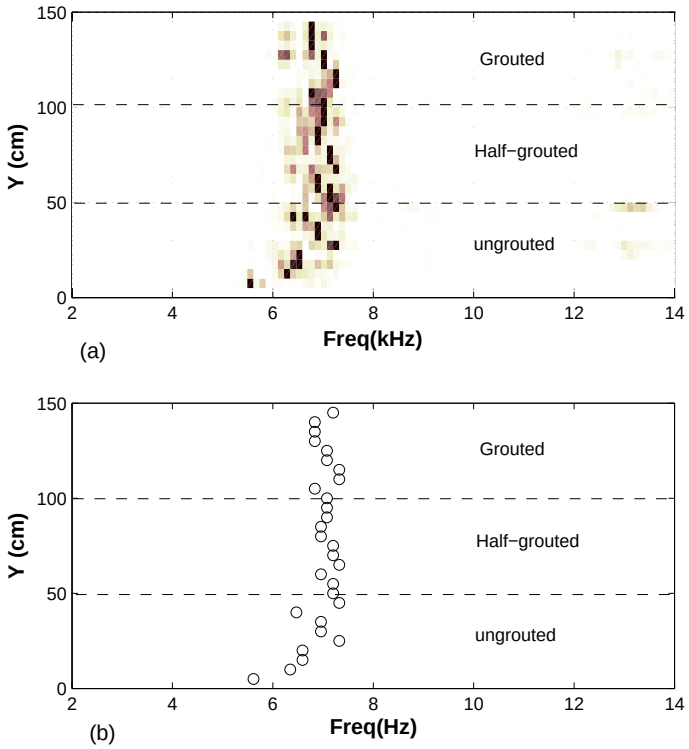

Figure 7.15: Air-coupled impact-echo scans along centerline of the plastic Duct. (a) Impact-echo spectrum image. (b) Peak frequency along the plastic duct. Y is the scan distance along the duct.

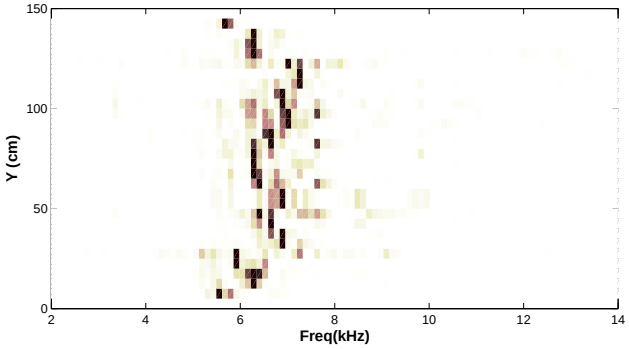

Figure 7.16: Conventional contact impact-echo spectrum image along centerline of the plastic duct.

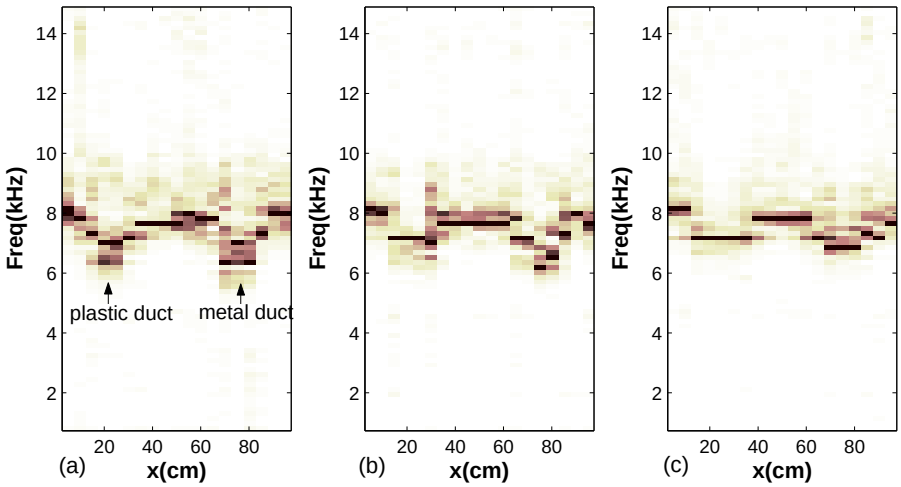

Figure 7.17: Air-coupled impact-echo scan across the duct direction. The three images represent scans on three sections with different grouting conditions. (a) Ungrouted; (b) Half-grouted; (c) Grouted. X is the scan distance.

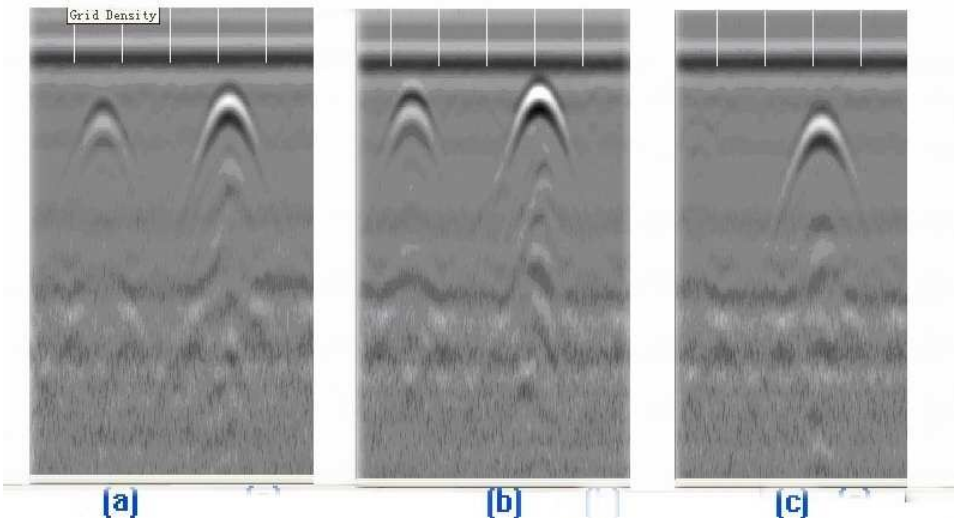

Figure 7.18: GPR cross-duct scanning images. (a) Ungrouted; (b)Half-grouted; (c)Grouted.

8 Future Work

Based on the theoretical analyses (chapter 4) and experimental studies (chapters 5, 6, 7) presented in this thesis, the following future work efforts are proposed to further develop air-coupled NDT techniques for concrete. The proposed work includes development of air-coupled impact-echo equipment, air-coupled impulse-response method, and an air-coupled surface wave transmission method for surface-breaking crack depth measurement.

8.1 Air-Coupled Impact-Echo Testing Equipment

The experimental studies presented in chapter 7 demonstrate that air-coupled impact-echo method can be applied to image embedded defects in concrete slabs. The sensitivity of air-coupled sensing is comparable, and in some cases superior, to that of the contact method. However, the testing efficiency of the air-coupled sensing system used in this research is not optimal. To improve efficiency, an automatic testing system should be developed. Similar to the Delamatec© to some degree, the system would consist of automated tappers (impactors), a sensitive microphone, and a computer-controlled data acquisition and signal processing system. The sensor and impactors would be mounted on a wheeled frame, where a 'control wheel' keeps track of the sensor position and controls impact triggering. A similar design has been used in other NDT scan systems, e.g. RADAR, and contact impact-echo scanning devices [67].

Small scanning spacing gives good spatial resolution in an image, enabling detection of small defects in concrete. With an air-coupled automated scanning system, very small scan spacings can be applied. Based on the study in chapter 7, the spacing should be less than 1/2 of the expected defect size. In practice, a 2 cm spacing is sufficient to generate an scan image with spatial resolution that meets most requirements.

The sound-proof microphone stand used in this research provides a good insulation barrier to ambient noise and direct acoustic waves. Air-coupled impact-echo tests were performed in the Newmark lab during normal operation hours. The air-coupled tests were not disturbed by the loud nearby machinery operating in the lab. Therefore, it is believed this design would withstand ambient traffic noise. However, the current design requires contact between the stand and concrete surface to maintain good sound insulation. The contact requirement significantly reduces the applicability of this method. Therefore, further study is needed to improve the design of the insulation barrier.

Experiment results indicate that the microphone height affects test results, although the reason is still unclear. One possible explanation is the sensor has a focal distance at which the sensitivity is maximum. Numerical analysis and experiments are needed to study the effect of sensing height on air-coupled impact-echo.

8.2 Air-Coupled Impulse Response

In the U.S. the Impulse Response (IR) method is mainly applied to plate-like structure testing, in addition to pile testing as in Europe and Asia. Equipment development in North America has focused on rapid testing over test point grid on large areas, such as bridge decks and industrial floor slabs. This approach allows immediate display of IR parameter contour maps over the tested area [18].

The IR test impact excites low frequency flexural modes of the plate structure. From the experimental results shown in chapter 7, for all types of defects, the flexural mode vibration is easier to excite than the impact-echo mode, especially for shallow delaminations. The flexural mode frequency is very consistent, and less affected by boundary reflections. However, the test efficiency of IR is still limited by the contact between the sensor (geophone) and concrete surface. Currently the IR test is conducted manually, and the operator needs to stop at each test grid point to apply an impact and collect data. To improve the efficiency, an automated testing system with air-coupled sensors could be applied. The system design would be very similar to the air-coupled impact-echo system discussed above, except the impactors would be replaced with a force hammer. The geophone used in IR tests would be replaced by a sensitive microphone with good low frequency response; most microphones meet this requirement. The microphone measures pressure, which in turn is proportional to the particle velocity at the concrete surface. Thus the output of an air-coupled IR test represents the dynamic mobility of the structure. In this way, current IR analysis software could also be used for the air-coupled IR test.

8.3 Depth of Surface-Opening Cracks

The effect of isolated surface-opening cracks on surface wave propagation has been investigated by Viktorov [68]. He found that the transmission coefficient T_r of surface waves across the crack depends on the ratio of crack depth to Rayleigh wavelength d/λ_R. Popovics and Song [49, 65] proposed a self-compensating surface wave transmission coefficient measurement method to measure T_r across cracks or notches in concrete using two surface-mounted accelerometers. The relation between d/λ_R and T_r has been established in that work. The testing scheme is similar to the SASW method. The surface wave transmission ratio is measured from two opposite directions, so that any inconsistency or asymmetry due to sensor coupling is cancelled. Five repeated signals are usually obtained and averaged in each direction, and the final transmission coefficient is calculated based on the average of results.

Although the self-compensating method improves data reliability, surface coupling is still problematic because it is time-consuming to prepare surface and keep good contact between sensors and concrete surface. If air-coupled sensors are used to replace the contact sensors, improved measurement accuracy and sensitivity are expected since the disruption from coupling effect and body waves are minimized.

Numerical simulation and experimental studies have been carried out by the author to study the relation between crack depth and surface wave transmission ratio. Results show that many factors affect the calculation of transmission ratio, and no unique relation between T_r and crack depth is derived from this study. Nevertheless it is still worthwhile to present the findings here, which are helpful to further study of this topic.

According to Yew et al. [72] the surface wave, after passing a crack, includes contributions from two sources: one is from a portion of incident surface wave transmitting through the crack, and the other from the scatted P- and S- waves from the crack tip. At low frequency, when λ_R is larger than the crack depth d, the incident surface wave contribution dominates. When $\lambda_R < d$, the reconstructed surface wave after the crack is mainly comprised of scattered P- and S- waves.

Yew et al.[72] also noted that the receiver position affects transmission calculation. Signals recorded by a receiver behind the crack contain contributions from surface waves and scattered body waves. If the receiver is placed very close to the crack (less than the crack depth), the wave field is dominated by scattered body waves and the surface wave is difficult to identify. The suggested sensing distance from the crack should be comparable to, or larger than, the crack depth.

To eliminate effects from body waves arriving before the surface wave and late-arriving reflections from slab boundaries, a time window is normally applied to the signals. The window is centered at the negative peak of the received surface wave pulse, and the window length is determined by the input force duration. Analysis shows that window parameters (length and shape) affect transmission ratio calculation. Tukey windows were investigated in this study. Tukey windows are cosine-tapered windows. The Matlab function $tukeywin(n, \alpha)$ returns an n-point Tukey window, where α is the ratio of taper to constant sections and is between 0 and 1. $\alpha = 0$ is a rectangular window and $\alpha = 1$ is a Hanning window. Figure 8.1 shows the effects of window length T (unit:μs) and shape α on surface wave transmission calculation. Numerical simulation signals (FEM) are obtained on simulated crack free surface of a solid half space. Surface wave ares excited by a simulated impact source with $50\mu s$ duration. It is seen that the transmission ratio varies significantly with window shape and length, especially in low and high frequency ranges. In the center frequency (20 kHz) region, all windows give similar results, and the transmission is relatively flat in this region. From Fig. 8.1, the Hanning window ($\alpha = 1$) gives a wide flat region of transmission ratio.

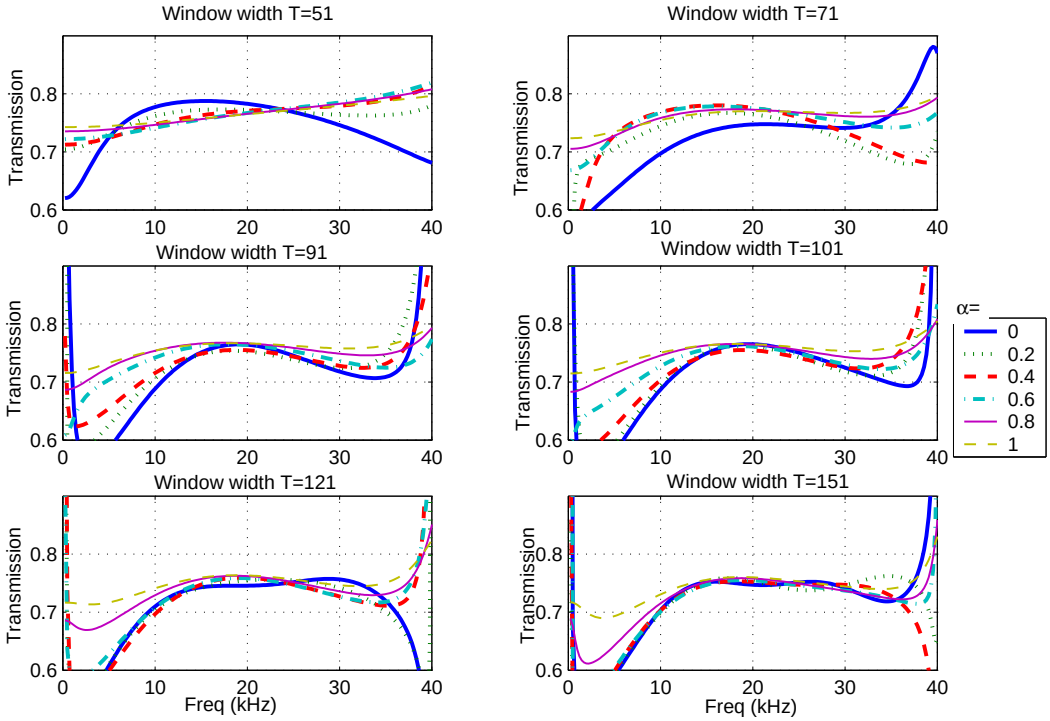

Figure 8.1: Effect of windowing on the calculated surface wave transmission. The length of Tukey windows vary from 51 μs to 151 μs, while the window shape changes with $\alpha = 0 \sim 1$.

9 Conclusions

Air-coupled sensing techniques are investigated in this study for NDT of concrete structures. The following conclusions are drawn from the conducted theoretical analyses and experimental studies.

Theory of Leaky Surface Wave Propagation

Theoretical analyses were first conducted to study the propagation of leaky Rayleigh waves in fluid-solid half spaces. The Green's functions for pressure in the fluid and displacement in the solid were derived using integral transform methods. Simplified solutions containing only interface wave contributions were also derived. The following conclusions are obtained from the theoretical analyses.

1. Within interface wave dominated regions (usually the near-interface regions), there is good agreement between the simplified and exact solutions. The simplified solutions provide an easy way to quickly estimate interface wave responses and isolate interface waves from other waves.

2. An impact point load normally applied to the interface is an effective way to generate Leaky Rayleigh waves in the fluid. The excitability of leaky Rayleigh waves generated by an impact point source is around $0.1 \sim 1.0$ Pa/kN, depending on the impact force duration. This represents measurable sound pressure levels that can be used for air-coupled sensing in concrete.

3. Leaky surface waves can be separated from the direct acoustic waves by using small z and large r. In air-coupled surface wave sensing, effects of direct acoustic waves can be eliminated by increasing the source-to-receiver spacing, and reduced by using sound insulation devices around the air-coupled sensor.

Air-Coupled Surface Wave Sensing

Air-coupled sensors were used to sense leaky surface waves in concrete slab structures. Three types of microphones were investigated for leaky surface wave detection. Experiments indicated microphones are very effective for detecting leaky surface waves that propagate in concrete. The measured signals have high sensitivity and good S/N ratio within the frequency range of interest.

Air-coupled sensors were used to measure surface wave dispersion curves in layered structures using SASW and MASW methods. Field tests carried out on a full-scale CRCP (continuously reinforced concrete pavement) indicated that air-coupled sensors are able to replace contact sensors in the conventional SASW and MASW tests, with an accuracy comparable to that of contact sensors. Test accuracy can be further improved by incorporating sound insulation design for the air-coupled sensor, to reduce effects of ambient noise and direct acoustic waves.

Using the contact-less nature of air-coupled sensing, surface wave attenuation was applied to investigate influences of defects in concrete. Experimental results indicated that the surface wave attenuation is more sensitive to existence of defects than the wave velocity. Further analysis is needed to correlate the surface wave attenuation (transmission) to the surface-opening crack depth.

Air-Coupled Impact-Echo

Air-coupled impact-echo was developed and applied to locate defects and determine their depths in concrete. Unlike leaky surface waves, the impact-echo vibration mode cannot be separated from the direct acoustic waves in the time signals by increasing the source-to-receiver spacing, so a sound insulation design is necessary for air-coupled impact-echo. The sound insulation used in this study was very effective in reducing acoustic noise. It also provided support for the microphone.

A small (1/4 inch diameter) measurement microphone was used for air-coupled impact-echo. The sensitivity of the microphone is comparable, or even superior, to that of contact sensors.

Two 250 mm thick reinforced concrete slabs were cast. One contained delaminations and voids at different depth, and the other contained two ducts with different grouting conditions. Experiments did show that air-coupled impact-echo works well to locate and determine depth of delaminations and voids in concrete. 2-D air-coupled impact-echo scans were conducted over the entire slab. All defects were located from the image. To accurately locate and determine the areal size of defects, the scan spacing should be smaller than 1/2 of the expected defect size.

Air-coupled impact-echo scans over a metal duct revealed grouting conditions in the duct. The poorly-grouted sections are clearly differentiated from the well-grouted section. However, grouting conditions for plastic ducts could not be determined by the impact-echo scans (both air-coupled and contact). The GPR scan works in the contrary way. Therefore, the accuracy of duct characterization could likely be improved by combining advantages of GPR and impact-echo.

Based on studies presented in this thesis, a practical air-coupled impact-echo scanning system can be developed. The air-coupled sensing techniques also show potential in applications to the Impulse Response method and surface-opening crack depth measurement in concrete.

References

[1] Achenbach, J. D., *Wave Propagation in Elastic Solids*, North-Holland, Amsterdam, The Netherland, 1973.

[2] ACI Committee 228, "Nondestructive test methods for evaluation of concrete in structures," Report ACI 228.2R-98, American Concrete Institute, Farmington Hills, MI., 1998.

[3] Alder, E., Billy, M., Quentin, G., Talmant, M., and Nagy, P., "Generalized Lamb modes in friction welded steel layer on aluminum," in *Review of Progress in Quantitative Nondestructive Evaluation*, edited by D. O. Thompson and D. E. Chimenti, volume 9, pages 1973–1980, American Institute of Physics, Melville, NY, 1990.

[4] Asano, M., Kamada, T., Kunieda, M., Rokugo, K., and Kodama, I., "Impact acoustics methods for defect evaluation in concrete," in *Non-Destructive Testing in Civil Engineering 2003*, volume Proceeding BB 85-CD, DGZIP, Berlin, Germany, Sept.2003.

[5] ASCE, "2001 report card for America's infrastructure," http://www.asce.org, Mar 2001.

[6] ASCE, "2003 progress report for America's infrastructure," http://www.asce.org, Sept 2003.

[7] Beard, M. D., Lowe, M. J. S., and Cawley, P., "Ultrasonic guided waves for inspection of grouted tendons and bolts," *Journal of Materials in Civil Engineering*, 15:212–218, 2003.

[8] Bohlen, T., Kugler, S., Klein, G., and Theilen, F., "1.5d inversion of lateral variation of scholte wave dispersion," *Geophysics*, 69(2):330–344, 2004.

[9] Bungey, J. H., "Sub-surface radar testing of concrete: a review," *Construction and Building Materials*, 18(1):1–8, 2003.

[10] Bungey, J. H. and Millard, S. G., "Radar inspection of structures," *Structures and Buildings Journal (London),Proceedings of Institute of Civil Engineers*, 99:173–186, 1993.

[11] Buyukozturk, O., "Imaging of concrete structures," *NDT&E International*, 31:233–243, 1998.

[12] Carcione, J. M. and Helle, H. B., "The physics and simulation of wave propagation at the ocean bottom," *Geophysics*, 69(3):825–839, 2004.

[13] Carino, N. J., Sansalone, M., and Hsu, N. N., "A point source-point receiver, pulse-echo technique for flaw detection in concrete," *ACI Materials Journal*, 83(2):199–208, 1986.

[14] Castings, M. and Hosten, B., "Lamb and SH waves generated and detected by air-coupled ultrasonic transducers in composite material plates," *NDT&E International*, 34:249–258, 2001.

[15] Chao, C., "Surface waves in an elastic half space," *J. App. Mech.*, 28:300–301, 1961.

[16] Clemeñ̃a, "Short-pulse radar methods," in *Handbook on Nondestructive Testing of Concrete*, edited by V. M. Malhotra and N. J. Carino, pages 253–274, CRC Press, Boca Raton, Fla., 1991.

[17] Davis, A. and Dunn, S. C., "From theory to experience with the non-destructive vibration testing of piles," in *Proc Inst Civil Engrs*, volume 57, pages 571–593, 1974.

[18] Davis, A. G., "The non-destructive impulse response test in north america: 1985c2001," *NDT&E International*, 36:185–93, 2003.

[19] Davis, A. G., Lim, M. K., and Petersen, C. G., "Rapid and economical evaluation of concrete tunnel linings with impulse response and impulse radar non-destructive methods," *NDT&E International*, 38:181–186, 2005.

[20] de Hoop, A. and van der Hijden, J., "Generation of acoustic waves by an impulsive line source in a fluid/solid configuration with a plane boundary," *J. Acoust. Soc. Am.*, 74:333–342, 1983.

[21] de Hoop, A. and van der Hijden, J., "Generation of acoustic waves by an impulsive point source in a fluid/solid configuration with a plane boundary," *J. Acoust. Soc. Am.*, 75:1709–1715, 1984.

[22] Delahaza, A., "Things you want to know about NDE of concrete - ground penetrating radar: Concrete evaluation applications," in *ACI Spring Convention, Vancouver, Canada*, 2003.

[23] Ewing, W., Jardetzky, W., and Press, F., *Elastic Waves in Layered Media*, McGraw-Hill Book Company, New York, 1957.

[24] Fellinger, P., Marklein, R., Langenberg, K. J., and Klaholz, S., "Numerical modelling of elastic wave propagation and scattering with efit - elastodynamic finite integration technique," *Wave Motion*, 21:47–66, 1995.

[25] Foti, S., *Multistation Methods for Geotechnical Characterization using Surface Waves*, Ph.D. thesis, University of Genova, 2000.

[26] Gan, T. H., Hutchins, D. A., Billson, D. R., and Schindel, D. W., "The use of broadband acoustic transducers and pulse-compression techniques for air-coupled ultrasonic imaging," *Ultrasonics*, 39:181–194, 2001.

[27] Gibson, A. and Popovics, J. S., "Lamb wave basis for impact-echo method analysis," *Journal of Engineering Mechanics*, 131(4):438–443, 2005.

[28] Glorieux, C. and Van de Rostyne, K., "On the character of acoustic waves at the interface between hard and soft solids and liquids," *J. Acoust. Soc. Am.*, 110:1299–1306, 2001.

[29] Grandia, W. and Fortunko, C., "NDE applications of air-coupled ultrasonic transducers," *IEEE Ultrasonics Symposium*, 1:697–709, 1995.

[30] Gusev, V., Desmet, C., Lauiks, W., Glorieux, C., and J., T., "Theory of scholte, leaky rayleigh, and lateral wave excitation via the laser-induced thermoelastic effect," *J. Acoust. Soc. Am.*, 100:1514–1528, 1996.

[31] Jaeger, B. J., Sansalone, M. J., and Po, R. W., "Detecting voids in grouted tendon ducts of post-tensioned concrete structures using the impact-echo method," *ACI Structural Journal*, 93:462–473, 1996.

[32] Kohler, E. R., *Experimental Mechanics of Crack Width in Full-Scale Sections of Continuously Reinforced Concrete Pavements*, Ph.D. thesis, University of Illinois at Urbana-Champaign, 2005.

[33] Krstoluvic-Opara, N., Woods, R. D., and Al-Shayea, N., "Non-destructive testing of concrete structures using the Rayleigh wave dispersion method," *ACI Materials Journal*, 93(1):75–86, 1996.

[34] Lamb, H., "On the propagation of tremors over the surface of an elastic solid,," *Phil. Trans. R. Soc.*, A203:1–42, 1904.

[35] Lin., Y. and Su, W., "Use of stress waves for determining the depth of surface-opening cracks in concrete structures," *ACI Materials Journal*, 93:494–505, 1996.

[36] Liu, Q., "Perfectly matched layers for elastic waves in cylindrical and spherical coordinates," *J. Acoust. Soc. Am.*, 105:2075–2084, 1999.

[37] Luke, B. A. and Stokoe, K. I., "Application of sasw method underwater," *J. Geotech. Engrg., ASCE*, 124(6):523–531, 1998.

[38] Martin, J., Broughton, K., Giannopolous, A., Hardy, M., and Forde, M., "Ultrasonic tomography of grouted duct post-tensioned reinforced concrete bridge beams," *NDT&E International*, 34:107–113, 2001.

[39] Moore, W., "Detection of bridge deterioration," *Highway Research Record*, (451):53–61, 1973.

[40] Moore, W., Swift, G., and Milberger., L., "An instrument for detecting delamlnation in concrete bridge decks," *Highway Research Record*, (451):44–52, 1973.

[41] Mozhaev, V. and Weihnacht, M., "Attenuated leaky rayleigh waves," *Ultrasonics*, 40:927–933, 2002.

[42] Nazarian, S., Baker, M., and Crain, K., "Assessing quality of concrete with wave propagation techniques," *ACI Materials Journal*, 94:297–305, 1997.

[43] Ozturk, T., Rapoport, J., Popovics, J., and Shah, S. P., "Monitoring the setting and hardening of cement-based materials with ultrasound," *RILEM Concrete Science and Engineering*, 1:83–91, 1999.

[44] Park, C. B., Miller, R. D., and Xia, J., "Multichannel analysis of surface waves," *Geophysics*, 64(3):800–808, 1999.

[45] Park, C. B., Miller, R. D., Xia, J., Ivanov, J., Sonnichsen, G. V., Hunter, J. A., Good, R., Burns, R., and Christian, H., "Underwater masw to evaluate stiffness of water-bottom sediments," *The Leading Edge*, 24(7):724–728, 2005.

[46] Pekeris, C. L., "The seismic surface pulse,," *Proc. Natn. Acad. Sci*, 41:469–80, 1955.

[47] Pessiki, S. P. and Carino, N. J., "Setting time and strength of concrete using the impact-echo method," *ACI Materials Journal*, 85:389–399, 1988.

[48] Popovics, J. S., "NDE techniques for concrete and masonry structures," *Progress in Structural Engineering and Materials*, 5(2):49–59, 2003.

[49] Popovics, J. S., Song, W., Ghandehari, M., Subramaniam, K. V., Achenbach, J. D., and Shah, S. P., "Application of wave transmission measurements for crack depth determination in concrete," *ACI Materials Journal*, 97:127–135, 2000.

[50] Popovics, J. S. and Wiggenhauser, H., "Non-contact laser vibrometer wave sensing on concrete," in *15th ASCE Engineering Mechanics Conference*, Columbia University, New York, NY, June, 2002.

[51] Qi, Q., "Subsonic leaky Rayleigh waves at liquid-solid interfaces," *J. Acoust. Soc. Am.*, 95:3222–3230, 1994.

[52] Rayleigh, L., "On waves propagated along the plane surface of an elastic solid," *London Mathematical Soc. Proc.*, 17:4–11, 1885.

[53] Rens, K. L., "Recent trends in non-destructive inspections in state highway agencies," *Journal of Performance of Constructed Facilities*, 12(2):94–96, 1998.

[54] Richart, F., Hall, J., and Woods, R., *Vibrations of soils and foundations*, Prentice-Hall Inc, Englewood Cliffs, New Jersey, 1970.

[55] Ritzwoller, M. H. and Levshin, A. L., "Estimating shallow shear velocities with marine multicomponent seismic data," *Geophysics*, 67(6):1991–2004, 2002.

[56] Ryden, N., *Surface Wave Testing of Pavements*, Ph.D. thesis, Lund University, 2004.

[57] Ryden, N. and Lowe, M. J. S., "Guided wave propagation in three-layer pavement structures," *J. Acoust. Soc. Am.*, 116(5):2902–2913, 2004.

[58] Ryden, N. and Park, C., "Surface waves in inversely dispersive media," *Near Surface Geophysics*, 2(4):187–197, 2004.

[59] Ryden, N., Park, C. B., Ulriksen, P., and Miller, R., "Multimodal approach to seismic pavement testing," *J. Geotech. Eng.*, 130(6):636–645, 2004.

[60] Sansalone, M. and Carino, N. J., "Detecting delaminations in concrete slabs with and without overlays using the impact-echo method," *ACI Materials Journal*, 86(2):175–184, 1989.

[61] Sansalone, M. and Streett, W. B., *Impact-Echo: Nondestructive Testing of Concrete and Masonry*, Bullbrier Press, 1997.

[62] Schickert, M., Krause, M., and Müller, W., "Ultrasonic imaging of concrete elements using reconstruction by synthetic aperture focusing technique," *J. Acoust. Soc. Am.*, 15(3):235–246, 2003.

[63] Schubert, F., Peiffer, A., Koehler, B., and Sanderson, T., "The elastodynamic finite integration technique for waves in cylindrical geometries," *J. Acoust. Soc. Am.*, 104(5):2604–2614, 1998.

[64] Scott, M. L., *Automated Characterization of Bridge Deck Distress Using Pattern Recognition Analysis of Ground Penetrating Radar Data*, Ph.D. thesis, Virginia Tech, 1999.

[65] Song, W. J., Popovics, J. S., Aldrin, J. C., and Shah, S. P., "Measurement of surface wave transmission coefficient across surface-breaking cracks and notches in concrete," *J. Acoust. Soc. Am.*, 113(2):717–725, 2003.

[66] Szilard, J., *Ultrasonic Testing: Non-conventional Testing Techniques*, Wiley, New York, 1982.

[67] Tinkey, Y., Olson, L. D., Bedon, R., and Lieberle, C., "Impact echo scanning technology for internal grout condition evaluation in post-tensioned bridge ducts," in *Non-Destructive Testing in Civil Engineering 2003,Proceeding BB 85-CD*, DGZIP, Berlin, Germany, Sept.2003.

[68] Viktorov, I. A., *Rayleigh and Lamb Waves*, Plenum, New York, 1967.

[69] Weyers, R. E., Prowell, B. D., Sprinkel, M. M., and Vorster, M., "Concrete bridge protection, repair, and rehabilitation relative to reinforcement corrosion: A methods application manual," Strategic Highway Research Program Report No. SHRP-S-360, National Research Council, Washington, D.C., 1993.

[70] Wiggenhauser, H., "Duct inspection using scanning impact-echo," in *Non-Destructive Testing in Civil Engineering 2003, Proceeding BB 85-CD*, DGZIP, Berlin, Germany, Sept.2003.

[71] Wright, W. and Hutchins, D., "Air-coupled ultrasonic testing of metals using broadband pulses in through-transmission," *Ultrasonics*, 37(1):19–22, 1999.

[72] Yew, C. H., Chen, K. G., and Wang, D. L., "An experimental study of interaction between surface waves and a surface breaking crack," *J. Acoust. Soc. Am.*, 75(1):189–196, 1984.

[73] Zhu, J. and Popovics, J. S., "Excitation and measurement of interface waves between solids and fluids," *Geophysics Research Letters*, submitted.

[74] Zhu, J. and Popovics, J. S., "Non-contact detection of surface waves in concrete using an air-coupled sensor," in *Review of Progress in Quantitative Nondestructive Evaluation*, edited by D. O. Thompson and D. E. Chimenti, volume 20B, pages 1261–1268, American Institute of Physics, Melville, NY, 2001.

[75] Zhu, J. and Popovics, J. S., "Non-contact imaging for surface-opening cracks in concrete with air-coupled sensors," *Materials and Structures*, 38:801–806, 2005.

[76] Zhu, J., Popovics, J. S., and Schubert, F., "Leaky Rayleigh and Scholte waves at the fluid-solid interface subjected to transient point loading," *J. Acoust. Soc. Am.*, 116:2101–2110, 2004.